



HAL
open science

Interactions and structures in polydisperse suspensions of charged spherical colloids

Guillaume Bareigts

► **To cite this version:**

Guillaume Bareigts. Interactions and structures in polydisperse suspensions of charged spherical colloids. Theoretical and/or physical chemistry. Université Bourgogne Franche-Comté, 2018. English. NNT : 2018UBFCK062 . tel-02015347

HAL Id: tel-02015347

<https://theses.hal.science/tel-02015347>

Submitted on 12 Feb 2019

HAL is a multi-disciplinary open access archive for the deposit and dissemination of scientific research documents, whether they are published or not. The documents may come from teaching and research institutions in France or abroad, or from public or private research centers.

L'archive ouverte pluridisciplinaire **HAL**, est destinée au dépôt et à la diffusion de documents scientifiques de niveau recherche, publiés ou non, émanant des établissements d'enseignement et de recherche français ou étrangers, des laboratoires publics ou privés.



**THÈSE DE DOCTORAT DE L'ÉTABLISSEMENT UNIVERSITÉ
BOURGOGNE FRANCHE-COMTÉ
PRÉPARÉE AU LABORATOIRE INTERDISCIPLINAIRE CARNOT
BOURGOGNE**

École doctorale n°553
École doctorale Carnot-Pasteur

Doctorat de Chimie Physique

Par

M. Bareigts Guillaume

Interactions et structures dans les suspensions polydisperses de
colloïdes chargés sphériques

Thèse présenté et soutenue à Dijon, le 14 Décembre 2018

Composition du Jury :

Mme Pirio, Nadine	Professeur, Université de Bourgogne, ICMUB	Présidente
Mme Duvail, Magali	Chercheur CEA/DRF, ICSM	Rapporteure
M. Von Roij, René	Professeur, Utrecht University, ITP	Rapporteur
M. Cabane, Bernard	Directeur de Recherche, CNRS, ESPCI	Examineur
M. Goehring, Lucas	Professeur assistant, Max Planck Institute Göttingen	Examineur
Mme Marry, Virginie	Professeur, Université Pierre et Marie Curie, PHENIX	Examinatrice
M. Labbez, Christophe	Chargé de Recherche, CNRS, ICB	Directeur de thèse
M. Simon, Jean-Marc	Maître de Conférences, Université de Bourgogne, ICB	Directeur de thèse

Titre : Interactions et structures dans les suspensions polydisperses de colloïdes chargés sphériques

Mots-clés : colloïdes, simulation, polydispersité, cristaux colloïdaux

Résumé : Les suspensions colloïdales se trouvent un peu partout autour de nous, dans les matériaux de construction, en cosmétique, dans l'alimentation, en biologie. Elles sont composées de particules nanométriques ou micrométriques dispersées dans un gaz, un liquide ou un solide.

Cette thèse porte sur les suspensions colloïdales dans des solutions ioniques, où les colloïdes portent une charge électrique, par exemple des particules de silice dans une solution aqueuse de chlorure de sodium, à un pH basique. Les colloïdes, ici approximés par des sphères, peuvent varier significativement en taille, ce qui peut avoir un effet important sur le comportement de ces systèmes. Cette étude vise à améliorer la compréhension de ces suspensions colloïdales chargées par des modèles théoriques résolus par des simulations numériques.

Un des défis de ces simulations est le grand

nombre de degrés de liberté. Pour chaque (micro-)ion il y a des centaines de molécules de solvant, et pour chaque colloïde des centaines voire des milliers d'ions. Pour s'en sortir, nous avons calculé les interactions effectives à l'échelle colloïdale. Nous avons repris et développé plusieurs approches, présentant chacune un compromis en terme de temps de calcul et précision.

La variation en taille des colloïdes peut introduire des effets intéressants, observés expérimentalement, notamment le fractionnement des suspensions en plusieurs phases cristallines quand on augmente la concentration en colloïdes. Des techniques de simulations Monte-Carlo simples associées aux interactions inter-colloïdes calculées précédemment ont permis d'obtenir des résultats en bon accord avec l'expérience.

Title: Interactions and Structures in Polydisperse Suspensions of Charged Spherical Colloids

Keywords: colloids, simulation, polydispersity, colloidal crystals

Abstract: Colloidal suspensions are found everywhere around us, in construction materials, in cosmetics, in food, in biology. They are composed of nanometric or micrometric particles dispersed in a gas, a liquid or a solid.

This thesis is about colloidal suspensions in aqueous salt solutions, where colloids bear an electric charge, for example silica particles in an aqueous solution of sodium chloride, at high pH. The colloids, here approximated by spheres, can vary significantly in size, which can have an important effect on the behavior of these systems. This study aims to improve the understanding of these charged colloidal suspensions by theoretical models solved by numerical simulations.

One of the challenges of these simulations is

the huge number of degrees of freedom. For each (micro-)ion there are hundreds of solvent molecules, and for each colloid there are hundreds if not thousands of ions. To deal with this, we calculated the effective interactions at the colloidal scale. We took and developed several approaches, each showing a trade-off in terms of computational time and accuracy.

The size variation of colloids may introduce interesting effects, experimentally observed, notably the fractionation of suspensions in several crystalline phases when the colloidal concentration is increased. Some simple Monte-Carlo simulation techniques in combination with the inter-colloid interactions computed previously allowed us to obtain results in good agreement with experiments.

List of Papers

This thesis is based on the following papers. The content of some of them constitutes chapters of this thesis.

- **Hiding in Plain View: Colloidal Self-Assembly from Polydisperse Populations**

Bernard Cabane, Joaquim Li, Franck Artzner, Robert Botet, Christophe Labbez, Guillaume Bareigts, Michael Sztucki, and Lucas Goehring.

Physical Review Letter, **116**(20), 208001, 2016

- **Effective Pair Potential between Charged Nanoparticles at High Volume Fractions**

Guillaume Bareigts and Christophe Labbez

Physical Chemistry Chemical Physics, **19**(6), p. 4787-4792, 2017

Chapter 2

- **Jellium and Cell Model for Titratable Colloids with Continuous Size Distribution**

Guillaume Bareigts and Christophe Labbez

The Journal of Chemical Physics, **149**, 244903, 2018.

Chapter 3

- **Structure and Thermodynamics of Aqueous Suspensions of Polydisperse Silica Nanoparticles: A Monte Carlo Study**

Guillaume Bareigts and Christophe Labbez

Manuscript

Chapter 4

Contents

Abbreviation Table	ix
1 General introduction	1
1.1 Systems	4
1.1.1 Fluid	4
1.1.2 Colloid crystals and polydispersity	4
1.1.3 Glass	7
1.2 Models	7
1.2.1 Primitive model	7
1.2.2 Coarse-Grained Model	8
1.3 Statistical thermodynamics	9
1.3.1 Principles	10
1.3.2 Ensembles	11
1.3.3 Dynamical quantities	12
1.3.4 Statistical thermodynamics of systems of classical particles	13
1.4 Simulation techniques	14
1.4.1 Monte-Carlo Simulations	14
1.4.2 Molecular Dynamics	17
1.4.3 Boundary Conditions and Long Range Interactions	18
1.4.4 Coarse-graining Interactions	24
1.5 Mean-Fields Approaches	31
1.5.1 Poisson equation	31
1.5.2 Poisson-Boltzmann equation	31
1.5.3 Cell Model	32
1.5.4 Renormalized Jellium Model	33

1.5.5	Numerical resolution of the Poisson–Boltzmann Equation	33
1.6	Structure Analysis	35
1.6.1	Radial distribution function	35
1.6.2	Structure factor	35
1.6.3	Local Bond-Order Parameters	38
2	Effective pair potential	41
2.1	Introduction	41
2.2	Model and Simulations	44
2.3	Results	48
2.4	Conclusion	50
3	Jellium and Cell Model	53
3.1	Introduction	54
3.2	Models	57
3.2.1	Cell model	58
3.2.2	Renormalized jellium model	59
3.2.3	Boundary conditions at the colloidal surface	61
3.2.4	Algorithm description	63
3.2.5	Suspensions and model details	65
3.3	Results	66
3.3.1	Charging process of silica	66
3.3.2	Renormalized parameters	71
3.3.3	Osmotic pressure	75
3.4	Conclusion	78
4	Structure and Thermodynamics of Aqueous Suspensions	83
4.1	Introduction	84
4.2	Methods	89
4.2.1	Model and Simulations	89
4.2.2	Effective structure factor	91
4.2.3	Local bond-order parameters	92
4.3	Results	94
4.3.1	HS40 silica suspensions	94

4.3.2	TM50 silica suspensions	105
4.3.3	Discussion and conclusion	113
	Conclusions	117
	Bibliography	121
	Remerciements	147

Abbreviation Table

BCC	Body-Centered Cubic
CS	Charged Sphere
DLVO	Derjaguin-Landau-Verwey-Overbeek
FCC	Face-Centered Cubic
FPM	Full Primitive Model
HCP	Hexagonal Close-Packing
HCY	Hard Core Yukawa
HS	Hard Sphere
IBI	Interactive Boltzmann Inverse
LJ	Lennard-Jones
MC	Monte-Carlo
MCM	Multi-Component Model
MCM-CM	Multi-Component Model from the Cell Model
MCM-RJM	Multi-Component Model from the Renormalized Jellium Model
MD	Molecular Dynamics
OCM	One-Component Model
PBC	Periodic Boundary Conditions
PBE	Poisson-Boltzmann Equation
PCM	Polydisperse Cell Model
PM	Primitive Model
PME	Particle Mesh Ewald
PRJM	Polydisperse Renormalized Jellium Model
RDF	Radial Distribution Function
RHCP	Random Hexagonal Close-Packing
RJM	Renormalized Jellium Model
SAXS	Small Angle X-Ray Scattering
SLJ	Shifted Lennard-Jones

Chapter 1

General introduction

Colloids are common in our everyday life starting from our own body to construction materials. Cosmetic cream and shampoo, milk and wine, toothpaste and shaving cream, mustard and chocolate, soils and paper, foam and smoke are other good examples of colloidal systems, that are composed of colloidal particles dispersed in a dispersion medium. Both the dispersed phase and dispersion medium can be either a gas, a liquid or a solid, with the exception of a gas dispersed in a gas phase. A particle is qualified as a colloid if it has at least one dimension between approximately 1 nm to 1000 nm[1]. To put this in perspective, the diameter of a human hair ($\sim 80 \mu\text{m}$) is ten thousand to a hundred times bigger than a colloidal particle. Colloids further present a large variety of shapes. When they are solid, they can be spherical, cubic, rod-like, or plate-like, to cite a few examples. Their smallness makes their specific surface area, expressed in square meter per gram, extremely large. The surface, and more generally speaking the physical chemistry properties of the interface thus play a key role in controlling the behaviour of colloidal dispersions. As an example, sedimentation of colloids is greatly retarded due to the enhanced frictional resistance at the interface with the dispersion medium as compared to the weight of the particle. When a colloid is suspended in a fluid, it experiences collisions from the fluid molecules which result (at every instant in time) in a net force on the particle. The direction of this net force is random, and as a result, if the particle is sufficiently small it performs a random walk through the fluid, i.e. Brownian motion. When more and more particles are added to the suspension, eventually they also start to interact (either repel or attract) with each others. This gives rise to collective behaviour, and ultimately leads to the formation of liquid-like states and solid-like ordered struc-

tures, i.e. colloidal crystals, as well as gel and glassy states and liquid crystals. Many industrial applications take advantage of these properties e.g. food, papers[2], drilling, plastics[3], construction materials, softeners, photonic crystals and photovoltaic cells[4]. However, the understanding of those systems is still rather limited and the technological developments remain principally empirical.

Electric charge at the surface of colloids and polydispersity are ubiquitous in the realm of colloidal systems. The electric charge which controls the electrostatic interactions among the colloids is often considered as fixed. More often, however, it arises from the titration process where surface groups ionize, for example, the titration of silanol groups $-\text{SiOH} \rightleftharpoons -\text{Si-O}^- + \text{H}^+$. It depends on the pH, the ionic strength and the salt nature but also on the surface curvature and interparticle interactions. The latter is referred to charge regulation but is often ignored in theoretical studies. Polydispersity is the property of having many (thus poly) non-identical components in the dispersed phase of a colloidal system. The variation from one component (e.g. a particle) to the next could be one of many parameters, such as size, shape, charge, density etc. . . In theoretical studies polydispersity is often ignored, as solving the single-sized or monodisperse problem is often sufficiently complicated. However, as real experiments are always performed on at least slightly polydisperse systems it is essential to rationalize the effects of this pervasive phenomenon.

Since the 1940's, the stability of colloidal dispersions in aqueous solution has been rationalized with the help of the DLVO theory [5, 6], that combines a short range attractive (van der Waals) potential with a long range electrostatic repulsion. Indeed, a strong attraction can force particles to coagulate and lead to a phase separation, whereas a dispersion under strong repulsion can remain stabilized for years [4]. Unfortunately, the DLVO theory is valid only for a limited range of conditions. In particular, it is valid for weakly coupled systems, i.e. where ion-ion correlations are not predominant. What is more, the DLVO theory is restricted to high particle dilution and thus does not account for the many-body interactions involved at finite colloid concentrations. The lack of a generalized set of DLVO like effective potentials for charge and size polydisperse colloidal systems, on one hand, and of extensive computer simulations on aqueous suspensions of charged polydisperse particles, on the other hand, explains our poor understanding of these complex systems and the motivations of this work.

More specifically, it started with a discussion with Bernard Cabane on the structural evolution of thin films of aqueous silica nanoparticle dispersions (Ludox HS40) during drying[7]. The structure of the colloidal film was followed by small X-Ray scattering (SAXS). The short-range order was initially observed to increase as the dispersion was concentrated by evaporation before decreasing continuously upon further evaporation. Upon slow compression by osmotic stress and long equilibration time, the aqueous silica dispersion showed the same qualitative behavior. In addition, scattering intensities recorded by SAXS in the density region of maximum order, revealed multiple Bragg peaks characteristic of colloidal crystals with a large superlattice, despite the broad size polydispersity of the colloids[8]. This collection of experimental results brought many questions, fed many discussions and motivated the combination of an in depth experimental study[9] with the present simulation investigation. The main questions were: 1) How the decrease in the short range order in the dispersions at high densities can be explained? Is it the result of aggregation due to short range attractive forces? 2) How the solid-crystalline phases vary with the size/charge polydispersity of the colloids and what are they? 3) Is it possible to predict them and how?

Here, simulation techniques are developed, tested and used to address these questions. The strategy followed is based on a hierarchical multiscale approach. First, various numerical methods are developed for determining the effective pair potentials in charged and polydisperse colloidal systems. Then, computer simulations, employing these effective *force fields*, are further used to identify, at the microscopic scale, the different chemical and physical processes when charge polydisperse colloids are immersed and concentrated into an aqueous salt solution in an attempt to predict their macroscopic behavior.

The thesis is organized as follow. In the following sections, the theoretical background and the simulation techniques are described. Chapter 2 (Paper II) deals with the determination of the effective pair potential between charged colloids at high particle volume fractions in the low and high coupling regime. Then in Chapter 3 (Paper II), two numerical methods are developed and deployed to calculate the effective pair potentials in polydisperse suspensions of titratable colloids. Finally, Chapter 4 (Paper IV) prospects the validity of the two previous methods and studies in details the structure and the phase behavior of suspensions of polydisperse silica nanoparticles varying the ionic strength and size distribution.

1.1 Systems

This thesis examines inter-colloid interactions and the phase behavior of charged hard sphere systems. Of particular interest, is the effect of size polydispersity on these systems. Here we give an overview of the phases observed in repulsive systems of spherical colloids, either due to hard-core or electrostatic interactions. We further describe some of the experimental systems with which the present simulation work was compared to.

1.1.1 Fluid

A fluid is an ergodic disordered state whose structure depends on the colloid density. In the very diluted regime, a dispersion of hard core (HS) or charged hard sphere (CS) behaves as an ideal gas characterized by colloid pair distribution function, thereafter denoted as $g(r)$, insensitive to their separation r and equal to unity. In reality, a Coulomb or hard core hole is present for a small range of r , compared to the mean colloid separation, but can be neglected. The thermodynamic properties can then be easily calculated with a pen and paper. As the colloid density is increased the colloidal particles start to repel with each other and form a non ideal gas characterized by some short range oscillation in the $g(r)$. Upon further addition of colloids, the $g(r)$ shows long range oscillations characteristic of a liquid. The determination of the thermodynamic properties then requires the use of simulations or advanced theories, e.g. Hypernetted Chain theory, that properly account for the colloidal interactions (non ideality).

1.1.2 Colloid crystals and polydispersity

A colloidal crystal, analogous of mineral crystals, is an ergodic solid state whose colloidal particles are arranged in a highly ordered structure forming a crystal lattice that repeats in all directions of space. Colloidal crystals were first observed in nature with viruses during the first half of the last century [10, 11], in iron oxide sols forming schilling layers [12] and later in natural silicate opals[13, 14] formed by sedimentation of uniform silica particles [15]. The discovery with viruses clearly pointed out the importance of the narrow particle size distribution in forming crystals. The rapid development in the field of colloidal crystals started later (in the second half of the last century) with the emergence of computer simulations[16, 17] and elaboration of simple and low-cost methods of preparing

synthetic colloids with very narrow size distribution[18, 19]. It traces back to the long time controversial discovery of the freezing transition in a purely entropic system made of hard core particles: i.e. the ordering transition can be “entropy driven.” At that time the generally accepted idea was that a spontaneous phase transition from the fluid to the crystalline state can only take place if the freezing lowers the internal energy of the system sufficiently to outweigh the loss in entropy: i.e. the ordering transition is “energy driven.” However, counter-intuitively, the entropy increases because the free-volume per particle is larger in the ordered than in the disordered phase. This transition in hard core systems had been predicted by Kirkwood[20] in the early fifties based on an approximate theory confirmed by Alder and Wainwright[16] and Wood and Jacobson[17] using numerical simulations and experimentally by Pusey and van Megen [18] using colloidal particles that behave nearly as ideal hard core particles. Today, the entropy-driven freezing transition is generally accepted for hard core systems and is even seen to apply to many other systems, not to say to be the rule[21].

Table 1.1: A list of crystalline structures found in hard-sphere systems FCC: face-centered cubic, BCC: body-centered cubic, RHCP: random hexagonal close-packing

System	Structures	ref
Monodisperse	FCC	[18]
Monodisperse	RHCP	[22]
Binary	FCC	[23, 24]
Binary	FCC(large)	[25]
Binary	FCC + FCC	[26]
Binary	AB (NaCl)	[27, 28]
Binary	AB (CsCl,CrB,CuTi,IrV)	[28]
Binary	AB ₂ (AlB ₂)	[29, 30, 31, 28]
Binary	AB ₂ (HgBr ₂ ,AuTe ₂ ,Ag ₂ S)	[29, 30, 31, 28]
Binary	AB ₂ (MgZn ₂ ,MgCu ₂)	[26, 32, 33]
Binary	AB ₂ (MgNi ₂)	[26]
Binary	AB ₆	[34, 28]
Binary	AB ₁₃	[30, 35, 27, 31]
Polydisperse	FCC (fractionated)	[36]

Table 1.2: A list of crystalline structures found in charged-sphere systems FCC: face-centered cubic, BCC: body-centered cubic, RHCP: random hexagonal close-packing

System	Structures	ref
Monodisperse	FCC	[37, 38]
Monodisperse	BCC	[37, 38]
Binary	BCC	[39]
Binary	AB (CsCl)	[40, 41]
Binary	AB ₂ (MgZn ₂)	[34, 26, 32, 42]
Binary	AB ₂ (MgCu ₂)	[34, 32, 42]
Polydisperse	AB ₂ (MgZn ₂) + BCC (fractionated)	[8]

The freezing and melting density of monodisperse HS was established in 1968 by Hoover and Ree[43] and was found to predict accurately experiments[18]. The stable solid phase has a face centered cubic (fcc) structure. The phase diagram of repulsive point Yukawa particles as a model of CS was established in 1988 by Robins et al [44]. It shows in addition to the stable fcc solid phase a stable body centered cubic solid phase in the low ionic strength and density region triggered by the long range electrostatic repulsions between the CS. Since then a long list of crystalline structures was predicted and observed in binary mixtures of CS and HS. Tables 1.1 and 1.2 give an overview of the crystal structures found in HS and CS systems, respectively.

Guided by the first findings on natural colloidal crystals and the analogy with atomic and molecular crystals where all elements are identical, lots of efforts have been deployed to approach as much as possible an ideal monodisperse colloidal dispersion. An other motivation was also to test theories and numerical simulations which until recently completely ignored polydispersity. All of this have fueled the common idea/concept of the so called terminal polydispersity (in size, shape or charge) beyond which the formation of colloidal crystals is prevented, see e.g. [45]. Such an idea has been challenged in the last two decades by simulations on ideal HS systems. Polydispersity is predicted to shift the phase boundaries upward in a non trivial way and to even introduce novel phases by fractionation above a critical value of 7-8%[46, 47, 48], if they are able to form. These predicted features of fractionated crystals and multiple-phase coexistence were only recently observed by Cabane and co-authors[8] on aqueous dispersions of polydisperse CS, silica

nanoparticles (≈ 10 nm), with very high polydispersity ($\approx 14\%$). The observed phase diagram was found, however, to be much richer than so far predicted, with the coexistence between a fluid, a solid bcc and a solid MgZn₂ Laves, see Table 1.2. In Chapter 4, the phase behavior of this system is studied in details.

1.1.3 Glass

Glasses are non-ergodic disordered solid states characterized by a very slow particle dynamics and peculiar mechanical properties[49]. They appear in many classes of materials ranging from silicates to metals and polymers but also in colloids. See e.g.[50] for a recent review. The first clear evidence of a colloid glass was observed by Pusey and Van Megen[18] in their experimental model of HS system which experimentally confirmed the freezing transition suggested by simulations by Hoover and Ree[43]. It was found at high HS densities well above the freezing transition[51]. In CS systems colloidal glasses are also commonly found, but at much lower particle densities. It is fair to say that glasses and the glass transition are not much understood and are thus a very active field of research. Vitrification can, however, be viewed as a competing process of crystallization. Various strategies can be applied to obtain and stabilize over a long period of time colloidal glasses[49, 50]. One of the most natural ones is to take advantage of particle polydispersity. Colloidal glasses are discussed further in Chapter 4.

1.2 Models

Ideally, one would like to model an aqueous dispersion of polydisperse colloids with all its atomic details. Numerical calculation of such a model is at best very expensive and at worst impossible to carry out. It is then necessary to use approximate models which retain the essential physics and chemistry of these systems. The aim of this chapter is not to give a full descriptions of all the existing models but rather to give a brief description of those used in Chapters 2–4.

1.2.1 Primitive model

The primitive model (PM) is a standard model for charged colloidal dispersions. The colloids and ions are treated explicitly, and the solvent molecules are implicit. The elec-

trostatic interactions between colloids and ions are described by Coulomb pair potentials, reading

$$u_{ij}^{el}(r) = \frac{q_i q_j}{4\pi\epsilon r}, \quad (1.1)$$

where i and j are particles (colloid or ion) of charge q_i , r is the separation between i and j , ϵ is the electrical permittivity of the solvent.

Particles interact also via short-range interactions. The simpler ones are hard sphere (HS) interactions, whose potentials read

$$u_{ij}^{\text{HS}}(r) = \begin{cases} +\infty & \text{if } r \leq R_i + R_j \\ 0 & \text{otherwise} \end{cases} \quad (1.2)$$

where R_i (resp. R_j) is the radius of the particle i (resp. j). A more realistic potential is the paradigmatic attracto-repulsive Lennard-Jones (LJ) potential, which reads

$$u_{ij}^{\text{LJ}}(r) = 4\epsilon_{ij}^{\text{LJ}} \left[\left(\frac{\sigma_{ij}^{\text{LJ}}}{r} \right)^{12} - \left(\frac{\sigma_{ij}^{\text{LJ}}}{r} \right)^6 \right], \quad (1.3)$$

with $\sigma_{ij}^{\text{LJ}} = R_i + R_j$ and $\epsilon_{ij}^{\text{LJ}}$ is an energy parameter (the minimum of the LJ potential). To model repulsive soft sphere interactions, one may use the shifted and truncated Lennard-Jones (SLJ) potential, which reads

$$u_{ij}^{\text{SLJ}}(r) = \begin{cases} 4\epsilon_{ij}^{\text{SLJ}} \left[\left(\frac{\sigma_{ij}^{\text{SLJ}}}{r} \right)^{12} - \left(\frac{\sigma_{ij}^{\text{SLJ}}}{r} \right)^6 + \frac{1}{4} \right] & \text{if } r \leq R_i + R_j \\ 0 & \text{if } r > R_i + R_j \end{cases}, \quad (1.4)$$

where $\sigma_{ij}^{\text{SLJ}} = 2^{-1/6}(R_i + R_j)$ and $\epsilon_{ij}^{\text{SLJ}}$ is an energy parameter.

1.2.2 Coarse-Grained Model

Complex systems like colloidal dispersions in particular, have a large number of degrees of freedom. Charged colloidal dispersions can have hundreds to hundreds of thousands of ions per particle, and many more solvent molecules. These systems require huge computational power even for relatively small ones. A possible solution consists in reducing the system in less components by averaging out the degrees of freedom of the solvent and/or of the ions, this is often named coarse-graining. In this regard the PM is already a coarse-grained model because the solvent is treated implicitly.

At low electrostatic couplings and low density, the standard approach of Derjaguin, Landau, Verwey and Overbeek, known as DLVO theory[5, 6], applies. The electrostatic

interactions between spherical colloids are described by *screened* Coulomb potentials, or Yukawa potentials, of the following form,

$$u_{ij}^Y(r) = \frac{Q_i Q_j f_i f_j}{4\pi\epsilon r} \exp(-\kappa r), \quad (1.5)$$

where Q_i (resp. Q_j) is the charge of the colloid i (resp. j), κ is the inverse screening length or inverse Debye length. It reads

$$\kappa = \sqrt{\frac{4\pi\epsilon}{k_B T} I}, \quad (1.6)$$

where $I = \sum_{\alpha=1}^{n_I} q_{\alpha}^2 c_{\alpha}$ is the ionic force, with n_I the number of ionic species, c_{α} is the bulk concentration of the ionic specie α , k_B the Boltzmann constant, T the temperature. f_i is a form factor that depends on the composition of the colloid i . For homogeneous spheres it reads

$$f_i = \frac{\exp \kappa R_i}{1 + \kappa R_i}. \quad (1.7)$$

For “hollow” spheres (the solution can get inside the colloid), it reads

$$f_i = \frac{\sinh \kappa R_i}{\kappa R_i}. \quad (1.8)$$

At higher couplings or higher concentrations, this approximation breaks. One would have to take into account 3-body, 4-body etc...interactions. It has been found that Yukawa potentials with *effective* parameters (Q^* , κ^*), which notably depend on the colloidal density, can describe well charged dispersions. §1.5 describes some methods to calculate these effective parameters.

However, at very high electrostatic couplings, ionic correlations have to be accounted for, and therefore the Yukawa is no longer a good fit and a correct pair potential does not have a simple form and must be computed numerically. §1.4.4 describes some methods to work out these potentials.

1.3 Statistical thermodynamics

At a microscopic scale, a colloidal dispersion, and many other materials, can be described by myriad atoms and molecules in motion at some level, or more deeply by the time evolution of a complex quantum state. At a macroscopic level these materials are described by a limited set of properties (temperature, pressure, ...) usually accessible by experiments.

Statistical thermodynamics makes a bridge between these two scales. A probability p_i is associated to a micro-state i , the set of probabilities associated with given macroscopic constraints defines an ensemble. Furthermore, two postulates are made, namely the *ergodic* and *equipartition* principles. Below these principles are detailed followed by a definition of the main thermodynamic ensembles and further notions of statistical thermodynamics.

1.3.1 Principles

Ergodic principle

The ergodic principle states that the time average of a macroscopic quantity is equal to the statistical average of the same quantity. This means that, for a quantity A that has values A_i for each micro-state i , we have

$$\lim_{T \rightarrow +\infty} \frac{1}{T} \int_0^T A(t) dt = \sum_i p_i A_i \quad (1.9)$$

Equipartition principle

The equipartition principle states that all micro-states are equiprobable. It implies that there is a number Ω such that

$$p_i = \frac{1}{\Omega} \quad (1.10)$$

for all micro-state i , where Ω is the number of possible micro-states.

The entropy S is defined as proportional to the Shannon expression of loss of information,

$$S = -k_B \sum_i p_i \ln p_i, \quad (1.11)$$

where k_B is the Boltzmann constant.

So, for an isolated system, the entropy reads

$$S = k_B \ln \Omega. \quad (1.12)$$

One can show that it is the *maximum* entropy for all probability distributions. So the equipartition principle is the equivalent of the second principle of thermodynamics at the microscopic level.

1.3.2 Ensembles

Microcanonical ensemble

In the microcanonical ensemble the system is isolated and the energy E of a system is set (often within a $E \pm \delta E$ interval) such as for a micro-state i E_i is defined within the interval $E - \delta E < E_i < E + \delta E$. The equipartition principle (see §1.3.1) implies that the entropy S takes the form

$$S = k_B \ln \Omega(E), \quad (1.13)$$

where $\Omega(E)$ is the number of micro-states that satisfy the constraint on E .

Canonical ensemble

In this ensemble the system can exchange energy with a larger system at temperature T . The constraint is therefore that the mean energy ($\sum_i p_i E_i$) is set. Maximizing entropy yields the following form for the probability distribution:

$$p_i \propto \exp^{-\beta E_i}. \quad (1.14)$$

With the thermodynamic relation $T = \frac{\partial E}{\partial S}$, and the relation $\sum_i p_i = 1$, one can show that

$$p_i = \frac{\exp\left(-\frac{E_i}{k_B T}\right)}{Z}, \quad (1.15)$$

where Z is defined as the partition function,

$$Z = \sum_i \exp\left(-\frac{E_i}{k_B T}\right). \quad (1.16)$$

It follows that the free energy F can be expressed as a function of Z by

$$F = -k_B T \ln Z. \quad (1.17)$$

Grand Canonical ensemble

When defined in the Grand Canonical ensemble, the system can exchange energy and particles with a reservoir at a set temperature. Denoting N_i^a the number of particles of type a for a micro-state i , one can show that

$$p_i = \frac{\exp\left(-\frac{E_i - \sum_a N_i^a \mu_a}{k_B T}\right)}{\Xi}, \quad (1.18)$$

where μ_a is the chemical potential of the species a . The grand-canonical partition function can be defined as

$$\Xi = \sum_i \exp\left(-\frac{E_i - \sum_a N_i^a \mu_a}{k_B T}\right). \quad (1.19)$$

The grand-canonical function J then follows

$$J = -k_B T \ln \Xi. \quad (1.20)$$

Isobaric-Isothermal ensemble

The system can exchange energy and volume with a reservoir at a set temperature. Denoting V_i the volume of a micro-state i , one can show that

$$p_i = \frac{\exp\left(-\frac{E_i + PV_i}{k_B T}\right)}{Q}, \quad (1.21)$$

where P is the pressure of the reservoir, and the isobaric-isothermal partition function is

$$Q = \sum_i \exp\left(-\frac{E_i + PV_i}{k_B T}\right). \quad (1.22)$$

The Gibbs energy G is then defined by the relation

$$G = -k_B T \ln Q. \quad (1.23)$$

Ensemble averages and thermodynamic variable

Thermodynamic quantities can be computed from the ensemble function directly or from ensemble averages. For example, in the canonical ensemble, for a quantity A of conjugate B , we have

$$A = -\frac{\partial F(B)}{\partial B}. \quad (1.24)$$

If for a micro-state i we have $A_i = \frac{\partial E_i}{\partial B}$, then it is equal to the ensemble average

$$A = \frac{\sum_i \exp[-\beta E_i(B)] A_i}{\sum_i \exp[-\beta E_i(B)]}, \quad (1.25)$$

where $\beta = 1/k_B T$.

1.3.3 Dynamical quantities

The statistical average of a quantity $A(t)$ is

$$\langle A(t) \rangle = \sum_i p_i A_i(t), \quad (1.26)$$

where $A_i(t)$ is the value of A at time t for an initial micro-state i at $t = 0$.

Using the ergodic principle one can express this in terms of temporal averages at different starting points:

$$\langle A(t) \rangle = \lim_{T \rightarrow +\infty} \frac{1}{T} \int_0^T A(t+t') dt'. \quad (1.27)$$

1.3.4 Statistical thermodynamics of systems of classical particles

A system of general coordinates \mathbf{q} is usually described by an Hamiltonian \mathcal{H} function of \mathbf{q} and \mathbf{p} , the latter being the associated momentum. From Eq. 1.16, and with assumptions related to the classical limit, like $k_B T \gg \frac{h^2}{mL^2}$, where h is the Plank constant, m a mass (e.g. the mass of a particle) and L a dimension of the system (e.g. the length of the box containing the system, the length of a molecule), one can show that the partition function can be evaluated by the integral

$$Z = \int \cdots \int \frac{d^{n_f} \mathbf{p} d^{n_f} \mathbf{q}}{\mathcal{I} h^{n_f}} \exp\left(-\frac{\mathcal{H}(\mathbf{p}, \mathbf{q})}{k_B T}\right), \quad (1.28)$$

where n_f is the number of degrees of freedom of the system. \mathcal{I} is a factor taking into account the indiscernability of particles of a specie, reading

$$\mathcal{I} = \prod_{a=1}^{n_s} N_a!, \quad (1.29)$$

where n_s is the number of species and N_a the population of specie a .

When the system can be reduced to effectively point particles (e.g. spheres), the Hamiltonian is often equal to the sum of a kinetic part and a potential energy part,

$$\mathcal{H}(\mathbf{p}, \mathbf{q}) = K(\mathbf{p}) + U(\mathbf{q}), \quad (1.30)$$

with

$$K(\mathbf{p}) = \sum_{i=1}^N \frac{\vec{p}_i^2}{2m_i}, \quad (1.31)$$

where m_i is the mass of particle i . One can show that in this case the partition function can be integrated in the momenta space, so that

$$Z = \prod_{a=1}^{n_s} \frac{1}{N_a! \Lambda_a^{3N_a}} \int \cdots \int d^{n_f} \mathbf{q} \exp\left(-\frac{U(\mathbf{q})}{k_B T}\right), \quad (1.32)$$

where n_s is the number of species, a denotes a particular specie, N_a is the number of particles of the specie a , and Λ_a is the De Broglie length defined as

$$\Lambda_a = \frac{h}{\sqrt{2\pi m_a k_B T}}. \quad (1.33)$$

1.4 Simulation techniques

A summary of the simulation techniques, namely Monte-Carlo (MC) and Molecular Dynamics (MD), used in this work to compute thermodynamic and structural quantities is presented in this section. They are based on statistical mechanics. MD is a dynamic simulation and calculated properties are time-averaged properties. MC is a stochastic technique and works with ensemble average. It provides several advantages inherent to this technique: i) the equilibrium is quickly reached, ii) it allows the use of a large number of ensembles and iii) it allows unphysical displacements of the particles. We end this section with the specific simulation techniques used in this work with a special emphasis on the coarse graining techniques.

1.4.1 Monte-Carlo Simulations

One would like to compute ensemble averages like Eq. 1.25. It is often not possible analytically, and doing it naively requires the exploration of a huge configuration space. As not all micro-states are equally probable, hopefully many portions of the space can be neglected. A Monte-Carlo simulation generates a (pseudo-)random sequence of micro-states with a probability p_i for a micro-state i . Hence an ensemble average of a quantity A can be computed as

$$\langle A \rangle = \sum_i A_i, \quad (1.34)$$

where the sum is on the sequence of micro-states.

It can also be viewed as a stochastic process, more precisely a Markov chain. A Monte-Carlo move is done with the following procedure:

1. generate a new micro-state j from a micro-state i with a probability $\alpha(i \rightarrow j)$
2. Accept or reject the move with a probability $a(i \rightarrow j)$.

The transition probability is therefore $\Pi(i \rightarrow j) = \alpha(i \rightarrow j)a(i \rightarrow j)$. It must satisfy the balance condition

$$\sum_{j \neq i} \Pi(j \rightarrow i)p_j = \sum_{j \neq i} \Pi(i \rightarrow j)p_i. \quad (1.35)$$

An often used and more stringent constraint is the detailed balance, which reads

$$\Pi(j \rightarrow i)p_j = \Pi(i \rightarrow j)p_i. \quad (1.36)$$

If the detailed balance is satisfied and if step 1 is symmetric ($\alpha(i \rightarrow j) = \alpha(j \rightarrow i)$), the acceptance probability $a(i \rightarrow j)$ follows the relation

$$a(j \rightarrow i)p_j = a(i \rightarrow j)p_i. \quad (1.37)$$

The very commonly used Metropolis rule defines the acceptance probability as [52]

$$a(i \rightarrow j) = \min\left(1, \frac{p_j}{p_i}\right). \quad (1.38)$$

and respects detailed balance. It is particularly convenient for statistical ensembles because we can compute the ratio $\frac{p_j}{p_i}$ without knowing p_i itself. For example in the canonical ensemble, the Metropolis rule becomes

$$a(i \rightarrow j) = \min\left(1, \exp[-\beta(E_j - E_i)]\right). \quad (1.39)$$

Moves

Translation move For systems of particles the phase space of positions of N particles has to be explored. The simplest way to do that is to translate particles individually. A particle at position (x, y, z) is selected at random and set to a position of $(x + \Delta x, x + \Delta y, x + \Delta z)$, where Δx , Δy , and Δz are three random numbers in the interval $[-\Delta r/2, +\Delta r/2]$. Δr is a defined translation amplitude. The new movement is accepted or rejected with the Metropolis rule, see §1.4.1. Δr can be adjusted so that the average acceptance is equal to a goal value. In practice it is generally believed than a value of less than 50 % yields optimum results (faster convergence)[52].

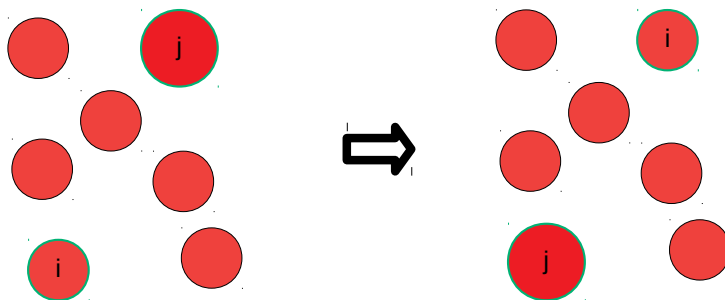


Figure 1.1: Swap move: two particles i and j picked at random swap their positions

Swap move For systems composed of different types of particles, typically of concern to this work, size and charge polydisperse particles, the swap move[53, 54] is found to be a very efficient move to sample the phase space and to reach the equilibrium state faster. Indeed, in Chapter 4 it allowed concentrated colloidal systems to explore configurations unreachable in practice with only single particles displacements or MD simulations. It consists in picking two particles at random and swapping their positions, see Figure 1.1. The new configuration is accepted with the probability defined by the Metropolis rule, that is,

$$a_{swap} = \min(1, \exp(-\beta(U(\vec{r}_i = \vec{r}_{jo}, \vec{r}_j = \vec{r}_{io}) - U(\vec{r}_i = \vec{r}_{io}, \vec{r}_j = \vec{r}_{jo}))))), \quad (1.40)$$

where i and j are the particles to be swapped, \vec{r}_{io} and \vec{r}_{jo} are their respective positions in the old configuration, and U is the potential energy defined above.

Volume moves To implement the isobaric-isothermal ensemble, or NPT , where in addition to the number of particles N and the temperature T , the pressure P is maintained constant, one needs to allow the volume of the simulation box to fluctuate. This is done by trying random contractions or expansions of the simulation box. Such a volume change can be generated as follow,

$$\begin{cases} V_{new} = V_{old} + \Delta V \\ \vec{r}_{i,new} = \vec{r}_{i,old} \times \left(\frac{V_{new}}{V_{old}}\right)^{1/3} \quad \forall i = 1, \dots, N, \end{cases} \quad (1.41)$$

where V_{old} and V_{new} are the old and new volume and ΔV is the volume difference generated randomly between $-\Delta V_{max}/2$ and $+\Delta V_{max}/2$. The species positions r_i are rescaled according to the new volume. The acceptance probability can be deduced from Eq. 1.38 and Eq. 1.21 and reads

$$a_{NPT} = \min\left(1, \left(\frac{V_{new}}{V_{old}}\right)^N \exp(-\beta(U_{new} - U_{old}))\right). \quad (1.42)$$

Alternatively, one can prefer to change the *logarithm* of the volume, as in this case the change in volume becomes proportional to the initial volume. In addition, the new volume is always positive. The transformation becomes

$$\ln V_{new} = \ln V_{old} + \Delta \ln V, \quad (1.43)$$

where $\Delta \ln V$ is a random number generated between $-\Delta \ln V_{max}/2$ and $+\Delta \ln V_{max}/2$.

The acceptance probability then reads

$$a_{NPT} = \min \left(1, \left(\frac{V_{new}}{V_{old}} \right)^{N+1} \exp(-\beta(U_{new} - U_{old})) \right). \quad (1.44)$$

Particle insertion and deletion When simulating in the grand-canonical ensemble (μVT), the particles move in and out the simulation box according to their chemical potential $\{\mu\}_{a=1,\dots,n_s}$ set by a connected reservoir. In practice this means that the numbers of particles, $\{N_a\}_{a=1,\dots,n_s}$, are allowed to fluctuate by trying random additions or deletions in the simulation box. The acceptance probabilities for these moves can be deduced from Eq. 1.38 and Eq. 1.18. For addition, the acceptance criteria for a particle a is

$$a_{\mu VT,add} = \min \left(1, \frac{V}{(N_a + 1)\Lambda_a^3} \exp(-\beta(U_{new} - U_{old} - \mu_a)) \right), \quad (1.45)$$

and for deletion it is

$$a_{\mu VT,del} = \min \left(1, \frac{N_a \Lambda_a^3}{V} \exp(-\beta(U_{new} - U_{old} + \mu_a)) \right), \quad (1.46)$$

where Λ_a is defined in Eq. 1.33. In charged systems, these moves must be handled with care such as to maintain electroneutrality in the box. This is done by adding or deleting several chemical species simultaneously whose total charge is zero. As an example, in a system containing Na^+ and Cl^- ions, the insertion of a neutral NaCl salt pair has the acceptance probability

$$a_{\text{NaCl},add} = \min \left(1, \frac{V^2}{(N_{\text{Na}} + 1)\Lambda_{\text{Na}}^3 (N_{\text{Cl}} + 1)\Lambda_{\text{Cl}}^3} \exp(-\beta(U_{new} - U_{old} - \mu_{\text{NaCl}})) \right). \quad (1.47)$$

1.4.2 Molecular Dynamics

The basics of Molecular Dynamics (MD) consists in integrating the equations of movements of Newton,

$$(1.48)$$

$$\vec{v}_i = \frac{d\vec{r}_i}{dt} \quad (1.49)$$

$$m_i \frac{d\vec{v}_i}{dt} = \vec{F}_i \quad (1.50)$$

$\forall i = 1, \dots, N$. \vec{F}_i is the force acting on the particle i . For conservative systems, it is equal to $\frac{\partial U}{\partial \vec{r}_i}$, where U is the potential energy. A common way to solve these equations

numerically is to discretize the trajectory into timesteps of duration Δt . An algorithm to compute velocities and positions is needed, for example the Velocity-Verlet algorithm

$$\vec{r}_i(t + \Delta t) = \vec{r}_i(t) + \Delta t \vec{v}_i(t) + \frac{\Delta t^2}{2m_i} \vec{F}_i(t) \quad (1.51)$$

$$\vec{v}_i(t + \Delta t) = \vec{v}_i(t) + \frac{\Delta t}{2m_i} (\vec{F}_i(t) + \vec{F}_i(t + \Delta t)) \quad (1.52)$$

$\forall i = 1, \dots, N$. This is for the microcanonical ensemble. For the canonical ensemble, one has to introduce some sort of energy exchange with a thermostat at a given temperature T . For example the velocity-rescaling thermostat[55], for which, as its name might indicate, the velocity is rescaled periodically by a random factor in order to obtain a Boltzmann distribution of velocities corresponding to the wanted temperature. In this work, we used the well-optimized and well-tested Gromacs[56] software package.

1.4.3 Boundary Conditions and Long Range Interactions

Boundary conditions

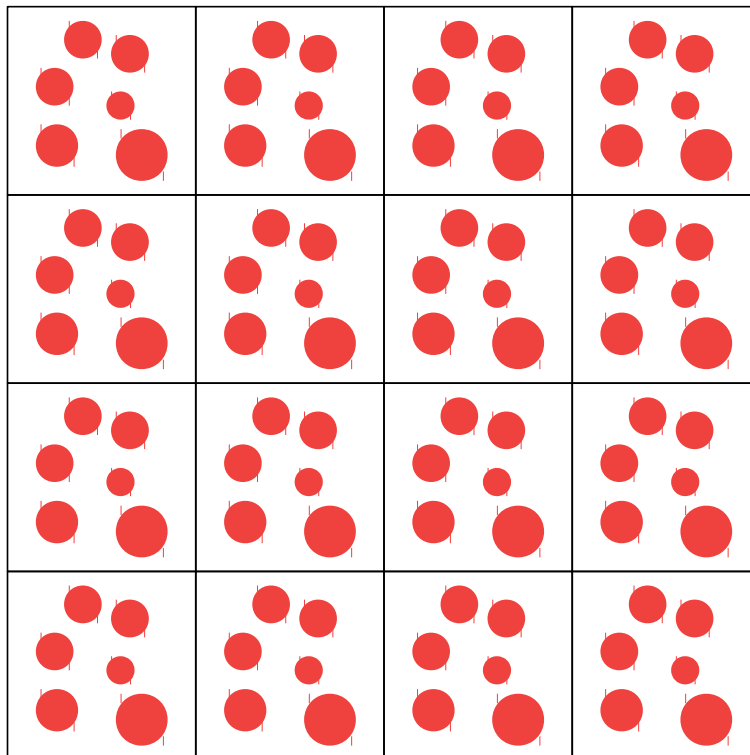


Figure 1.2: Schematic 2D representation of periodic boundary conditions.

Simulations of microscopic systems either by Monte Carlo or Molecular Dynamics aim to extract and in the best case predict macroscopic observables and quantities of a macroscopic sample. Typically in our work we compute thermodynamic properties. Yet, the number of particles that can be handled with today's best super-computers do not exceed a few million, not to speak of the every-day computers. Clearly, this number is still far from the thermodynamic limit. One thus relies on numerical artifices to mimic the presence of an infinite bulk surrounding our N particle model system. In some special cases, one can make use of hard or soft walls, like for example systems that can be reduced to a cell model (see e.g. §1.5). More generally, it is achieved by employing periodic boundary conditions. The simulation box is treated as a unit cell infinitely repeated over space in a periodic lattice, see Figure 1.2. A particle thus now interact with all other particles in the primary cell as well as all particles in all cell replicas. One should note that, although very successful to suppress edge effects, the use of periodic boundary conditions can still give rise to finite-size effects, in particular, spurious correlations induced by the periodicity of the cell images.

Minimum image

When the range of interactions is smaller than the length of the simulation box the minimum image convention is a convenient and efficient approximation to be used. In this convention only the first images of the primary cell is accounted in the particle interaction calculation. Typically, in the one component simulations in Chapter 2 and Chapter 4 such a convention was used.

Ewald summation

In the case of long range interactions such as the electrostatic interactions, the first image convention may not suffice and one may like to include all cell images. However, a brute force calculation of the involved summations is shown to be poorly convergent. The Ewald summation has been shown to circumvent this problem and is probably the most commonly used boundary condition method. The basic principles is schematically described in Figure 1.3. It rests on the idea that a system composed of point charges may be considered as a sum of two terms that is a set of screened charged minus the smoothly varying screening background. The screened charge clouds, with a Gaussian distribution,

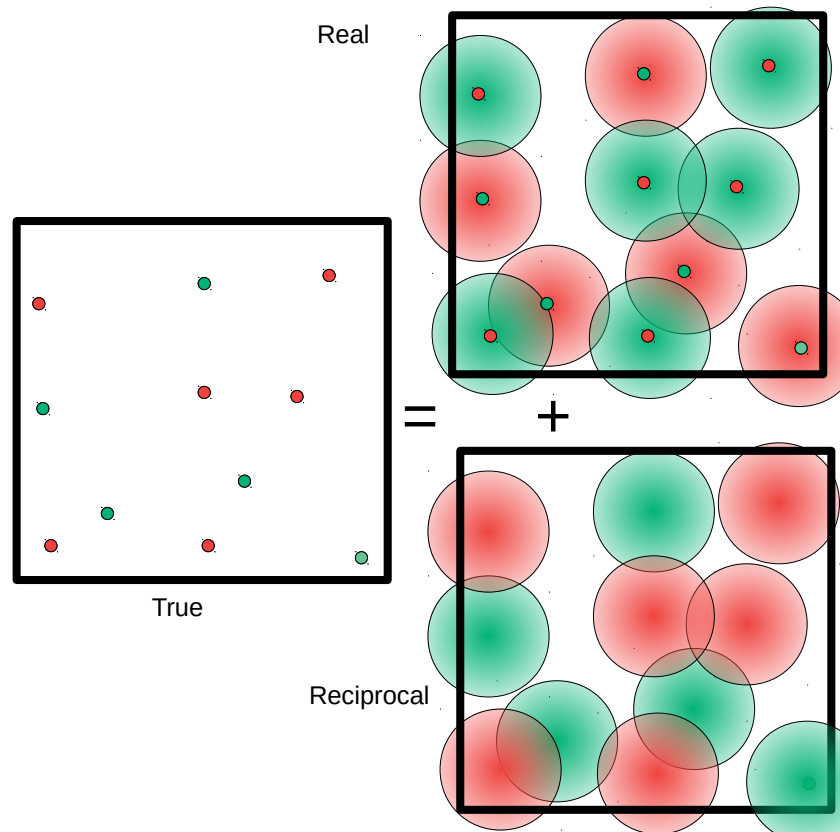


Figure 1.3: Division of the charges for the Ewald summation. The charge density (originally composed of point charges, left box) is divided into two charge densities. In the upper box the point charges are screened by charge clouds, leading to a fast converging sum in the real space. In the lower box, the compensating charge distribution, which yields to a fast converging sum in the reciprocal space. By convention red charges are positive, and green ones are negative.

compensate the point charges, such that the generated electrostatic potential is now a rapidly decaying function of the distance r and can thus be easily computed in the real space. The second term is used to correct for the introduction of the screened charge cloud to every particles. It turns out that the compensating charge distribution is a smooth function but is also periodic and rapidly convergent when represented by Fourier series in the reciprocal space. In short, the electrostatic potential energy can be written as a sum of three terms: a sum in the real space, a sum in the reciprocal space and a constant term (correction for self-interactions). One can show that the electrostatic potential energy \mathcal{U}^{el} reads

$$U^{el} = \frac{1}{2V} \sum_{\mathbf{k} \neq 0} |\rho(\mathbf{k})|^2 \frac{4\pi}{k^2} \exp\left(-\frac{k^2}{4\alpha}\right) - \left(\frac{\alpha}{\pi}\right) \sum_{i=1}^N q_i^2 + \frac{1}{2} \sum_{i \neq j}^N \frac{q_i q_j \operatorname{erfc}(\sqrt{\alpha} r_{ij})}{r_{ij}}, \quad (1.53)$$

where \mathbf{k} is a wave vector, $\rho(\mathbf{k})$ is the particle density in the reciprocal space, and α is a adjustable parameter of the Gaussian function (that defines the screening cloud). The coulomb-like potential in the real space sum is damped when $\alpha > 0$, which allows to use cutoff schemes like for short-range interactions. The computation can be improved by more advanced techniques like Particle Mesh Ewald(PME) [52], where the computation of the reciprocal space sum can be improved by approximating the charge distribution with a mesh, enabling the use of Fast Fourier Transforms.

Fennell method

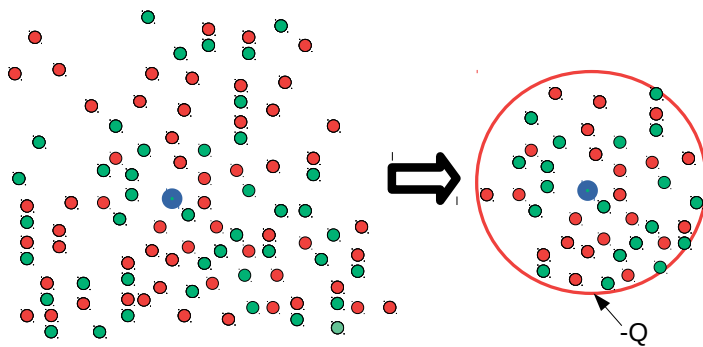


Figure 1.4: Illustration of the Fennell method to deal with the long range electrostatic interactions. The method uses a truncated and shifted potential which takes a nil value beyond a given cutoff radius, r_c . A self-image charge Q is further employed to neutralize each cutoff sphere. Q is placed on the cutoff sphere.

An efficient alternative to the Ewald summation is the Fennel method[57] which is particularly suitable for homogeneous systems such as a particle dispersion or a bulk solution. The method is an extension of the work of Wolf et al[58]. Wolf et al observed that the Coulomb interactions were rather short range in condensed phase systems and that neutralization of the charge is crucial for potential stability. They thus devised a pairwise and spherically truncated summation method that ensures charge neutrality through placement on the cut-off sphere of a self-image charge, see Figure 1.4. The Fennel method is not based on a shifted potential as the Wolf method but a shifted force. Contrary to the shifted potential form which only ensures that the potential is smooth at the cutoff radius, r_c , this presents the advantage that both the potential and the forces go to zero at r_c . The Fennel electrostatic energy reads

$$U_{Fennel} = \sum_{\substack{i \neq j \\ r_{ij} < r_c}} \frac{q_i q_j}{4\pi\epsilon} \left(\frac{1}{r_{ij}} + \frac{r_{ij}}{r_c^2} - \frac{2}{r_c} \right). \quad (1.54)$$

r_c is generally set to half the box length for a better accuracy. This method may not match the Ewald summation in terms of accuracy. However, it is much simpler. In §1.4.4, a comparison of the inter-colloid force as obtained from using the Ewald summation and the Fennel method for the long range electrostatic interactions is made.

Potential truncation

Let us now consider the case that we perform a simulation of a system with short range interactions. One might think here of a LJ particle system but it can be extended to any system where the interactions of the particle is dominated by its first neighbors. This is the case in Chapters 2 and 4 where a colloidal dispersion is modeled with charged hard spheres that interact only through a pair potential $w^*(r)$. The simplest method to truncate potentials is to ignore all the interaction beyond a given cutoff radius, r_c . The simulations are then performed with the pair potentials,

$$u_{ij}(r) = \begin{cases} w^*(r) & \text{when } r \leq r_c \\ 0 & \text{otherwise} \end{cases} \quad (1.55)$$

The use of r_c considerably reduces the computational time of the simulations. Although the contribution of a single pair potential is very small, when $r > r_c$, the number of neglected pairs increases rapidly with r such as the total tail potential energy, U_{tail} ,

becomes non negligible. An accurate potential energy and pressure can, however, be obtained *a posteriori* with a tail correction term. The tail corrections assume a smooth and mean density of the particles given by their radial distribution function, defined below in Eq. 1.88. In the case of monodisperse suspension it reads[52] for U_{tail} ,

$$U_{tail} = \frac{1}{2} \int_{r_c}^{\infty} dr 4\pi r^2 \rho g(r) w^*(r). \quad (1.56)$$

and for the pressure correction term

$$P_{tail} = \frac{1}{2} \int_{r_c}^{\infty} dr 4\pi r^2 \rho^2 g(r) r \frac{\partial w^*(r)}{\partial r}. \quad (1.57)$$

The $1/2$ term in front of U_{tail} and P_{tail} is there to avoid double counting of particle interactions. The extension of the correction terms involving a mixture of chemical species (e.g. polydisperse systems) is straightforward.

Cell decomposition

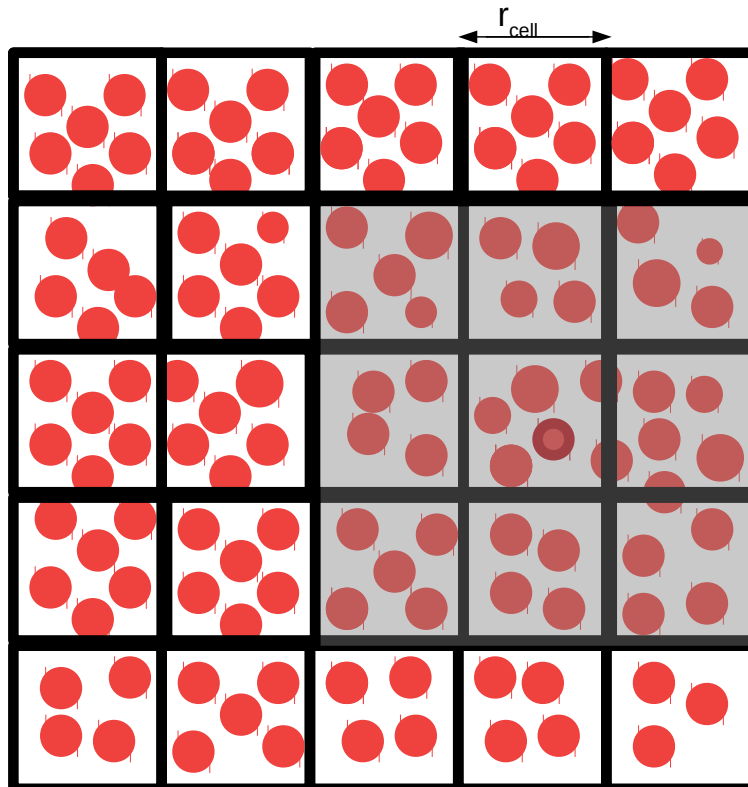


Figure 1.5: Decomposition of the box in cells of equal width. The gray area contains the particles to look for when working out the energy of the marked particle.

When inter-particle interactions can be truncated, see §1.4.3, and r_c is smaller than a quarter of the simulation box length L , an important speed up of the computation time can be obtained with the use of the cell decomposition method[59]. Within this method, the box is divided into cubic cells of length larger than or equal to the interaction cutoff, see Fig 1.5. Each particle is affected to a cell and then only its interactions with the particles belonging to the same cell and the first neighbor cells have to be computed. The time scaling for the update of the cell list, which is $\mathcal{O}(N^2)$, can be made $\mathcal{O}(N)$ using a double linked list. All in all, a linear scaling of the simulation time with the system size can be obtained. This is illustrated in Figure 1.6 which compares the simulation time per MC cycle (N translation attempts) versus N for a colloidal system typical of those studied in Chapter 2 and Chapter 4.

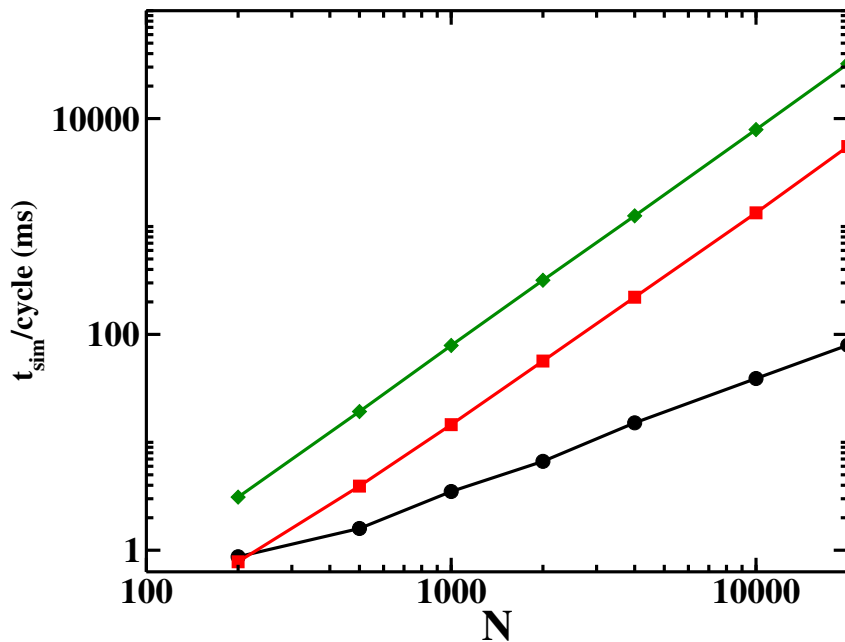


Figure 1.6: Duration of a MC simulation versus the number of particles N . Conditions: monodisperse ($R = 13.75$ nm), pH = 9, I = 5 mM, $\phi = 0.1$. Cutoff radius is 71.5 nm. Implementations are: Cell Decomposition (black), Cutoff (Red), Minimum Image (Green),

1.4.4 Coarse-graining Interactions

In colloidal suspensions, coarse-graining consists in reducing the system to fewer components by averaging out the degrees of freedom of the solvent and/or of the ions. Let (\mathbf{p}, \mathbf{q}) be the (momenta, positions) of the species to be averaged out, n_f the number of degrees

of freedom for these species, and (\mathbf{P}, \mathbf{Q}) the (momenta, positions) of the species to be kept. The coarse-grained model is described by an effective Hamiltonian \mathcal{H}_{eff} reading

$$\mathcal{H}_{eff}(\mathbf{P}, \mathbf{Q}) = -k_B T \ln \left[\int \cdots \int \frac{d^{n_f} \mathbf{p} d^{n_f} \mathbf{q}}{\mathcal{I} h^{n_f}} \exp \left(-\frac{\mathcal{H}(\mathbf{P}, \mathbf{Q}, \mathbf{p}, \mathbf{q})}{k_B T} \right) \right], \quad (1.58)$$

where \mathcal{H} is the original Hamiltonian of the system and \mathcal{I} is defined in Eq. 1.29. \mathcal{H}_{eff} can be approximated by effective pair potentials,

$$\mathcal{H}_{eff} \approx K + \sum_{i < j} w_{ij}^*(r_{ij}), \quad (1.59)$$

where K is the kinetic part, and w_{ij}^* is the effective potential between particles i and j .

w^* can be obtained from sampling the pair potential of mean force. For charged colloid systems at finite particle volume fraction ϕ a convenient approach consists in using a single colloid pair enclosed either in a cylindrical cell [60, 61] or in cubic box with periodic boundary conditions (PBC) [62], such as the volume ratio of the colloid pair to that of the cell (box) is equal to ϕ . However, due to boundary artifacts, colloid images or hard cell walls, the range of ϕ is limited to the dilute or semi-dilute regime. In Chapter 2 we propose and develop the idea that this limitation can be circumvented by the combined use of an excess counterion concentration, to mimic a finite ϕ , in a large enough simulation box with PBC and of a uniform charged background, to neutralize the overall system. The potential of mean force was extracted from the calculation of the inter colloid force (F_t) at fixed colloid positions D , followed by the integration of the latter, $w^*(D) = -\int_D^\infty F_t(r) dr$. Below the mean force calculation of a colloid pair with a uniformed charged background is described.

When simulations in the full primitive model are affordable, reverse Monte Carlo simulation methods can be employed to evaluate w^* . One of those, called the iterative Boltzmann inverse (IBI), was used in Chapter 2 and the results compared to those obtained with the charged background method. Following the force calculation, the IBI is described in some details.

Forces between two particles

Let us consider the system pictured in Figure 1.7 which consists of two spherical and charged colloids aligned on the x axis of a cubic box of length L with PBC filled with a salt solution containing N_I ions and N_e counterions in excess compensated by an homogeneous

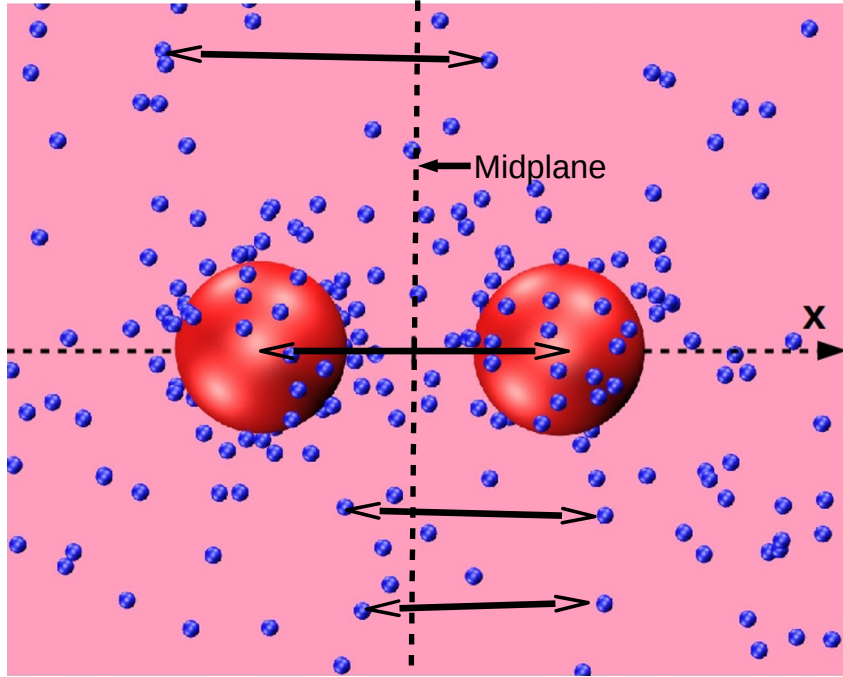


Figure 1.7: Illustration of the calculation of the force over the midplane. Only interactions between particles from different sides of the midplane are computed.

charged background (pink). The colloids and ions are further assumed to interact through shifted and truncated Lennard-Jones (SLJ) potentials, see Eq. 1.4.

The mean force between the pair of colloids at a given background charge (or equivalently volume fraction) can be evaluated at contact for fixed center-to-center separations D . It can be expressed as,

$$\begin{aligned}
 F_t(D) = & -\frac{\partial u^{el}(D)}{\partial D} - \frac{\partial u^{SLJ}(D)}{\partial D} \\
 & - \left\langle \sum_{i=1}^{N_I} \frac{\partial u_{ic}^{el}(r)}{\partial r} \Big|_{r=r_{ic}} + \sum_{i=1}^{N_I} \frac{\partial u_{ic}^{SLJ}(r)}{\partial r} \Big|_{r=r_{ic}} \right\rangle \\
 & - \left\langle \sum_{i=1}^{N_e} \frac{\partial u_{ic}^{el}(r)}{\partial r} \Big|_{r=r_{ic}} + \sum_{i=1}^{N_e} \frac{\partial u_{ic}^{SLJ}(r)}{\partial r} \Big|_{r=r_{ic}} \right\rangle
 \end{aligned} \tag{1.60}$$

where the two first terms are the direct Coulomb and LJ forces between the colloids. The four last are the ensemble average of the electrostatic and LJ forces exerted on the colloids by the small ions. It can be noted that the contact force exerted on the colloids by the charged background is centro-symmetric and, thus, cancels out.

The mean force can also be computed across the mid-plane ($x = 0$) for a fixed center-to-center separation D along the x-axis of the simulation box. By doing so, the total

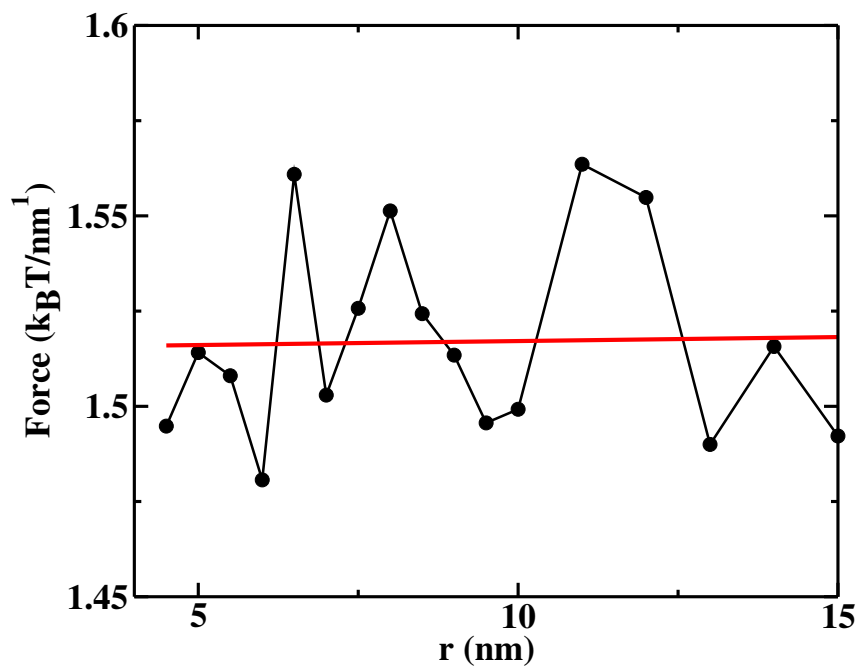


Figure 1.8: Background charge term of the inter-colloid force over the midplane, $F_{back}^{el}(r, \phi)$, as obtained at different center-to-center colloid separations for two colloids placed in a cubic box with PBC filled with an excess of monovalent counterions such that $\phi = 3.3\%$. The diameter of the colloids is 4 nm and their charge is $-60e$. The red line is a fit to the computed values (black line with circles). See the text for more details.

mean force can be divided in four terms as follow

$$F_t(D) = F^{el}(D) + F^{LJ}(D) + F^{id}(D) + F_{back}^{el}(D). \quad (1.61)$$

The electrostatic, $F^{el}(D)$, and LJ, $F^{LJ}(D)$, terms are respectively calculated by summing all the Coulomb and LJ forces between the species residing on different side of the midplane. The third term, $F^{id}(r)$, is the ideal contribution which can be conveniently defined as,

$$\beta F^{id}(D) = [\rho_I(x=0) - \rho_I(x=L/2)]L^2, \quad (1.62)$$

where $\rho_I(x=0)$ and $\rho_I(x=L/2)$ are the ion densities at the midplane and at one end of the simulation box. The fourth term, $F_{back}^{el}(D)$, stems from average electrostatic force over the midplane of the charged background with the charged species and with itself. We solved it numerically from the calculation of the contact force applied to the colloids (insensitive to the background charge), whose computation is straightforward but has poorer statistics compared to the midplane calculations. The difference between the contact force and the sum of the other terms of the force over the midplane provides a first estimate of F_{back}^{el} . The latter is then collected as a function of colloid separation and finally fitted by a straight line to give the final values. Figure 1.8 provides an example.

The electrostatic interactions were computed with the Fennell potential, introduced above in §1.4.3. Calculations of the contact force, using the Particle Mesh Ewald (PME) method implemented by Gromacs, were also made to check the accuracy of the Fennell potential. The simulations were performed using the charge background method for a system composed of charged spherical colloids of radius 2 nm and charge -60 e with explicit monovalent counter-ions at a particle volume fraction of 6.7%. Figure 1.9 gives a comparison of the inter-colloidal force computed with PME and the Fennell Hamiltonian. It shows that within the statistical uncertainties the mean forces are virtually the same for such systems.

Iterative Boltzmann inverse

Iterative Boltzmann inverse calculations[63, 64] (IBI) allows to compute an effective pair potential (e.g. between colloids) with the radial distribution function (RDF) (see §1.6.1) as input. Let us denote c the specie (e.g. colloids) we wish to compute the effective pair potential $w^*(r)$ and $g(r)$ the RDF already calculated with the full primitive model (e.g.

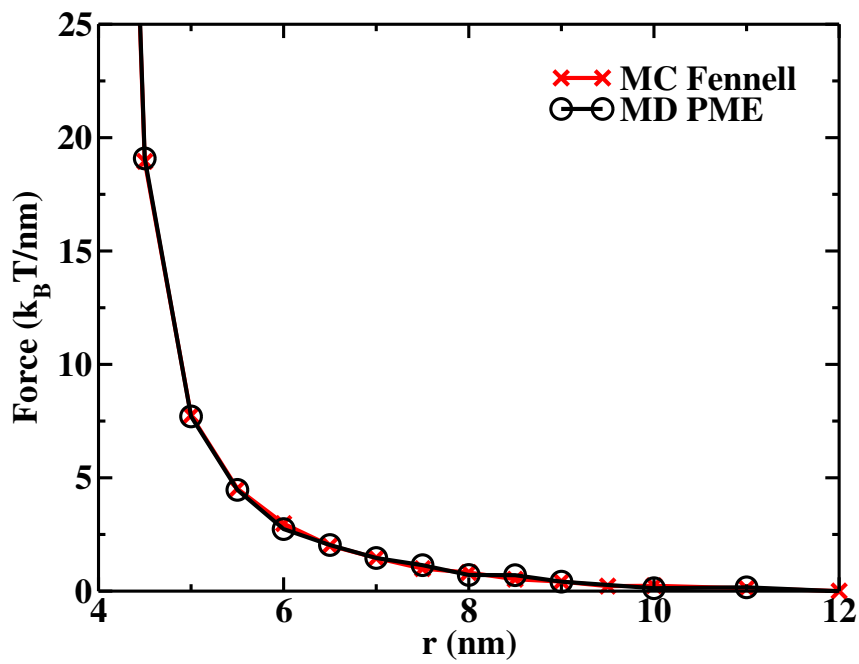


Figure 1.9: A comparison of the inter-colloidal force as obtained from the Fennell Hamiltonian (red crosses) and from Particle Mesh Ewald (black squares) using the background charge method. The simulations were performed with two colloids placed in a cubic box with PBC filled with an excess of monovalent counterions corresponding to $\phi = 6.7\%$. The radius and charge of the colloids are set to 2 nm and $-60 e$, respectively.

the primitive model with colloids and explicit ions). For a given pair potential $w_0^*(r)$ one can work out the radial distribution function $g_0(r)$ in the one-component model with only c . Likely $g_0(r)$ differs significantly from $g(r)$ but a correction can be made as a first approximation to form a new effective pair potential $w_1^*(r)$, reading

$$w_1^*(r) = w_0^*(r) - k_B T \ln \frac{g_0(r)}{g(r)} \quad (1.63)$$

This is related to the potential of mean force, equal to $-k_B T \ln g(r)$, which is equal to $w^*(r)$ at infinite dilution. This suggests an iterative procedure, the iteration from $w_{n+1}^*(r)$ $w_n^*(r)$ at step n reads

$$w_{n+1}^*(r) = w_n^*(r) - k_B T \ln \frac{g_n(r)}{g(r)}. \quad (1.64)$$

To be repeated until convergence. A natural choice for the first guess $w_0^*(r)$ is $-k_B T \ln g(r)$.

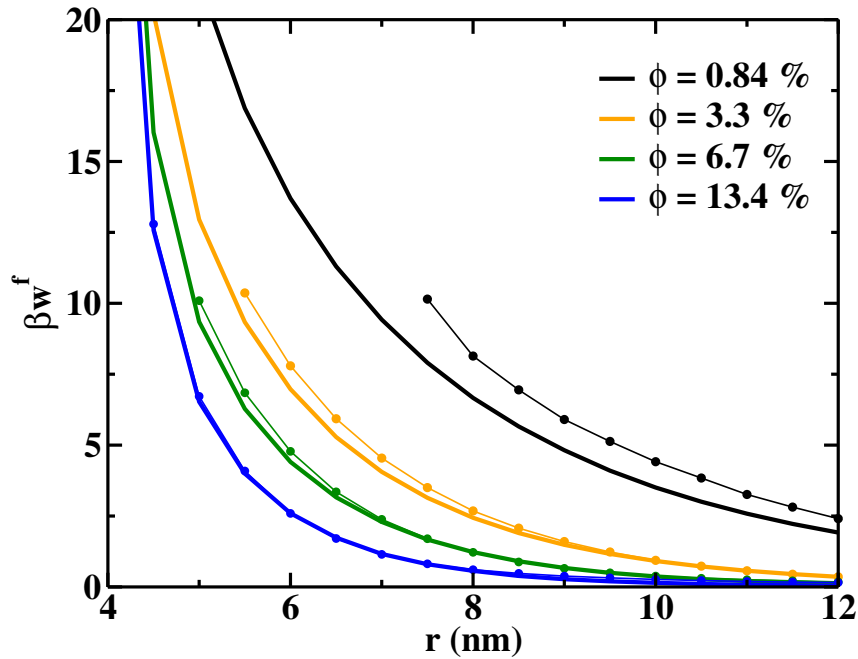


Figure 1.10: Comparison between the inter-colloidal effective pair potential obtained from background charge simulations (thick lines) and interactive Boltzmann inverse simulations (thin lines with circles) for various particle volume fractions. The counterions are monovalent. The IBI potentials are not displayed down to the hard-core diameter, lacking good enough statistics for these small colloid separations.

Figure 1.10 compare the so obtained potentials with those computed from background charge simulations for monovalent counterions. For all volume fractions and ion types (not shown), the IBI potential is higher, showing that our method tends to overestimate the

screening of the electrostatic repulsions but gives more reliable results as ϕ is increased, i.e. the ϕ range for which it has been designed.

1.5 Mean-Fields Approaches

Alternative methods to the full primitive model simulations introduced in the previous section to calculate the effective pair potential between the colloids can be based on solving the cell model[65] and the Bjerrum model[66] at the mean field level of approximation. In Chapter 3, the methods are generalized and applied to an aqueous dispersion of titratable colloids with continuous size polydispersity. It should be stressed, however, that these mean field approaches are not applicable to highly coupled systems, i.e. highly charged particles and aqueous solutions with high salt concentration or multivalent counterions. In this section we introduce briefly the Poisson-Boltzmann equation (PBE) as well as the cell and the renormalized jellium model. The numerical method used to solve the PBE for these two models is further described.

1.5.1 Poisson equation

In the primitive model, one can write the Poisson equation for the electrostatic field $\mathcal{V}(\vec{r})$ as

$$\epsilon \Delta \mathcal{V}(\vec{r}) + \rho_e(\vec{r}) = 0, \quad (1.65)$$

where Δ the Laplacian, ϵ is the dielectric permittivity of the solvent, and $\rho_e(\vec{r})$ is the electrical charge density, that depends on the positions of the ions. The mean-field approximation applied here consists in replacing the electrostatic field that depends on the instantaneous positions of the ions by its average value. A further approximation can be made by neglecting the non-electrostatic interactions between ions, that is approximating the system to an ideal gas plus an external potential. This leads to the Poisson-Boltzmann equation.

1.5.2 Poisson-Boltzmann equation

The Poisson-Boltzmann Equation (PBE) reads[67]

$$\epsilon \Delta \mathcal{V}(\vec{r}) + \sum_{\alpha=1}^{n_I} q_{\alpha} c_{\alpha}(\vec{r}) + \rho_e(\vec{r}) = 0, \quad (1.66)$$

where n_I is the number of ion species, q_α is the electrical charge of the ion α , $c_\alpha(\vec{r}) = c_{s,\alpha} \exp\left(\frac{-q_\alpha \mathcal{V}(\vec{r})}{k_B T}\right)$ is the concentration of the ion α , $c_{s,\alpha}$ being the concentration of the salt in the reservoir. ρ_e is a charge density (specified later according to the model), k_B is the Boltzmann constant, and T is the temperature. For convenience, we will use a reduced form of this equation with less explicit parameters, by defining the dimensionless potential $\psi = \frac{e\mathcal{V}}{k_B T}$, where e is the elementary charge, $z_\alpha = q_\alpha/e$ is the charge number for each ion α , $\xi = \rho_e/e$, and $\lambda_B = \frac{e^2}{4\pi k_B T \epsilon}$ is the Bjerrum length. One can show that

$$\Delta \psi(\vec{r}) + 4\pi\lambda_B \left[\sum_{\alpha=1}^{n_I} z_\alpha c_{s,\alpha} \exp(-z_\alpha \psi(\vec{r})) + \xi(\vec{r}) \right] = 0. \quad (1.67)$$

1.5.3 Cell Model

In a colloidal dispersion, the closeness of colloids tend to push ions towards them. In a monodisperse colloidal crystal, the periodicity implies that the volume can be divided into identical electroneutral Wigner-Seitz cells[65], and, as an approximation, the thermodynamics of the dispersion can be reduced to a cell. In this Cell Model(CM), one colloid is enclosed in a cell. Typically one wants to use a spherical cell for a spherical colloid. In this case, Eq. 1.67 can be simplified because of the radial symmetry, and $\xi(\vec{r}) = 0$. The PBE becomes

$$\frac{\partial^2 \psi(r)}{\partial r^2} + \frac{2}{r} \frac{\partial \psi(r)}{\partial r} + 4\pi\lambda_B \left[\sum_{\alpha=1}^{n_I} z_\alpha c_{s,\alpha} \exp(-z_\alpha \psi(r)) \right] = 0 \quad (1.68)$$

For a colloid of radius R_p and surface charge density σ and a cell of radius R_c , the boundary conditions are

$$\left. \frac{\partial \psi}{\partial r} \right|_{r=R_p} = -4\pi\lambda_B \sigma \quad (1.69)$$

$$\left. \frac{\partial \psi}{\partial r} \right|_{r=R_c} = 0 \quad (1.70)$$

The volume fraction is

$$\Phi = \left(\frac{R_p}{R_c} \right)^3 \quad (1.71)$$

The osmotic pressure of the dispersion is obtained by noting that the ionic pressure at the edge of the cell represents the ionic pressure in the dispersion by continuity. Hence the osmotic pressure in this model is

$$\Pi = k_B T \rho_p + k_B T \sum_{\alpha=1}^{n_I} c_{s,\alpha} (\exp(-z_\alpha \psi(R_c)) - 1), \quad (1.72)$$

where ρ_p is the colloidal concentration.

1.5.4 Renormalized Jellium Model

In the Renormalized Jellium Model(RJM)[66], the colloids surrounding one colloid are represented by a background charge, that can be uniform and constant if the radial distribution function $g(r) = 1$. For a spherical colloid the PBE becomes

$$\frac{\partial^2 \psi(r)}{\partial r^2} + \frac{2}{r} \frac{\partial \psi(r)}{\partial r} + 4\pi \lambda_B \left[\sum_{\alpha=1}^{n_I} z_\alpha c_{s,\alpha} \exp(-z_\alpha \psi(r)) + \xi_{back} \right] = 0, \quad (1.73)$$

where ξ_{back} is the reduced density of the background charge. For a colloid of radius R and surface charge density σ and a cell or radius R_p , the boundary conditions are

$$\left. \frac{\partial \psi}{\partial r} \right|_{r=R} = -4\pi \lambda_B \sigma \quad (1.74)$$

$$\left. \frac{\partial \psi}{\partial r} \right|_{r \rightarrow \infty} = 0 \quad (1.75)$$

As a first try, one can set the background charge to $Z_p \rho_p$, where Z_p is the charge of a colloid. However, as colloids can be seen as surrounded by a cloud of counter-ions, a better approach would be to set ρ_{back} to $Z_p^* \rho_p$, where Z_p^* is the *renormalized* charge. The latter is defined by the asymptotic expression of $\psi(r)$ at infinity, $\psi_a(r)$, which takes the form

$$\psi_a(r) = \psi_D + \lambda_B \frac{Z_p^*}{1 + \kappa^* R_p} \frac{\exp(-\kappa^* r)}{r} + \dots, \quad (1.76)$$

where κ^* is the renormalized screening length and ψ_D is so that $\xi_{back} = \sum_{\alpha}^{n_I} z_\alpha c_{s,\alpha} \exp(-z_\alpha \psi_D)$. Z_p^* and κ^* can be computed by fitting the tail of $\psi(r)$ if one has solved Eq. 1.73 for a given ξ_{back} . One has therefore to iterate values of ξ_{back} until $Z_p^*(\xi_{back}) = Z_p \rho_p / \xi_{back}$. The osmotic pressure is then given by

$$\Pi = k_B T \rho_p + k_B T \sum_{\alpha=1}^{n_I} c_{s,\alpha} [\exp(-z_\alpha \psi_D) - 1]. \quad (1.77)$$

1.5.5 Numerical resolution of the Poisson–Boltzmann Equation

Here we describe how the PBE in the CM and the RJM is solved. For a spherical particle of radius R with a surface potential ψ_0 placed in a spherical cell of radius R_p the PBE and boundary conditions are

$$\begin{cases} \frac{\partial^2 \psi}{\partial r^2} + \frac{2}{r} \frac{\partial \psi}{\partial r} + 4\pi \lambda_B [\sum_{\alpha=1}^{n_I} z_\alpha c_{s,\alpha} \exp(-z_\alpha \psi(r)) + \xi(r)] = 0 \\ \psi(R) = \psi_0 \\ \left. \frac{\partial \psi}{\partial r} \right|_{r=R_p} = 0. \end{cases} \quad (1.78)$$

Note that for the RJM, one must choose a cell radius large enough such as $\psi(r) \approx \psi_D$ at the edge of the cell. This system of equations is numerically solved using an “in house” code based on Newton Gauss-Seidel iterations[68]. In brief, Eq. 1.78 is discretized into $N + 2$ intervals of length h :

$$L_k(\boldsymbol{\psi}) = 0 \quad \forall k = 1, \dots, N \quad , \quad (1.79)$$

with $\boldsymbol{\psi}$ the vector $(\psi_0 \psi_1 \dots \psi_{N+1})$ and

$$L_k(\boldsymbol{\psi}) = \frac{\psi_{k+1} + \psi_{k-1} - 2\psi_k}{h^2} + \frac{\psi_{k+1} - \psi_{k-1}}{hr_k} + 4\pi\lambda_B \left[\sum_{\alpha=1}^{n_I} z_\alpha c_{s,\alpha} \exp(-z_\alpha \psi_k) + \xi(r_k) \right], \quad (1.80)$$

for all $k = 1, \dots, N$. The boundary condition at the edge of the cell ($r_{N+1} = R_p$) is

$$\psi_{N+1} = \psi_N \quad (1.81)$$

The system of algebraic nonlinear equations defined by Eq. 1.79 is then solved iteratively.

A Newton step $p + 1$ updates $\boldsymbol{\psi}$ at step p , $\boldsymbol{\psi}^{(p)}$, to

$$\begin{cases} \psi_k^{(p+1)} = \psi_k^{(p)} - \frac{F_k(\boldsymbol{\psi}^{(p)})}{\left. \frac{\partial L_k(\boldsymbol{\psi})}{\partial \psi_k} \right|_{\boldsymbol{\psi}=\boldsymbol{\psi}^{(p)}}} & \forall k = 1, \dots, N \\ \psi_{N+1}^{(p+1)} = \psi_N^{(p+1)} \end{cases} \quad , \quad (1.82)$$

with

$$\frac{\partial L_k(\boldsymbol{\psi})}{\partial \psi_k} = -\frac{2}{h^2} - 4\pi\lambda_B \sum_{\alpha=1}^{n_I} z_\alpha^2 c_{s,\alpha} \exp(-z_\alpha \psi_k). \quad (1.83)$$

See Ref [68], Eq. 19.6.43. This is repeated until the condition

$$\sum_{k=1}^N L_k(\boldsymbol{\psi})^2 <= N\delta^2 \quad (1.84)$$

is met, where δ is a given tolerance. The step in Eq. 1.82 can be improved by replacing $\psi_{k-1}^{(p)}$ by $\psi_{k-1}^{(p+1)}$, as far as the latter is already calculated for the previous index $k - 1$. The term $L_k(\boldsymbol{\psi}^{(p)})$ in Eq 1.82 becomes

$$L_k(\boldsymbol{\psi}^{(p)}) = \frac{\psi_{k+1}^{(p)} + \psi_{k-1}^{(p+1)} - 2\psi_k^{(p)}}{h^2} + \frac{\psi_{k+1}^{(p)} - \psi_{k-1}^{(p+1)}}{hr_k} + 4\pi\lambda_B \left[\sum_{\alpha=1}^{n_I} z_\alpha c_{s,\alpha} \exp(-z_\alpha \psi_k^{(p)}) + \xi(r_k) \right]. \quad (1.85)$$

The number of steps needed to reach convergence are significantly lower for this scheme than for the previous one (Eq. 1.85). However, the previous algorithm is in theory more amenable to a vectorized or parallelized implementation.

1.6 Structure Analysis

The purpose of this section is to highlight some of the simulation techniques used to analyse the structure of the simulated colloidal dispersions. They were mostly employed in Chapter 4.

1.6.1 Radial distribution function

The two-point density function $\rho_{ab}(\vec{r}, \vec{r}')$ is the number per unit of volumes square of particles pairs of types a and b at positions \vec{r} and \vec{r}' . It reads

$$\rho_{ab}(\vec{r}, \vec{r}') = \left\langle \sum_{\substack{i \in A \\ l \in B \\ j \neq i}} \delta(\vec{r} - \vec{r}_i) \delta(\vec{r}' - \vec{r}_j) \right\rangle, \quad (1.86)$$

where A and B are the sets of particles of respectively types a and b , and δ is the Dirac distribution. When the system is homogeneous and isotropic this function only depends on the separation $r = \|\vec{r} - \vec{r}'\|$. When the particles do not interact, or are decorrelated (typically when $r \rightarrow \infty$), we have

$$\rho_{ab} = \rho_a(\rho_b - \delta_{ab}/V), \quad (1.87)$$

where ρ_a (resp. ρ_b) is the volume density of particles of type a (resp. b), V is the volume and $\delta_{ab} = 1$ if $a = b$, 0 otherwise. The radial distribution function is defined by

$$g_{ab}(r) = \frac{\rho_{ab}(r)}{\rho_a(\rho_b - \delta_{ab}/V)}. \quad (1.88)$$

It is computed numerically by discretizing the function in interval of length Δr , as

$$g_{ab}(r) = \frac{2V}{N_a(N_b - \delta_{ab})} \left\langle \frac{n_{ab}(r)}{4\pi r^2 \Delta r} \right\rangle, \quad (1.89)$$

where $n_{ab}(r)$ is the number of particles pairs of respective type a and b separated by a distance between $r - \Delta r/2$ and $r + \Delta r/2$. Figure 1.11 shows a representation of this computation.

1.6.2 Structure factor

SAXS (Small Angles X-ray Scattering) consists in illuminating a sample with X-rays, and in measuring the corresponding scattered intensity as a function of the diffusion angle θ .

The latter is linked to scattered wave vector, of norm q , by the relation

$$q = \frac{4\pi}{\lambda} \sin \frac{\theta}{2} \quad (1.90)$$

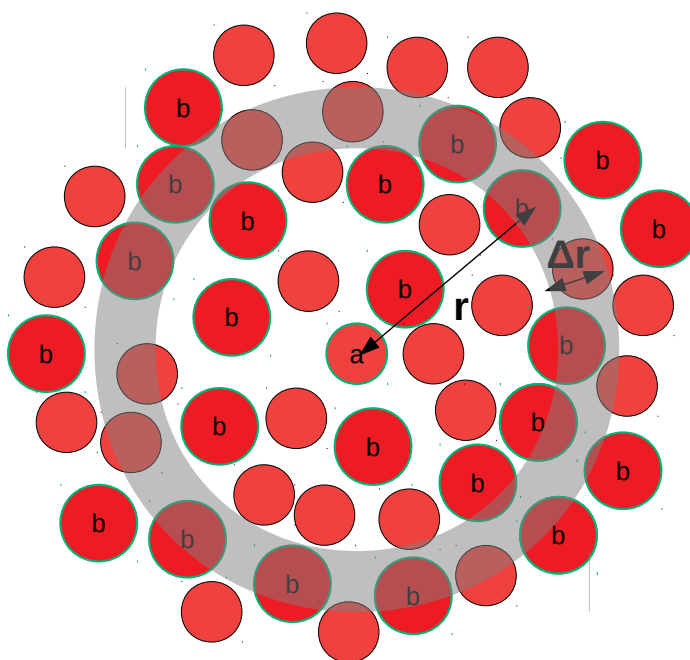


Figure 1.11: Representation of the calculation of the radial distribution function. Particles of type b between the sphere of radii $r - \Delta r/2$ and $r + \Delta r/2$ are counted.

For a monodisperse colloidal dispersion, the scattered intensity $I(q)$ (subtracted of the background intensity of the solvent) is directly proportional to the structure factor $S(q)$,

$$I(q) \propto |\mathcal{F}(q)|^2 S(q), \quad (1.91)$$

where $P(q) = |\mathcal{F}(q)|^2$ is the form factor of the particles. For spherical particles of radius R , \mathcal{F} can be expressed as

$$\mathcal{F}(q) = 3 \frac{\sin(qR) - qR \cos(qR)}{(qR)^3}. \quad (1.92)$$

$S(q)$, on the other hand, represents the mean spatial organization of the particles in the dispersion. It is nothing else than a function in the reciprocal space of the pair radial distribution function $g(r)$,

$$S(q) = 1 + \rho \int 4\pi r^2 \frac{\sin qr}{qr} [g(r) - 1] dr. \quad (1.93)$$

Typically, when $q = 2\pi/4R$, the oscillations of $g(r)$ are in line with those of $\sin(qr)$. It yields a peak in the $S(q)$, generally the main peak. The intensity of this peak is a measure of the local order between particles, its width is inversely related to the range of correlations. In the limit of an ideal dispersion, typically at infinite dilution where the particles does not interact, $S(q) = 1$ and the intensity is only a function of the form factor,

$$I^{id}(q) \propto \mathcal{F}(q)^2. \quad (1.94)$$

From a practical point of view, if the latter is known, the structure factor of a dispersion at finite concentration is obtained by

$$S(q) = \frac{I(q)}{I^{id}(q)}. \quad (1.95)$$

For a polydisperse colloidal dispersion, from Eq.(1.95)) we only get an *effective* structure factor. One can show that it is equal to

$$S_{eff}(q) = \frac{\sum_{a,b} \mathcal{F}_a(q) \mathcal{F}_b^*(q) v_a v_b \sqrt{\rho_a \rho_b} S_{ab}}{\sum_a \mathcal{F}_a(q) \mathcal{F}_a^*(q) v_a^2 \rho_a}, \quad (1.96)$$

where a (resp. b) indexes the family of particles of radius R_a (resp. R_b), v_a is the volume and ρ_a the volume density of the family a . $\mathcal{F}_a^*(q)$ is the complex conjugate of $\mathcal{F}_a(q)$, equal to $\mathcal{F}(q)$ (see Eq. 1.92) with $R = R_a$. The S_{ab} are related to the radial distribution function g_{ab} by

$$S_{ab}(q) = \delta_{ab} + \sqrt{\rho_a \rho_b} \int 4\pi r^2 \frac{\sin(qr)}{qr} [g_{ab}(r) - 1] dr, \quad (1.97)$$

with $\delta_{ab} = 1$ if $a = b$, otherwise $\delta_{ab} = 0$. In our simulations, the effective structure factors are calculated from the radial distribution functions with Equations 1.96 and 1.97.

1.6.3 Local Bond-Order Parameters

In crystals, first neighbors are arranged in a manner specific to the structure, local bond-order parameter are functions that depends on the relative orientations between a particle and its neighbors and are able sort out particles according to the phase they belong to. For a given natural number l , the complex local bond-order parameters $q_{lm}(i)$, with m an integer in the range $[-l, +l]$, the rotationally invariant local bond-order parameter $q_l(i)$, and the correlation function of the local bond-order parameters $c_l(i)$ are defined by [69, 70]

$$q_{lm}(i) = \frac{1}{N_b(i)} \sum_{j=1}^{N_b(i)} Y_{lm}(u_{ij}) \quad (1.98)$$

$$q_l(i) = \sqrt{\frac{4\pi}{2l+1} \sum_{m=-l}^l q_{lm}(i) q_{lm}^*(i)} \quad (1.99)$$

$$c_l(i, j) = \sum_{m=-l}^l q_{lm}(i) q_{lm}^*(j), \quad (1.100)$$

where i (resp j) denotes the number of the particle i (resp j), $N_b(i)$ is the number of neighbors around the particle i . The radius to find neighbors can be found by a rule of thumb that sets it at $1.5\sqrt[3]{V/N}$, with N the total number of particles, or by using the first minimum of the radial distribution function after the first peak. One should note that in practice for a body-centered cubic lattice it includes the first and second neighbors.

We also used the neighbor-averaged order parameters,

$$\bar{q}_{lm}(i) = \frac{1}{N_b(i) + 1} \left[\sum_{j=1}^{N_b(i)} q_{lm}(j) \right] \quad (1.101)$$

$$\bar{q}_l(i) = \sqrt{\frac{4\pi}{2l+1} \sum_{m=-l}^l \bar{q}_{lm}(i) \bar{q}_{lm}^*(i)} \quad (1.102)$$

$$(1.103)$$

more specifically \bar{q}_6 and \bar{q}_4 .

Figures 1.12(a) and 1.12(b) the (q_6, q_4) (resp. (\bar{q}_6, \bar{q}_4)) maps obtained for CS particles in various crystal phases and in a fluid phase. These maps are used to define the range of q_6 and q_4 (resp. \bar{q}_6 and \bar{q}_4) values for which a particle can be considered to belong to a given phase. Only the neighbor-averaged version of the order parameters allowed a clear distinction of the phases. It was thus used in this work.

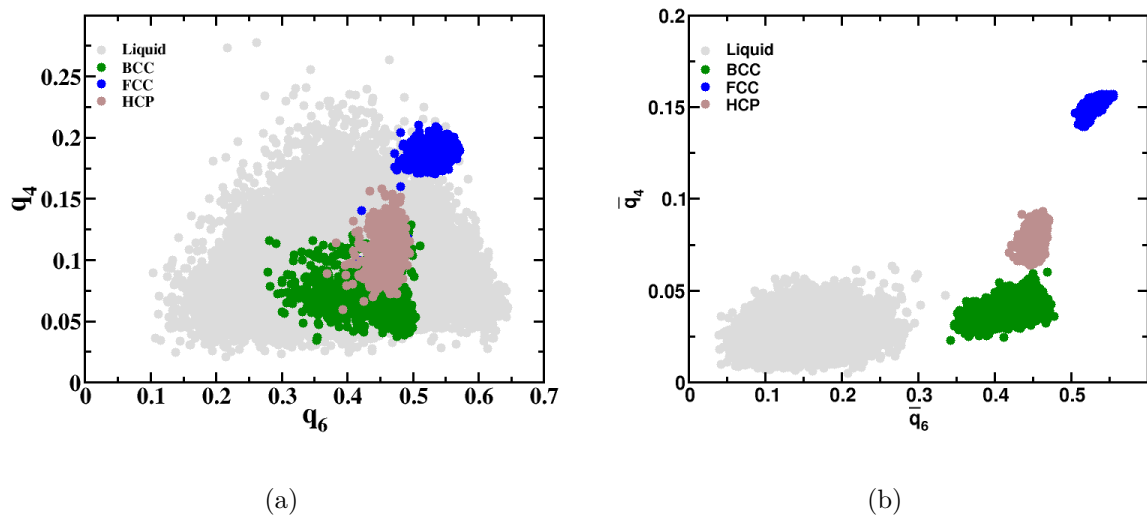


Figure 1.12: Bond order parameter maps of CS particles in various crystalline phases and in the liquid phase. (a) q_6q_4 map (b) $\bar{q}_6\bar{q}_4$ map.

Chapter 2

Effective pair potential between charged nanoparticles at high volume fractions

Simulations of charged colloidal dispersions are technically challenging. One possible workaround consists in reducing the system to the colloids only, whose interactions are described through an effective pair potential, w^* . Still, the determination of w^* is difficult mainly because it depends on the colloidal density, ϕ . Here we propose to calculate w^* from simulations of a pair of colloids placed in a cubic box with periodic boundary conditions. The variation in ϕ is mimicked by an appropriate change in the concentration of counterions neutralized by an homogeneous background charge. The method is tested at the level of the primitive model. A good description of the structure of the colloidal dispersion is obtained in the low and high coupling regimes, even at high ϕ ($\approx 30\%$). Furthermore, the method can easily be used in popular molecular simulation program packages and extended to non-spherical objects.

2.1 Introduction

Colloidal interactions play a key role in the understanding and control of structural and mechanical properties of colloidal materials[71, 72], as well as in the control of the stability, kinetics of aggregation and phase behavior of colloidal dispersions[73, 74]. They are of fundamental importance for numerous systems ranging from inorganic nanomaterials

(e.g. cement, mesocrystals) to polymers and proteins. Accurate descriptions of colloidal interactions can be used to quantitatively compute these properties or to design advanced materials *in silico*. Model hard core systems are a good example and have motivated a large number of theoretical and experimental works. In particular, computer simulations of these model systems were shown to quantify with good precision and to rationalize most of their properties. These include the glass transition, the phase diagram and the rate of crystal nucleation of hard spheres[75, 76, 18, 77] or the phase transition of hard discoids.[78, 79, 80]

Charged colloidal systems in the thermodynamic limit of infinite dilution, i.e., when interparticle distances well exceed the range of interactions, is another good example, although much more complicated. In this limiting case the Derjaguin-Landau-Verwey-Overbeek (DLVO) theory[5, 6], the cornerstone of colloidal science, describes accurately pair colloidal interactions, provided that the electrostatic coupling is not high and the interparticle distance not too small. The theory has successfully been applied to many systems, see, e.g., the recent work of Sinha *et al.*[74] At higher electrostatic coupling, ion-ion correlations need to be accounted for and this is well captured by modern computer simulations and theory[81, 82, 83].

When it comes to the concentrated regime, however, the picture is far less clear[84]. From the experimental point of view this is explained by the difficulty to characterize the interactions in concentrated colloidal dispersions. This is well exemplified by a series of experimental papers linked to controversial conclusions,[85, 86] suggesting long range attraction between like-charged colloids in salt free conditions, in contradiction with the expected DLVO like repulsion. It has since been shown that such «anomalous» long range attraction, measured by video microscopy, was the result of disregarding known limitations of optical microscopes[87, 88]. From the perspective of theories and simulations, the main reasons lie in the importance of many-body interactions, as well as in the large asymmetry in size, mass and time scale between the colloidal particles and solvent/solute molecules.

Several theoretical and simulation approaches have been proposed to tackle this challenging problem [89, 90, 65, 66, 62, 91, 60, 92, 93], among which one of the most promising ideas, first introduced by Beresford-Smith[90] and by Alexander[65], consists in reducing the colloidal system to a one component model (OCM), where the colloids and only the colloids interact through an effective pair potential $w^*(r)$. In other words, this amounts

to implicitly account for the many-body interactions through an effective pair potential. The consequence is a density dependence of $w^*(r)$ [89] which, thus, needs to be determined for each colloidal density of interest.

In the seminal work of Alexander[65], it was shown that accurate $w^*(r)$ at particle volume fraction ϕ can be calculated using a Wigner-Seitz cell model, of radius R_c , in which a single spherical colloid is placed, of radius R , such that $\phi = (R/R_c)^3$. The model can be solved using the Poisson-Boltzmann equation or Monte Carlo simulations. Also, a one colloid renormalized jellium model was introduced by Trizac *et al.*[66], thought to be more appropriate in the dilute regime. However, all these methods are restricted to low electrostatic couplings (where ion-ion correlations are negligible) and to spherical colloids. Furthermore, they are not appropriate to deal with the short range interactions at the molecular level.

In order to avoid these restrictions, it was more recently proposed to use two colloids, instead of one, in a closed cylindrical cell or in a cubic box with periodic conditions[60, 62], and to determine $w^*(r)$ from sampling the pair potential of mean force supplemented with a Yukawa force at long range. The method was tested by comparing the radial distribution functions of the colloids, $g_c(r)$, obtained from the OCM simulations using the precalculated $w^*(r)$ and from full primitive model (FPM) simulations of many-colloid systems with explicit monovalent and divalent counterions. The method was shown to give accurate density-dependent $w^*(r)$ for isotropic and anisotropic colloids even when ion-ion correlations are important[60, 61]. It was further successfully used at the molecular level[94]. However, due to boundary artifacts, colloid images or hard cell walls, the range of ϕ is limited to the dilute or semi-dilute regime.

In this chapter, we develop the idea that these artifacts can be eliminated by the combined use of an excess counterion concentration, to mimic a finite colloid density, in a large enough simulation cell, and of a uniform charged background, to neutralize the overall system. It presents some analogies with the jellium approximation[66], but, as it will be shown, is well appropriate for concentrated as well as for highly coupled systems. We explain how this idea can be implemented in a Monte Carlo (MC) or Molecular Dynamics (MD) simulation and give a simple recipe on how to relate the excess counterion concentration (background charge density) with that of the colloids. We further show, by comparing the $g_c(r)$ obtained from the OCM and FPM simulations, that this approach

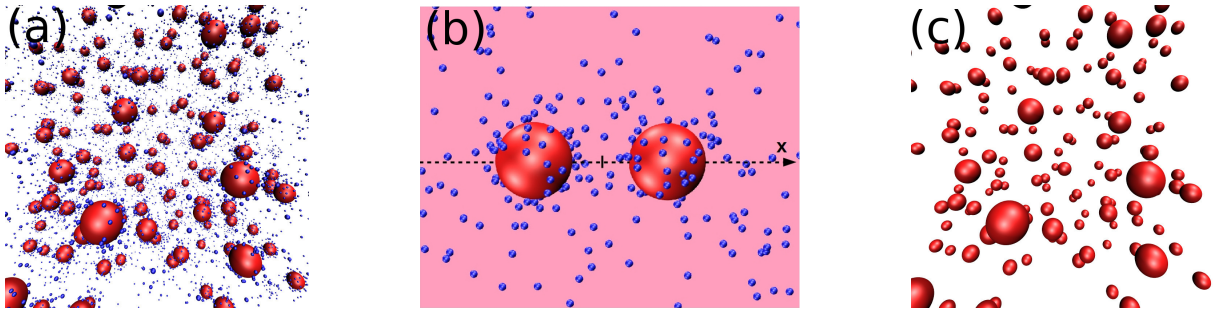


Figure 2.1: From the FPM simulations of a colloidal dispersion described at the level of the primitive model (a), two colloids are "extracted" and placed in a bath composed of counterions and of a homogeneous background charge (b), average forces between the colloids are then calculated to produce the PMF used in the OCM simulations (c).

gives good results at low and high electrostatic coupling, with virtually no limitations in ϕ .

2.2 Model and Simulations

For the sake of simplicity we chose the same model and reference systems as in [60], see also Fig. 2.1. In brief, we restricted ourselves to the primitive model, where all the colloids and micro-ions are treated explicitly but where the solvent is described as a dielectric continuum with $\epsilon_r = 78.4$. The reference systems are salt free colloidal dispersions at various ϕ composed of monodisperse spherical particles of diameter $\sigma_C = 40\text{\AA}$ bearing a charge $Q_c = -60e$ compensated either with monovalent, $Q_I = 1e$ or divalent, $Q_I = 2e$, counterions of diameter $\sigma_I = 4\text{\AA}$. For efficiency reasons, the usual hard core interaction of the primitive model was here replaced by a truncated and shifted Lennard-Jones potential,

$$w_{ij}^{SLJ}(r) = \begin{cases} \epsilon_{ij} \left\{ 4 \left[\left(\frac{\sigma_{ij}^*}{r} \right)^{12} - \left(\frac{\sigma_{ij}^*}{r} \right)^6 \right] + 1 \right\} & \text{if } r \leq \sigma_{ij} \\ 0 & \text{if } r > \sigma_{ij} \end{cases} \quad (2.1)$$

where $\sigma_{ij}^* = \frac{1}{2^{1/6}} \sigma_{ij}$, $\sigma_{ij} = \frac{1}{2}(\sigma_i + \sigma_j)$ and $\epsilon_{ij} = 100k_B T$. ϕ was varied from 0.84% to 26.8%, see Table 2.1, and the temperature was maintained constant at $T = 298$ K. The FPM systems were simulated with MD (GROMACS version 4.5.4[95]). On the other hand, the OCM simulations and calculations of $w^*(r)$ were performed with an in-house MC software in the NVT ensemble.

$w^*(r)$ between two colloids was calculated in a cubic box with periodic boundary

ϕ	L (nm)	ρ_{back} ($10^5 e \cdot \text{nm}^{-3}$)	Q_c^*	λ_D^* (nm)
0.84%	40 [40]	0.3031 [0.1250]	18.66 [6.129]	4.759 [5.839]
1.7%	40 [40]	0.5563 [0.2188]	18.60 [5.493]	3.647 [4.669]
3.3%	40 [40]	1.000 [0.3875]	19.46 [5.121]	2.647 [3.150]
6.7%	40 [40]	1.956 [0.6813]	19.30 [3.036]	2.052 [4.248]
13.4%	33 [40]	4.050 [1.263]	16.26 [-]	1.784 [-]
26.8%	33 [40]	10.20 [2.5312]	31.25 [-]	0.7809 [-]

Table 2.1: Parameters of the background charge simulations^a

^aThe columns give in the case of monovalent (unbracketed values) and of divalent (bracketed [values]) counterions (1) the colloidal volume fraction, (2) the box length, (3) the background charge density, (4) the fitted Yukawa effective colloidal charge and (5) the fitted Yukawa effective Debye length, see text for more details.

conditions, filled with an excess of counterions and a neutralizing background charge, c.f. Fig. 2.1. The length of the box, L , was chosen large enough such that the interactions of the colloids with their images are negligible. The Ewald summation is the most common way to introduce a background charge. For non-neutral systems, the Ewald algorithm implicitly introduces a uniform background charge distribution that effectively neutralizes the simulation box [96, 97]. Alternatively, an analytical expression for the field associated with the background charge can be obtained for a closed spherical cell (Wigner-Seitz cell model) and for a cubic box with the minimum image approximation [98]. Here, for efficiency and simplicity reasons, we made use of the Fennell Hamiltonian [57], which corrects for long-range electrostatic interactions and implicitly introduces a homogeneous background charge,

$$\beta H_{coul} = \sum_{\substack{i \neq j \\ r_{ij} < r_{cut}}} \lambda_B q_i q_j \left(\frac{1}{r_{ij}} + \frac{r_{ij}}{r_{cut}} - \frac{2}{r_{cut}} \right) \quad (2.2)$$

where r_{ij} the distance between the charged species i and j , $\beta = \frac{1}{k_B T}$ with k_B the Boltzmann constant, $q_i = Q_i/e$ and λ_B is the Bjerrum length. r_{cut} is a cutoff radius above which the interactions are not calculated. r_{cut} was set to half the box length, as prescribed by Fennell.

At this point, a closure relation which relates the excess counter-ion density (background charge density) to the colloid density (ϕ) is missing. A naive solution consists

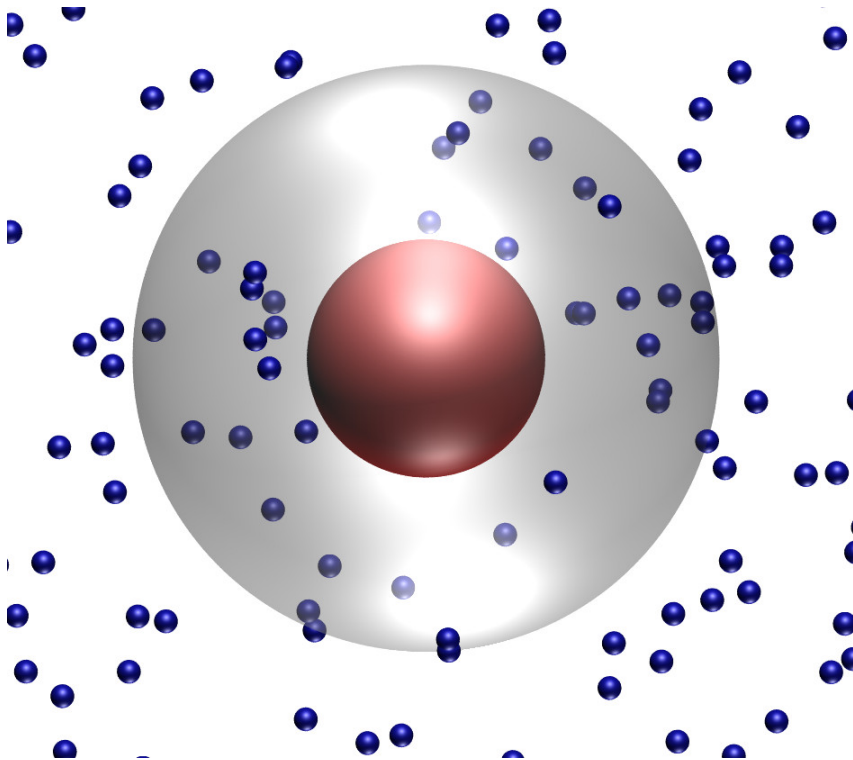


Figure 2.2: Representation of a simulation intended to determine the background charge at a given ϕ . The transparent sphere represents a virtual volume, V_a whose size is adjusted to the desired particle volume fraction, ϕ . The value of background charge density is obtained when V_a is on average charge neutral.

in equating the background charge density to the mean charge density of the colloids. However, this would only work at low electrostatic coupling[99, 66] as a result of ion condensation. An alternative is to use the closure proposed by Trizac *et al.* for the renormalized jellium model[66], which is conceptually similar to the present approach. Although appealing, the obtained results (not shown) were not optimal. Instead, we use a simple numerical recipe based on an NVT MC simulation of a single colloid in a cubic box with periodic boundary conditions. The recipe, see Fig.2.2, consists in finding for an adequate volume, V_a , around the colloidal particle, the background charge density for which the average total charge brought by the small ions exactly compensates that of the colloid,

$$\left\langle \sum_{\substack{i \\ r_I \in V_a}}^{N_I} Q_i \right\rangle = Q_c. \quad (2.3)$$

V_a is chosen such as to match the desired particle volume fraction and its geometry to fit that of the colloidal particle, here a sphere. Furthermore, the volume of the one-colloid simulation box was taken as half of the two-colloid simulations, since the calculated value for the background charge density, ρ_{back} , depends on the actual colloid density. We used $L = 31.748$ nm for one-colloid simulations and $L = 40$ nm for two-colloid simulations for most of the cases studied. The used L values and calculated ρ_{back} are listed in Table 2.1. As expected, the background charge density increases with ϕ and is weaker in presence of divalent counterions because of an enhanced screening effect.

The mean force between the colloids was calculated across the midplane ($x=0$) for fixed colloid separation r along the x -axis, see Fig.2.1. The total mean force reads,

$$F(r, \phi) = F^{el}(r, \phi) + F^{LJ}(r, \phi) + F^{id}(r, \phi) + F_{back}^{el}(r, \phi). \quad (2.4)$$

The electrostatic term, F^{el} , and Lennard Jones term, F^{LJ} , are calculated by summing up all Coulomb and LJ forces over the midplane. The third term is the ideal contribution, which has a simple relation of the ion densities, ρ_I , at the midplane and at the box edges, $F^{id}(r, \phi) = k_B T [\rho_I(x=0) - \rho_I(x=\pm L/2)] L^2$. The last term accounts for the electrostatic interactions of the background charge with the charged species and with itself. The latter was numerically solved, see §1.4.4 for more details. Following the previous work of Thuresson *et al.*[60], the so obtained calculated forces were then extrapolated to infinity by fitting a Yukawa force, $\beta F_Y(r) = \lambda_B \left(\frac{Q_c^*}{1+\sigma_C/2\lambda_D^*} \right)^2 \exp\left(\frac{-r}{\lambda_D^*}\right) / r (1/r + 1/\lambda_d^*)$, where Q_c^* and λ_D^* are the effective colloid charge and Debye length, respectively. The fitted values

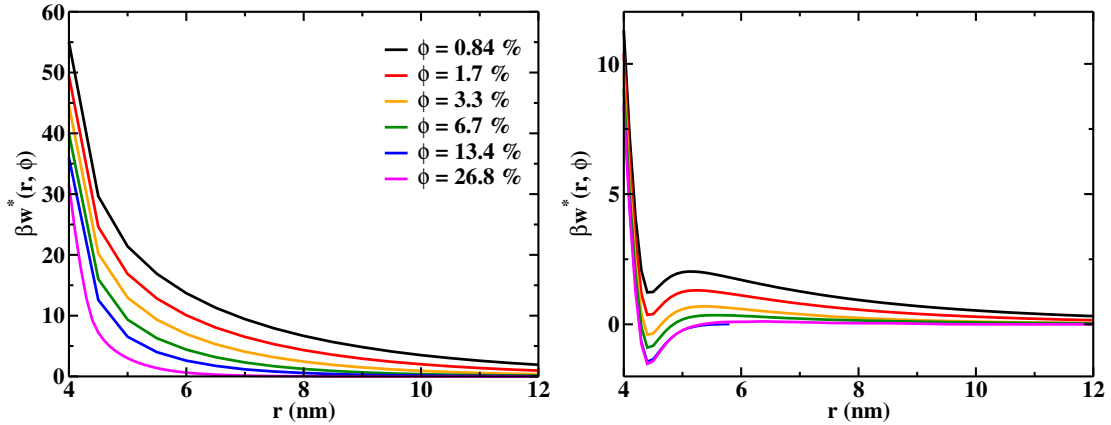


Figure 2.3: Pair potential of mean force between colloids at various volume fractions from background charge simulations, with monovalent (left) and divalent (left) counterions.

for those two parameters are also listed in Table 2.1. The pair potential of mean force, $w^*(r, \phi)$, is then calculated from the integration of $F(r, \phi)$, $w^*(r, \phi) = -\int_{\infty}^r F(r', \phi) dr'$.

2.3 Results

Fig. 2.3 shows the calculated $w^*(r, \phi)$ at various ϕ in presence either of monovalent or divalent ions. In agreement with our previous work[60], a purely repulsive $w^*(r, \phi)$ is found in the case of monovalent counterions while an attracto-repulsive potential is seen in the case of divalent counterions. The attraction, of purely electrostatic origin, is the consequence of the ion-ion correlations, see e.g.[81, 82, 83]. In both cases, $w^*(r, \phi)$ is found to decrease as ϕ is increased. That is, a reduced repulsion, in presence of monovalent ions and a drop in the repulsion barrier, in presence of divalent ions, concomitantly with a drop in λ_D^* , see Table 2.1. This is best explained by a larger ion concentration ($\#\rho_{back}$) which, in turn, leads to greater charge screening. Similarly, the correlation attraction is also found to strengthen with ϕ ($\#\rho_{back}$).

In Fig. 2.4 we compare $g_c(r)$ obtained from MD simulations of colloidal dispersions described at the level of the primitive model with predictions from OCM simulations, performed with MC, in the case of both mono and divalent counterions. For the OCM simulations, we use the effective pair potentials calculated above (Fig. 2.3). The general trend is very well reproduced for the entire range of ϕ studied. In particular, the liquid like oscillations in presence of monovalent counterions and the aggregate formation in the case of divalent counterions, characterized by a growing peak at $r \approx \sigma_C + \sigma_I$ and

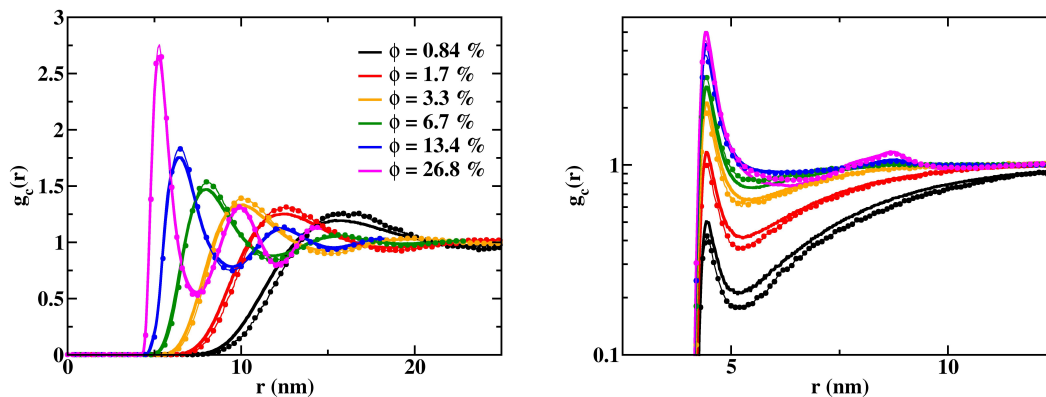


Figure 2.4: Comparison of the radial distribution functions of the colloids obtained in OCM simulations (thick lines) with those obtained in FPM simulations (lines with circles) in presence of monovalent (left) and divalent counterions (right).

the simultaneous appearance of a shoulder at $r \approx 2\sigma_C$ with increasing ϕ , are very well described. The quantitative agreement between the FPM and the OCM is good and tends to become better with increasing ϕ . The OCM with the calculated $w^*(r, \phi)$ tends to underestimate the height of the first peak, in the case of monovalent counterions. As we will show below, this small discrepancy can be explained by an overestimated background charge density, which in turn leads to a slightly too strong screening of the calculated electrostatic repulsions. Although less clear in the divalent counterion case, the observed difference in $g_c(r)$ obtained from the FPM and OCM simulations has the same origin. This is confirmed when one compares the effective pair potential obtained from the proposed method and from interactive Boltzmann inverse calculations[63, 64] of the FPM simulations, see §1.4.4.

In any case, to our knowledge, our method provides the best results, in a large range of ϕ , for both low and high electrostatic coupling. This is obvious at high electrostatic coupling, particularly in the concentrated regime. In the case of monovalent counterions, we also tested Alexander prescriptions further developed by Trizac *et al.* [100], which consist in extracting Q_c^* and λ_D^* from the cell model. We used MC simulations instead of the Poisson-Boltzmann equation, but the idea remains the same. The resulting $g_c(r)$ are plotted on Fig. 2.5. Although the agreement with FPM simulations is good at $\phi = 0.84\%$, it rapidly degrades when concentrating the dispersion, contrary to our approach. In general, for salt free systems, the effective pair potential obtained with Alexander prescriptions

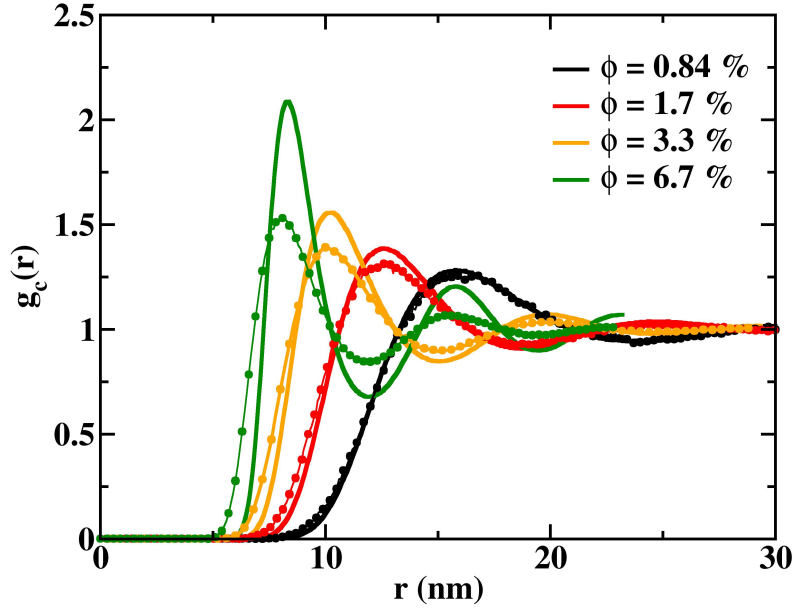


Figure 2.5: Comparison of the radial distribution functions of the colloids with monovalent counterions produced following Alexander's prescriptions (thick lines) and with the FPM (lines with circles).

largely overestimates the electrostatic repulsions.

Finally, we have seen that our simulation method, combined with the proposed numerical closure which relates ϕ to ρ_{back} , although more than satisfactory, does not give a perfect description of the colloidal dispersion structure. We can thus ask ourselves if this is the result of the developed approximation method to account for many body interactions, i.e., the use of ρ_{back} , or of the calculated ρ_{back} values. As an attempt to answer this question, we provide in Fig. 2.6 a comparison of $g_c(r)$ obtained with FPM simulations with that from OCM simulations, using ρ_{back} as a free parameter. The $g_c(r)$ are those of a salt free system at $\phi = 6.7\%$ with monovalent counterions. As can be seen, with $\rho_{back} = 1.219 \cdot 10^{-5} \text{ e.nm}^{-3}$ a perfect agreement is obtained, which gives a strong support to the second hypothesis and, consequently, to our simulation method to calculate $w^*(r, \phi)$.

2.4 Conclusion

To conclude, we developed a simulation method based on an homogeneous background charge density to estimate the density dependent effective pair potential between charged

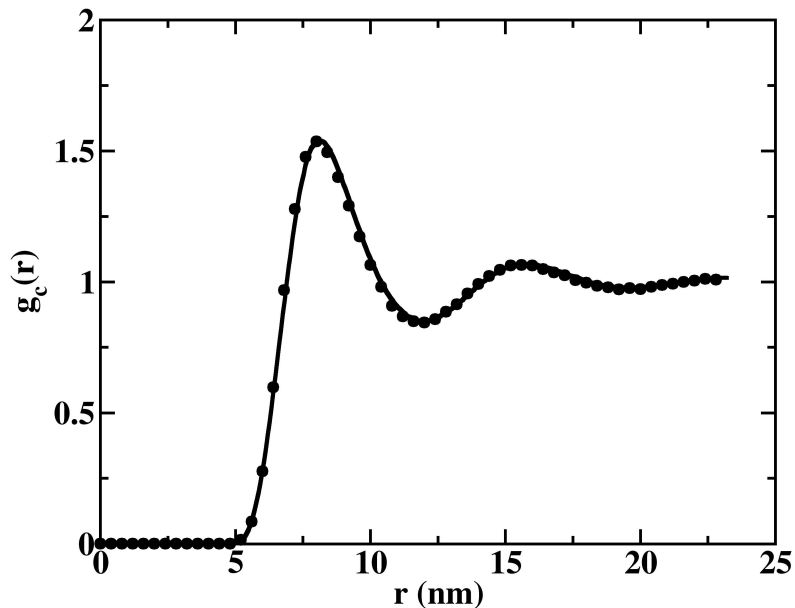


Figure 2.6: Radial distribution function of the colloids at 6.7% volume fraction as obtained from the FPM (circles) and the fitted background charge model (thick line).

colloids. Combined with a simple prescription to relate ρ_{back} to ϕ , it allows one to predict with a good accuracy the structure of colloidal dispersions in a large range of conditions at much lower cost than brute force simulations. The proposed method is shown to work in the diluted and concentrated regimes as well as at low and high electrostatic coupling. What is more, it can be easily used in popular MD packages (see §1.4.4 for an example) and is *a priori* applicable to molecular simulations as well as to any colloidal geometry and shape. Finally, we show that our prescription to relate ρ_{back} to ϕ can be improved, as preliminary simulation results strongly suggest that an optimum $w^*(r, \phi) = f(\rho_{back})$ exists. In any case, our approach should provide an easy route in assisting the efforts in the design of new nanomaterials.

Chapter 3

Jellium and Cell Model for Titratable Colloids with Continuous Size Distribution

A good understanding and determination of colloidal interactions is paramount to comprehend and model the thermodynamic and structural properties of colloidal suspensions. In concentrated aqueous suspensions of colloids with a titratable surface charge, this determination is, however, complicated by the density dependence of the effective pair potential due to both the many-body interactions and the charge regulation of the colloids. In addition, colloids generally present a size distribution which results in a virtually infinite combination of colloid pairs. In this chapter we develop two methods and describe the corresponding algorithms to solve this problem for arbitrary size distributions. An implementation in Nim is also provided. The methods, inspired by the seminal work of Torres *et al.*[101], are based on a generalization of the cell and renormalized jellium models to polydisperse suspensions of spherical colloids with a charge regulating boundary condition. The latter is described by the one-pK-Stern model. The predictions of the models are confronted to the equations of state of various commercially available silica dispersions. The renormalized Yukawa parameters (effective charges and screening lengths) are also calculated. The importance of size and charge polydispersity as well as the validity of these two models are discussed in light of the results.

3.1 Introduction

Size polydispersity, rather than being an exception, is a general rule in the realm of colloidal systems. It has been shown to influence the micro structure of suspensions [102], to considerably enrich the number of crystal phases observed [103, 104, 8, 33], to affect nucleation [105, 106, 50], to induce the fractionation of particles during crystallization [107, 77, 47, 108, 8] and to allow particular behavior such as colloidal Brazil nut effect [109, 110], colloidal stratification [111, 112] and fluid-fluid demixing [113, 114, 115]. Moreover, polydispersity has been shown to be an essential feature in the formation of colloidal glasses [18, 116] and has allowed substantial achievements in the understanding of this state, see e.g. Refs [53, 117, 118, 119].

Despite its ubiquity, polydispersity is still often neglected, with the exception of neutral hard sphere systems, and the variety of phases, states and behaviors that it brings about are imperfectly controlled and understood. The main reason for this is the fact that computer simulations still lag well behind experimental observations, when appropriate models exist at all. This is particularly true for charged colloidal suspensions, the system of interest in this PhD work.

From a simulation point of view, representative and realistic models of charged polydisperse colloidal suspensions are indeed tractable neither at the primitive model level of approximation, where the degrees of freedom of the solvent molecules are averaged out through a dielectric continuum, nor at the level of the mean field approximation [120, 121, 92], where the many ions are further replaced by a mean electrostatic potential obtained from solving the Poisson-Boltzmann equation. An amenable and attractive approach, first introduced by Beresford-Smith [122], consists, instead, in whittling the colloidal system down to the colloidal particles only, i.e. the one-component model, while the degrees of freedom of the ions and solvent molecules are integrated out in *effective* pair potentials between the colloids, $w^*(r)$. The reduction of the many-body interactions into effective potentials, however, makes w^* density dependent [123] and, thus, necessarily re-determined for each colloid density.

In the case of monodisperse spherical particles at low electrostatic coupling, Alexander *et al.* [65] showed that $w^*(r)$ retains a simple Yukawa form but with *effective* parameters, namely an effective charge, Z^* , and screening length, $1/\kappa^*$, instead of the bare charge, Z and bulk screening length, $1/\kappa$. The study further showed that Z^* and κ^* can be obtained

from solving the Poisson-Boltzmann equation around *one* colloid placed in Wigner-Seitz cell model (CM)[124]. In the same spirit, a one-colloid renormalized jellium model was developed and shown to be successful in salt free systems [66]. At high electrostatic coupling, *two*-colloids cell [60] and jellium models (see Chapter 2) solved in the full primitive model were shown to provide accurate $w^*(r)$ for arbitrary colloid shapes [61] and concentrations. The two-colloid approach was further used at a molecular level [94] in a 3D-periodic simulation box.

In the case of charged colloid mixtures, Torres *et al.* [101] proposed a generalization of the cell model. The great insight of Torres and co-workers was simply to impose the same potential at the boundary of each cell, each family of colloidal particles being represented by one colloidal particle centered in its own Wigner-Seitz cell, in such a way as to ensure the continuity of electric potential and ion concentrations across the cell boundaries. The greatest ideas also being the simplest, it was then followed to generalize the jellium model [125, 126]. However, to our knowledge the generalized cell and jellium models have only been tested in the salt free case [126]. Furthermore, they have so far always been restricted to binary mixtures, i.e. have never been applied to polydisperse charged colloidal suspensions with continuous size distribution.

Another difficulty arises from the nature of the surface charge and its dependence on the density and size polydispersity of colloidal suspensions, namely the *charge regulation* and the *charge polydispersity*. Both largely depend on the chemistry of the colloid surface and of the electrolyte but also on the surface curvature and strength of the interactions and are, thus, specific to each colloidal system. The aqueous surface chemistry and charging behavior of colloidal particles has been the subject of many investigations essentially concerning the thermodynamic limit of infinite (colloid) dilution, see e.g. Refs. [127, 128, 129, 130]. On the contrary, in studies of the structure of colloidal suspensions, the charging behavior (of colloids) is most often simply ignored, the assumption being either a constant surface charge density[131] or at best a constant electrical double layer potential [132]. This can be explained in part by the complexity of characterization and, thus, by the poor knowledge of the charging behavior of colloids in *non diluted* suspensions, not to mention the charge polydispersity, as indicated by the very limited research work available [133, 134, 135]. Very rarely have attempts been made to include a description of surface chemistry [136, 137, 138]. Furthermore, those that do exist are, again, all limited

to monodisperse systems.

Motivated by the recent experimental results obtained by Cabane *et al.*[8] on aqueous suspensions of titrating silica nanoparticles with large polydispersity, which show a fractionation of particles in three coexisting phases (Laves/BCC/liquid phases) in the semi-concentrated regime and high pH, we here develop two methods and describe the corresponding algorithms to estimate the charging behavior and charge polydispersity of titrating silica particles with a continuous size distribution. The methods are further used to evaluate the sets of effective parameters (i.e. Z^* and κ^*) to be used in a one-component model. The methods, largely inspired by the seminal work of Torres *et al.*[101], are based on a generalization of the cell and renormalized jellium models to polydisperse suspensions of spherical colloids supplemented with a charge regulating boundary condition described by a 1-pK-Stern model. Certain features are studied, in particular, the dependence of the charge polydispersity as well as its scaling with the surface curvature on the size polydispersity and density of the colloids. Finally, the validity of the proposed models is discussed in terms of their ability to describe the equation of state of various commercially available silica dispersions.

The chapter is organized as follows: in Sect. 3.2 we introduce the models used, that is, in Sect. 3.2.1 and 3.2.2, the generalized cell model and jellium model for charged polydisperse colloidal suspensions and, in Sect. 3.2.3, the 1-pK Stern model to describe the interface between the solid and the electrolyte solution in the presence of acidic surface groups. In Sect. 3.2.4 the algorithm used to solve the cell and jellium models coupled with the 1-pK Stern model is described. In Sect. 3.3.1 we present the 1-pK-Stern model fit of the charging behavior of silica surfaces in the dilute regime together with the CM and RJM predictions of the bare charge polydispersity of silica nanoparticles with various polydispersities and densities, and in various pH conditions. The corresponding effective charge polydispersities and effective screening lengths are presented in Sect. 3.3.2. Microion pressures for various polydispersities and distribution shapes is studied in Sect 3.3.3. Finally, experimental data are compared with the predictions of the cell and jellium model in the same section, followed by conclusions in Sect. 3.4.

3.2 Models

Let us consider a polydisperse colloidal suspension composed of n_p spherical colloidal species of radii R_p bearing a charge $Q_p = Z_p e$ with e the elementary charge and $p = 1, \dots, n_p$. They are immersed in a volume V filled with an aqueous salt solution of dielectric constant ϵ in equilibrium with a reservoir at a temperature T and of inverse screening length,

$$\kappa = \sqrt{4\pi\lambda_B \sum_{i=1}^{n_i} z_i^2 c_{s,i}}, \quad (3.1)$$

where $\lambda_B = \frac{e^2}{4\pi k_B T \epsilon}$ is the Bjerrum length and k_B is the Boltzmann constant while z_i and $c_{s,i}$ are the number valence and bulk concentration of ionic species i , respectively. n_i is the total number of ion species. The composition of each colloidal species is defined by its number fraction $x_p = N_p / \sum_{n_p} N_p$.

Within the mean-field approximation of the primitive model, the electrostatic potential at the surface of the colloids, at a set configuration of the latter, and in the electrolyte solution is determined by solving the Poisson-Boltzmann equation, which for an arbitrary system is given by [67]

$$\epsilon \Delta V(\vec{r}) + \sum_{i=1}^{n_i} z_i e c_i(\vec{r}) + \rho_e(\vec{r}) = 0, \quad (3.2)$$

where \vec{r} is the vector position in the solution, V is the electrostatic potential, Δ is the Laplace operator, $c_i(\vec{r}) = c_{s,i} \exp\left(\frac{-z_i e V(\vec{r})}{k_B T}\right)$ and ρ_e is a charge density associated with the colloids, specified later according to the model.

Within the approximation of the polydisperse cell model (PCM) and polydisperse renormalized jellium model (PRJM) it is only necessary to solve Equation 3.2 with one colloid with the appropriate boundary conditions and to repeat it for each colloid species. Taking further advantage of the spherical symmetry, the electrostatic potential becomes a mere function of the radial coordinate r and Eq. 3.2 reduces to

$$\frac{\partial^2 \psi}{\partial r^2} + \frac{2}{r} \frac{\partial \psi}{\partial r} + 4\pi\lambda_B \left[\sum_{i=1}^{n_i} z_i c_{s,i} \exp(-z_i \psi(r)) + \xi(r) \right] = 0, \quad (3.3)$$

where for convenience, we have introduced the dimensionless potential $\psi = \frac{eV}{k_B T}$ and the reduced charge density $\xi = \rho_e / e$. The surrounding colloids are effectively accounted for through the boundary conditions and ξ which depends on the model used. They are detailed below.

3.2.1 Cell model

The cell model approximation was initially designed for colloidal crystals and emerged from the realization that due to its periodicity the volume of a crystal can be divided into electroneutral Wigner-Seitz cells surrounding each colloid, which on average have the same volume and contain the same ion concentrations[65]. In other words, the thermodynamic properties of the system can be reduced to one colloid enclosed in an appropriate cell. The geometry of the cell is further assumed to have the same shape as the colloid. A spherical cell of radius R_c centered on the colloid is a natural choice for a spherical colloid. Note that the cell model approximation was also shown to be valid for non spherical colloids and moderately concentrated fluid states[139, 140, 141].

Within this approximation, $\xi = 0$ and, thus, the PB equation, Eq. 3.3, within the electrolyte solution takes the usual form

$$\Delta \psi(r) = \kappa^2 \sinh \psi(r) \text{ with } R_p < r < R_c. \quad (3.4)$$

Note that here a 1-1 salt solution is considered. The Gauss law imposes that the electric field be null everywhere on the boundary of the electroneutral cell,

$$\left. \frac{\partial \psi}{\partial r} \right|_{r=R_c} = 0. \quad (3.5)$$

The missing boundary condition at the colloid surface is described below (Sect. 3.2.3).

For monodisperse dispersions the cell radius is commensurate with the particle volume fraction ϕ ,

$$\phi = \left(\frac{R}{R_c} \right)^3. \quad (3.6)$$

Similarly, for polydisperse dispersions, the cell radii of the colloidal species, $R_{c,p}$, are related to the overall particle volume fraction by

$$\phi = \frac{\sum_{p=1}^{n_p} x_p R_p^3}{\sum_{p=1}^{n_p} x_p R_{c,p}^3}. \quad (3.7)$$

These unknown variables are determined by imposing the continuity of the electrical potential and ion concentrations over the different cells[101]. That is to say,

$$\psi(R_{c,1}) = \psi(R_{c,2}) = \dots = \psi(R_{c,n_p}) = \psi_c. \quad (3.8)$$

In the case of suspensions of colloids immersed in monovalent salt solutions, the effective pair potential between the colloids keeps the form of a screened Coulomb potential,

$$\beta u(r_{pq}) = \lambda_B v_p Z_p^* v_q Z_q^* \frac{\exp(-\kappa^* r)}{r}, \quad (3.9)$$

but with the renormalized charges and inverse screening length as leading parameters. In the previous equation $v_p = \exp(\kappa^* R_p)/(1 + \kappa^* R_p)$ ensures that the ionic cloud is excluded from the core of the colloid. Following the elegant method of Trizac *et al.*[100] those renormalized parameters can be obtained analytically from the calculated electrostatic potential at the edge of the cell. That is,

$$\kappa^* = \sqrt{4\pi\lambda_B \sum_{i=1}^{n_i} z_i^2 c_{s,i} \exp(-z_i\psi_c)} \quad (3.10)$$

and

$$Z_p^* = \frac{\gamma_0}{\kappa^*\lambda_B} \left[((\kappa^*)^2 R_{c,p} R_p - 1) \sinh \kappa^*(R_{c,p} - R_p) + (\kappa^*)^2 + \kappa^*(R_{c,p} - R_p) \sinh \kappa^*(R_{c,p} - R_p) \right], \quad (3.11)$$

where

$$\gamma_0 = \frac{-4\pi\lambda_B}{(\kappa^*)^2} \sum_{i=1}^{n_i} z_i c_{s,i} \exp(-z_i\psi_c), \quad (3.12)$$

from which the effective charge density for colloid p can be defined as

$$\sigma_p^* = \frac{Z_p^*}{4\pi R_p^2}. \quad (3.13)$$

The osmotic pressure of the colloidal dispersion can be approximated by the cell model and is given by

$$P = k_B T (c_{coll} + c_{ions,in} - c_{ions,res}), \quad (3.14)$$

with c_{coll} the concentration of the colloids, $c_{ions,res}$ the ion concentration of the reservoir, and $c_{ions,in}$ the ion concentration of the dispersion, *i.e.* the ion concentration at the edge of the cell(s). The latter can be re-expressed as

$$P = k_B T \left\{ \frac{\phi}{\bar{v}_p} + \sum_{i=1}^{n_i} c_{s,i} [\exp(-z_i\psi_c) - 1] \right\}, \quad (3.15)$$

where $\bar{v}_p = \sum_{p=1}^{n_p} x_p v_p$. This approximation for the osmotic pressure neglects, however, the contribution of the colloid-colloid correlations and is valid for low ionic strength and/or relatively large particle volume fraction only. For a detailed discussion see Refs. [142, 143, 92, 144].

3.2.2 Renormalized jellium model

In contrast to the cell model, the jellium model[145] is based on the fact that, for diluted suspensions, the colloid-colloid radial distribution function can be approximated to $g_{pp} =$

1. That is, the colloids can be seen as uniformly distributed throughout the suspension. The small ions are, on the other hand, strongly correlated with the colloids. Once again, the colloidal suspension can thus be reduced to a one-colloid subsystem immersed in an infinite sea of salt solution supplemented by a uniform background charge, namely $\xi = \xi_{back}$. Eq. 3.3 then becomes

$$\frac{\partial^2 \psi}{\partial r^2} + \frac{2}{r} \frac{\partial \psi}{\partial r} + 4\pi \lambda_B \left[\sum_{i=1}^{n_i} z_i c_{s,i} \exp(-z_i \psi(r)) + \xi_{back} \right] = 0. \quad (3.16)$$

The background charge represents nothing but the other colloids bearing a charge Z_{back} smeared out in space. In the case of a mono-disperse colloidal suspension of radius R , the particle volume fraction is thus a simple function of ξ_{back} . That is

$$\xi_{back} = Z_{back} \frac{3\phi}{4\pi R^3}. \quad (3.17)$$

As noted by Trizac *et al.*[66] in most of the cases Z_{back} is different from the bare charge of the colloids which must be renormalized by fitting the electrostatic potential tail obtained by means of Eq.3.16 with the known far field expression for $\psi(r)$, see below.

In order to keep the system electroneutral a Donnan potential is set at infinite separation from the colloid, *i.e.* $\psi(\infty) = \psi_D$, given by

$$\xi_{back} = - \sum_{i=1}^{n_i} z_i c_{s,i} \exp(-z_i \psi_D). \quad (3.18)$$

Furthermore, the condition of electroneutrality imposes,

$$\left. \frac{\partial \psi}{\partial r} \right|_{r \rightarrow +\infty} = 0. \quad (3.19)$$

The generalization of the renormalized jellium model to polydisperse colloidal suspensions is obtained simply by positing that the background charge is the charge density caused by a *uniform mixture* of colloidal species p bearing a charge $Z_{back,p}$, so that

$$\xi_{back} = \frac{\phi}{\bar{v}_p} \sum_{p=1}^{n_p} x_p Z_{back,p}, \quad (3.20)$$

where $\bar{v}_p = \frac{4}{3}\pi \sum_{p=1}^{n_p} x_p R_p^3$, or, equivalently, that the overall colloidal volume fraction is given by,

$$\phi = \frac{\bar{v}_p \xi_{back}}{\sum_{p=1}^{n_p} x_p Z_{back,p}}. \quad (3.21)$$

In other words, the continuity of the electrostatic potential and ion concentrations is ensured by imposing the same ξ_{back} for all colloidal species p .

The $Z_{back,p}$ values are obtained by an iterative procedure which consists in equating them to their respective effective charges, Z_p^* , obtained from a fit of the tail of the far-field electrostatic potential profile by the expression of the linearized potential, $\tilde{\psi}_p(r)$,

$$\tilde{\psi}_p(r) = \psi_D + \lambda_B \frac{Z_p^*}{1 + \kappa^* R_p} \frac{\exp(-\kappa^*(r - R_p))}{r}, \quad (3.22)$$

where

$$\kappa^* = \sqrt{4\pi\lambda_B \sum_{i=1}^{n_i} z_i^2 c_{s,i} \exp(-z_i\psi_D)}, \quad (3.23)$$

which thus gives a new value of ξ_{back} and $\psi_p(r)$, until convergence of Z_p^* for all colloidal species p ,

$$Z_{back,p}(Z_p^*) = Z_p^* \quad \forall p \in \{1, \dots, n_p\}. \quad (3.24)$$

Similarly to the cell model (Eq 3.15), the osmotic pressure of the colloidal dispersion can be expressed as

$$P = k_B T \left\{ \frac{\phi}{\bar{v}_p} + \sum_{i=1}^{n_i} c_{s,i} [\exp(-z_i\psi_D) - 1] \right\}. \quad (3.25)$$

Again, this expression neglects the contribution of the colloid-colloid correlations to the osmotic pressure.

3.2.3 Boundary conditions at the colloidal surface

So far, we have introduced the equation governing the electrostatic potential in the solution and the boundary conditions specific to the model used. In the following, we describe the boundary conditions relative to the surface of the colloids.

General conditions

For a colloid dressed with a bare surface charge density σ a general boundary condition can be expressed from the Gauss theorem

$$\left. \frac{\partial\psi}{\partial r} \right|_{r=R_p} = -4\pi\lambda_B\sigma, \quad (3.26)$$

In the case of a titrating surface charge a more convenient condition can be obtained from the electroneutrality condition and reads

$$\sigma = \frac{1}{R_p^2} \int_{R_p}^{R_c} dr r^2 \sum_{i=1}^{n_i} z_i c_{s,i} \exp(-z_i\psi(r)) \quad (3.27)$$

for the cell model and

$$\sigma = \frac{1}{R_p^2} \int_{R_p}^{\infty} dr r^2 \left[\sum_{i=1}^{n_i} z_i c_{s,i} \exp(-z_i \psi(r)) - \xi_{back} \right] \quad (3.28)$$

for the renormalized jellium model. The above boundary conditions, although necessary to solve the cell model and the renormalized jellium model do not prejudge (define) either the nature of the colloidal charge or the response of the latter to colloid density or to a change in the nature and concentration of the electrolyte solution.

Titration surface charge

In the case of a chemically inert colloid surface two conditions can be defined, namely the constant charge and constant potential conditions[127]. The first condition, however, gives rise to a nonphysical result when two such charged surfaces are in contact: the osmotic pressure becomes infinite! On the contrary, as two colloids approach, the second condition implies that σ drops and eventually completely vanishes on contact. The constant potential forms the lower bond of the charge regulation condition. It can also be seen as a cheap and implicit manner to qualitatively account for the chemistry of the interface, namely here the binding of the counter-ions.

In reality, the chemistry of the solid/solution interface is specific to the nature of both the surface and the electrolyte. This chemistry can be specified/defined along the chemical reaction equilibrium with associated Gibbs free energies. They are then coupled with the physical interactions undergone by the reaction products and reactants to form the generically-termed physical chemistry of interfaces. The chemical reactivity, in some sense, gives a fourth dimension to, and thus considerably enlarges the domain of possible states of colloidal systems.

Let us consider the situation in which the colloids bear titratable surface sites with a surface density d_s . The surface sites are either in a protonated state, $M-OH^{q_s^+}$ with charge q_s^+ and where M stands for any atoms, or deprotonated state, $M-O^{q_s^-}$ with charge q_s^- , depending on the equilibrium pH of the reservoir. Their partition can be conveniently quantified by the ionization fraction, $\alpha = N_{M-O^{q_s^-}} / (N_{M-OH^{q_s^+}} + N_{M-O^{q_s^-}})$. The bare surface density is then obtained from $\sigma = d_s(\alpha q_s^- + (1 - \alpha)q_s^+)$. The change in charge state of the surface sites with pH obeys the following chemical equilibrium



and associated equilibrium constant, a function of the Gibbs free energy,

$$K_a = \exp(-\beta\Delta G) = \frac{a_{\text{M-O}^{\text{s}-}} a_{\text{H}^+}}{a_{\text{M-OH}^{\text{s}+}}}, \quad (3.30)$$

where the a_s represent the chemical activities. Using the surface concentration for the definition of the standard composition[146], $\Gamma_s = d_s/N_A$ where N_A is the Avogadro number, the chemical activity of any chemical species at the colloid interface can be written as

$$a_s = \Gamma_s \exp(q_s \psi_s), \quad (3.31)$$

The fraction of deprotonated sites is obtained by combining Eqs. 3.30-3.31 and reads

$$\ln \frac{\alpha}{1-\alpha} = \ln 10 (\text{pH} - \text{p}K_a) - \psi_s (q_s^- - q_s^+). \quad (3.32)$$

Finally, a Stern layer of thickness λ_{Stern} is introduced around each colloids to account for the hydrated size of the ions and the hydration layer of the colloids[147]. The surface sites are considered to reside within this layer, that is, on the unhydrated surface of radius $R_p - \lambda_{\text{Stern}}$. Disregarding dielectric discontinuities, ψ_s can be deduced from the diffuse layer electric potential $\psi_d(R_p)$. It can be defined by the following expression

$$\psi_s = \psi(R_p) + \frac{4\pi\lambda_B\lambda_{\text{Stern}}}{1 + \lambda_{\text{Stern}}/R_p}\sigma, \quad (3.33)$$

obtained from the definition of the capacitance [148] for a spherical particle. Eqs. 3.29, 3.32, 3.33 form the basis of the 1-pK Stern model. With the model specific boundary condition (Eq. 3.5 for the cell model and Eq. 3.19 for the renormalized jellium model), Eq. 3.3 can be solved for each particle size at any given pH. The detailed algorithms are described in the next section.

3.2.4 Algorithm description

The Poisson-Boltzmann equation, thereafter referred to PBE, was numerically solved with an ‘‘in house’’ code based on the Newton Gauss-Seidel method[68], see §1.5.5 for more details. For a particle of radius R_p , and for a given pH, the potential profile $\psi(r)$ is calculated by the following algorithm:

1. Choose a first guess for the potential at $r = R_p$, ψ_d , within a range $[\psi_d^m, \psi_d^M]$.
2. Solve the PBE with a given $\psi(R) = \psi_d$.

3. Compute σ (Eq. 3.26-3.27) and $\text{pH}(\psi_d)$ (Eq. 3.32).
4. If $\text{pH}(\psi_d) - \text{pH}$ is small enough, stop the program and return the results.
5. Dichotomy step:
 - if $\text{sign}[\text{pH}(\psi_d) - \text{pH}] = \text{sign}[\text{pH}(\psi_d^M) - \text{pH}]$, $\psi_d^M := \psi_d$;
 - else $\psi_0^m := \psi_d$; $\psi_d := (\psi_d^m + \psi_d^M)/2$;
 Go to step 2.

If instead of the pH , one sets the bare charge as a constant parameter, pH and $\text{pH}(\psi_d)$ in step 5 have to be replaced by σ and $\sigma(\psi_d)$, respectively.

The polydisperse cell model can be advantageously solved, not by imposing a particle volume fraction, but, instead, by setting the same electrostatic potential ψ_c at the cell edge for all colloidal families, i.e. the condition defined by Eq. 3.8. The particle volume fraction is then calculated *a posteriori*. That is, for a given ψ_c the corresponding set of cell radii $\{R_{c,p}\}_{p=1,\dots,n_p}$ is calculated iteratively by solving Eq. 3.3 in such a way as the condition defined by Eq. 3.8 is respected and by imposing the boundary conditions defined by Eqs. 3.5, 3.27, 3.32, and 3.33. ϕ is then calculated with Eq. 3.7. The proposed algorithm is summarized below:

1. Choose a potential at the cell edge ψ_c .
2. For each colloidal species p choose a first guess $R_{c,p}$, within a range $[R_{c,p}^m, R_{c,p}^M]$.
3. For each p solve the PBE for a given pH , see 3.2.4.
4. For each p extract $\psi_p(R)$.
5. If $|\psi_p(R_{c,p}) - \psi_c|$ is small enough, go to step 7.
6. Dichotomy step:
 - if $\text{sign}[\psi_p(R_{c,p}) - \psi_c] = \text{sign}[\psi_p^M(R_{c,p}) - \psi_c]$, $R_{c,p}^M := R_{c,p}$;
 - else $R_{c,p}^m := R_{c,p}$; $R_{c,p} := (R_{c,p}^m + R_{c,p}^M)/2$.
 Go to step 3.
7. Calculate $Z^*_{p=1,\dots,n_p}$, ϕ (Eq. 3.7), and P (Eq. 3.25)

The polydisperse jellium model is simpler to solve since it eliminates the cell radius and the corresponding adjustment. In fact, no iteration is required if it is solved from a set value of the background charge. Alternatively, a given ϕ can be achieved by iteratively adjusting the background charge. The proposed algorithm reads:

1. Choose a background charge potential ψ_D . (see Eq. 3.18).
2. For each colloid p compute the potential profile $\psi_p(r)$ at a given pH (see 3.2.4) for a given ψ_D .
3. Calculate $Z^*_{p=1,\dots,n_p}$, then ϕ (Eq. 3.21), and P (Eq. 3.15).
4. Optionally, if a given ϕ_{goal} is imposed, inverse Eq. 3.21 with $\phi = \phi_{goal}$ to obtain a new ψ_D and go to step 2, unless $|\phi(\psi_D) - \phi_{goal}|$ is small enough.

The application to continuous size distribution of the PCM and PRJM takes advantage of the continuous variation of the effective charge with its curvature and is simplified with the proposed algorithm where the particle volume fraction is not an input parameter but calculated *a posteriori*. For relatively small adimensional curvatures the charge scales linearly with $1/\kappa R_p$, $\sigma^*(R_p) = \sigma^*_{plane}(1 + A(\kappa R_p)^{-1})$, while for large $1/\kappa R_p$ it scales quadratically, $\sigma^*(R_p) = \sigma^*_{plane}(1 + A(\kappa R_p)^{-1} + B(\kappa R_p)^{-2})$, see the results section for more details.

The source code for the PRJM and PCM, along with examples, is available at this address: <https://github.com/guibar64/polypbren>.

3.2.5 Suspensions and model details

As specified earlier, we focus in this chapter on polydisperse suspensions of titratable silica (SiO₂) nano-particles with continuous size distribution. As silicon is one of the major elements of the Earth's crust, the chemistry and, of particular interest here, the surface chemistry of SiO₂ are quite well defined and documented. The surface of SiO₂ is covered with titratable silanol groups with a surface density d_s . These titrate with pH according to the following equilibrium reaction



The corresponding equilibrium constant, pK_a , as well as the thickness of the Stern layer, λ_{Stern} and d_s were fitted against experimental titration data as obtained by Dove *et al.*

[149], see Sect. 3.3.1. These parameters were then maintained constant for all other calculations. A large number of calculations were made with size distributions corresponding to commercially available silica suspensions, namely Ludox HS40 and TM50 suspensions, thereafter denominated HS40 and TM50, respectively. They are described in detail elsewhere [150, 8, 151, 9]. In short, we used a gamma distribution for the HS40 and a normal distribution for the TM50. In particular, for HS40, an average radius of 8.14 nm and a polydispersity of 14 % and for TM50, $\langle R_p \rangle = 12.1$ nm and a polydispersity of 12 % were used. Calculations were also performed with various distribution shapes and varying polydispersities as indicated in the text.

All the calculations were performed at a finite concentration (5 mM for most of them) of a mono-monovalent salt, $T = 300$ K and $\lambda_B = 0.7105$ nm.

3.3 Results

Before comparing the generalized cell and renormalized jellium models, the charging process of silica is presented and modeled to extract the ionization constant, the density of titratable sites and the thickness of the Stern layer.

3.3.1 Charging process of silica

Figure 3.1 presents the titration curve of silica in NaCl salt solution at three different concentrations, these data were obtained by Dove *et al.* [149]. The surface charge density (in absolute values) increases with increasing pH due to the progressive dissociation of the silanol groups. σ is also seen to increase with the salt concentration as a result of a greater screening of the electrostatic repulsion between charged sites. The following set of parameters, $pK_a = 7.7$, $d_{site} = 5.55 \text{ nm}^{-2}$ and $\lambda_{Stern} = 0.107$ nm, is found to provide a good description of the charging process of silica. Note that these parameters were obtained with Eq. 3.32 assuming a planar surface in the limit of infinite dilution. They are kept constant in the rest of the chapter. The surface charge densities of a planar silica surface for several pH values and conditions used throughout this study are given in Table 3.1.

σ titrates with pH but also regulates as the particle volume fraction increases. The drop of σ with ψ is illustrated in Fig. 3.2 for the particle family of radius 5.5 nm in

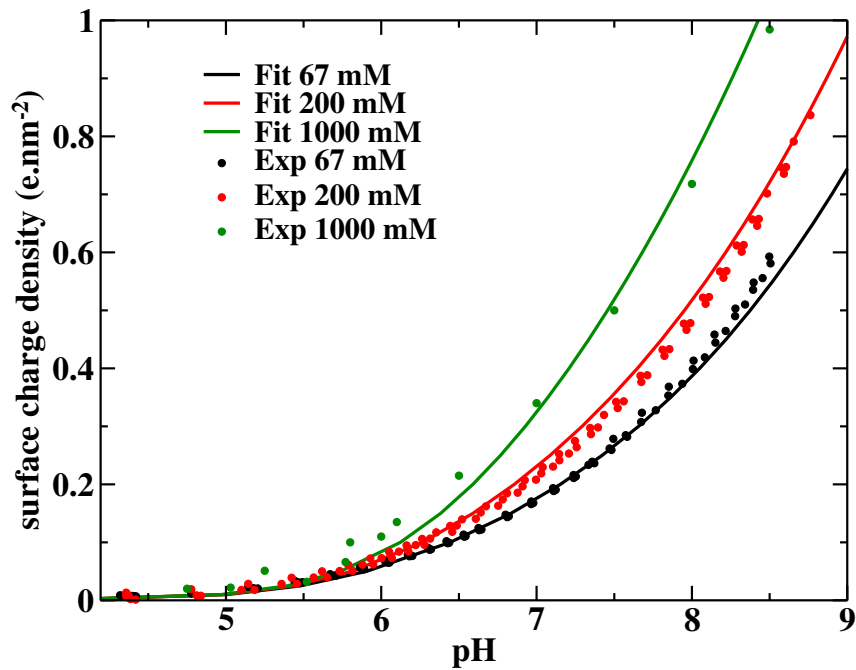


Figure 3.1: Comparison of experimental and simulated bare surface charge density versus pH for silica in aqueous solution at different NaCl concentrations. The simulations are represented by solid lines, the experimental data by points. The salt concentrations are 67 mM (black), 200 mM (red), 1000 mM (green). The experimental data are from Dove *et al.*[149].

pH	Surface charge (e.nm ⁻²)
7	0.0816
8	0.18
9	0.365
9.5	0.508
10	0.695
10.5	0.932

Table 3.1: pH and bare surface charge density calculated for a planar silica surface in a monovalent salt solution with $c_s = 5$ mM, $\lambda_B = 0.7105$ nm, $pK_a = 7.7$, $d_{site} = 5.55$ nm⁻², $\lambda_{Stern} = 0.107$ nm.

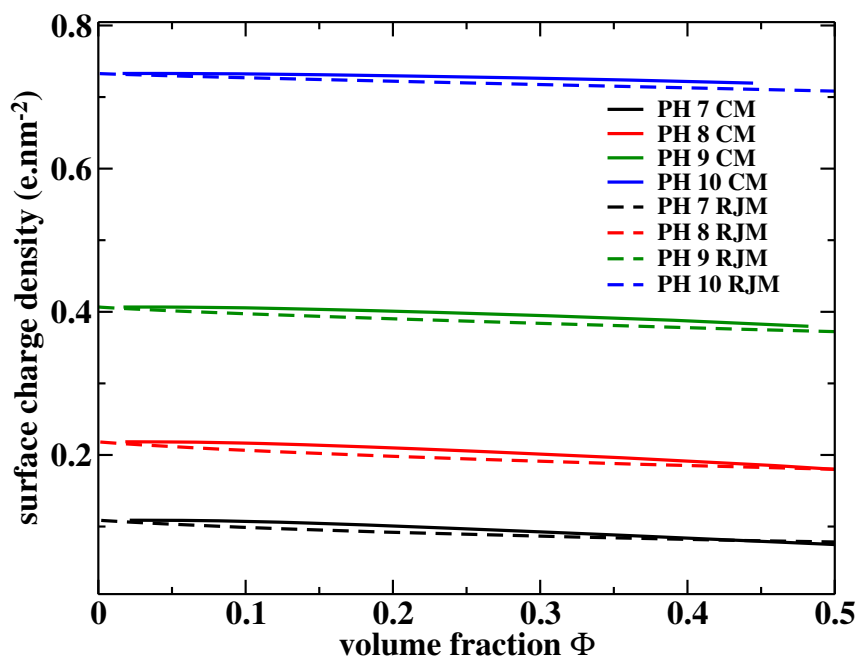


Figure 3.2: Calculated bare surface charge density for silica particles with $R_p = 5.5$ nm when varying the particle volume fraction of a polydisperse HS40 suspension in monovalent salt solution at different pHs: 7 (black), 8 (red), 9 (green), and 10 (blue). The results are presented both with the PCM (solid lines) and PRJM (dashed lines) approximations. The salt concentration is set to 5 mM.

an HS40 suspension (polydispersity 14%) dispersed in a monovalent salt solution. This trend is similar in the PCM and PRJM and is explained by the co-ion exclusion which effectively mimics the strong interactions of the colloidal particles with their neighbors. The calculated σ , although close, tends to be larger within the PCM than the PRJM. This discrepancy increases as the pH is depressed (<10% at pH 7, and <1% at pH 10).

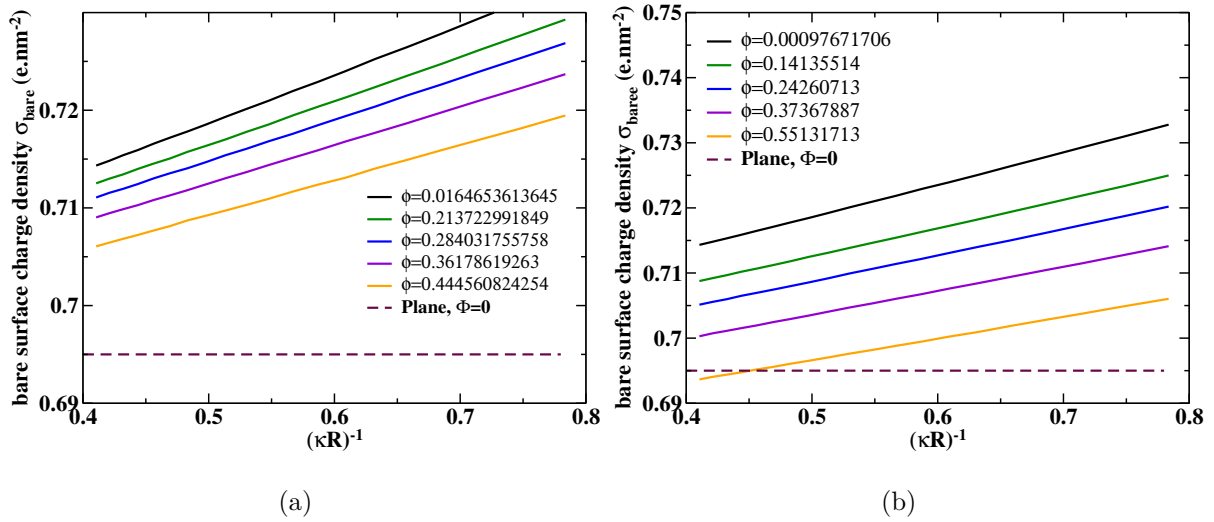


Figure 3.3: Bare surface charge σ versus dimensionless curvature $(\kappa R)^{-1}$ at pH 10 and several volume fractions (see legend), for the PCM (a) and the PRJM (b). The surface charge for a planar surface at infinite dilution ($\phi = 0$) are displayed in both cases with a purple dashed line.

A result of the charge titration is also the curvature dependence of the particle charging. In particular, Abbas and coworkers[152] showed that there is a considerable increase in the surface charge density for particles smaller than 10 nm in diameter. The rise in charge up with particle curvature can be understood as an enhanced screening of small sized particles by counter-ions as compared to that of large particles. This is illustrated in Fig. 3.3 as a function of the dimensionless curvature $(\kappa R_p)^{-1}$ at pH=10 for various ϕ of the HS40 silica particle dispersion. The calculations are performed both in the PCM and PRJM approximations and are compared to the planar case at infinite dilution. Interestingly, the curvature dependence of σ is found to vary linearly with $(\kappa R_p)^{-1}$. This can be explained by the Taylor development of σ with respect to $(\kappa R_p)^{-1}$ which in the limit of $\kappa R_p \gg 1$ takes the form

$$\sigma = \sigma_{\text{plane}}(1 + A_0(\kappa R_p)^{-1}), \quad (3.35)$$

where σ_{plane} is the surface charge density of a planar surface and A_0 gives the slope. Note that here it also applies to relatively small $(\kappa R_p)^{-1}$. It should be mentioned, however, that in the pH region of large charge regulation, typically for pH values close to pK_a [153], the linear relationship only holds for $\kappa R_p > 2$, not shown. The slope of $\sigma(1/\kappa R_p)$ is seen to decrease slightly with the particle volume fraction as a result of increasing counter-ion screening which tends to moderate, in relative terms, that due to curvature. Also, in the domain of large ϕ , the σ of the small particles becomes lower than σ_{plane} in the reference state (i.e. $\phi = 0$), see e.g. Fig. 3.3-b. In the infinite dilution limit where a Grahame relation for the nonlinear PBE in the spherical geometry has been recently obtained [154], an analytical expression for A_0 can be found. It reads

$$A_0 = \frac{1}{\cosh^2(\psi_{0,plane}/4) + \frac{C\sigma_{plane}\kappa\lambda_{Stern}}{2q_s \tanh(\psi_{0,plane}/2)}} + \frac{C\sigma_{plane}\kappa\lambda_{Stern}}{2q_s \tanh(\psi_{0,plane}/2)} \frac{1}{1 + \frac{1/(1-\alpha_{plane}) + C\sigma_{plane}}{2q_s \tanh(\psi_{0,plane}/2)}}. \quad (3.36)$$

A detailed development is given in the Appendix below.

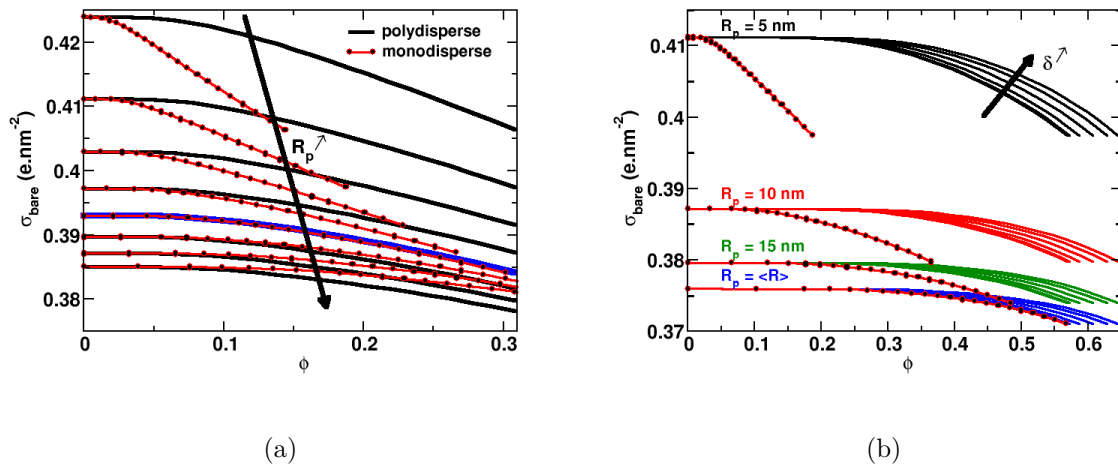


Figure 3.4: Bare surface charge density, σ , for particle suspensions immersed in a 5 mM 1-1 salt solution at pH 9 for various particle sizes, size distributions and particle volume fractions a) σ for particles of various R_p (4, 5, 6, 7, 8, 9, 10 and 11 nm) within HS40 suspensions in comparison with the corresponding monodisperse cases. The blue line gives that of particles with $R_p = \langle R_p \rangle$. b) The same as in (a) but for particle suspensions having a normal radii distribution with $\langle R_p \rangle = 20$ nm at different polydispersities δ (5, 10, 20, 30, 40 and 50 %). σ of monodisperse particle suspensions (red lines with symbols) are also given for comparison.

The influence of polydispersity on the bare surface charge density of different parti-

cle families, i.e. with different R_p , is illustrated in Fig. 3.4 which compares the case of polydisperse and monodisperse suspensions for various particle size distributions. Interestingly, for particles with R_p equal to the mean value of the distribution, $R_p = \langle R_p \rangle$, the polydispersity, when it is relatively small ($<15\%$), has virtually no impact on σ . As could be expected, this is the same for infinitely diluted suspensions whatever the particle family or polydispersity, see Fig. 3.4-b. On the contrary, as R_p departs from $\langle R_p \rangle$, the σ of mono- and poly-disperse suspensions can clearly be seen to differentiate and this differentiation steps up with ϕ and the departure from $\langle R_p \rangle$. The polydispersity effect is more pronounced for the small particles of the size distribution. In addition, polydispersity yields them higher charges (compared to monodispersity) which monotonically increase with it. The opposite is found for the large particles.

3.3.2 Renormalized parameters

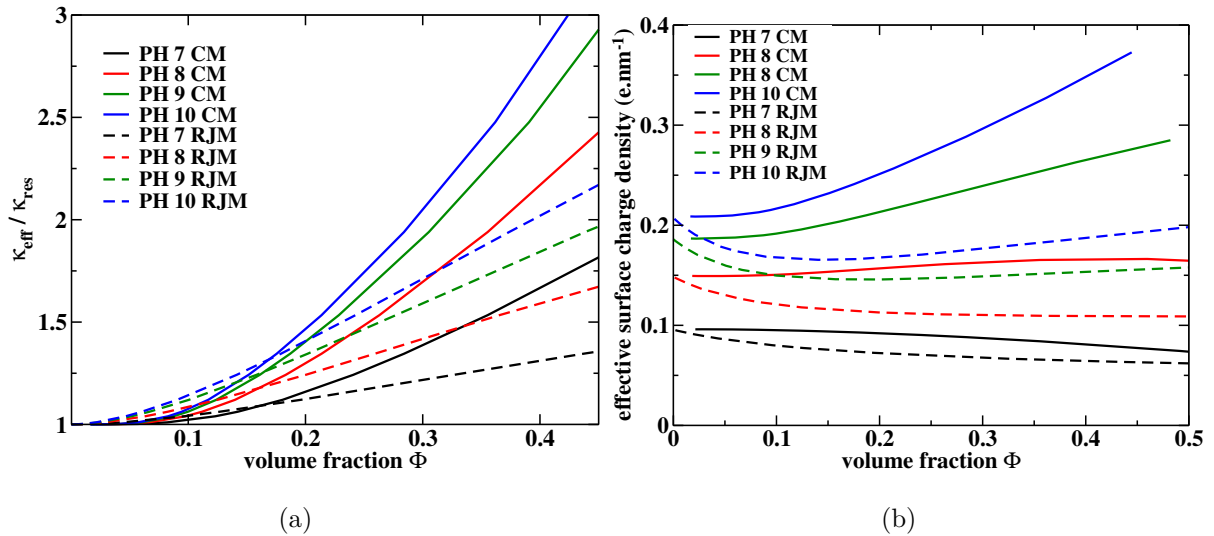


Figure 3.5: a) Relative effective inverse screening length κ^*/κ , and b) effective surface charge density σ^* versus volume fraction ϕ , for particles with $R_p = 5.5$ nm of the HS40 dispersion, at the following pHs: 7 (black), 8 (red), 9 (green) and 10 (blue). The ionic strength is set to 5 mM. The full lines give the results of the PCM while the dashed lines those of the PRJM.

So far we have seen that the bare surface charge densities as obtained from the PCM and PRJM approximations are very similar whatever the particle size distribution or particle volume fraction. This is no longer true for the renormalized charge and screening

length as shown in Fig. 3.5. These parameters are calculated for HS40 suspensions at various ϕ .

σ^* obtained within the PRJM is found to be lower than that within the PCM, whatever the ϕ and all the more so as pH increases, that is as the effective charge approaches saturation. The same is observed for κ^* but in the domain of large ϕ ($\phi \gtrsim 0.15$) while the opposite is found, that is $\kappa_{RJM}^* > \kappa_{CM}^*$, in the dilute and semi-dilute regimes ($\phi \lesssim 0.15$). These results are consistent with those obtained by Trizac *et al.* with monodisperse suspensions, see Refs [66, 143], but are here exacerbated by the polydispersity. In particular, κ^* values of both models are found not to converge in the limit of large ϕ , the domain of counter-ion dominated systems (supposedly equivalent to the salt free case), but, instead, to become increasingly divergent even at low pH values. Note that in the salt free case (not shown), σ^* is still distinctly lower in the RJM, but the κ^* of both models are found to be similar in the domain of low ϕ (< 0.2).

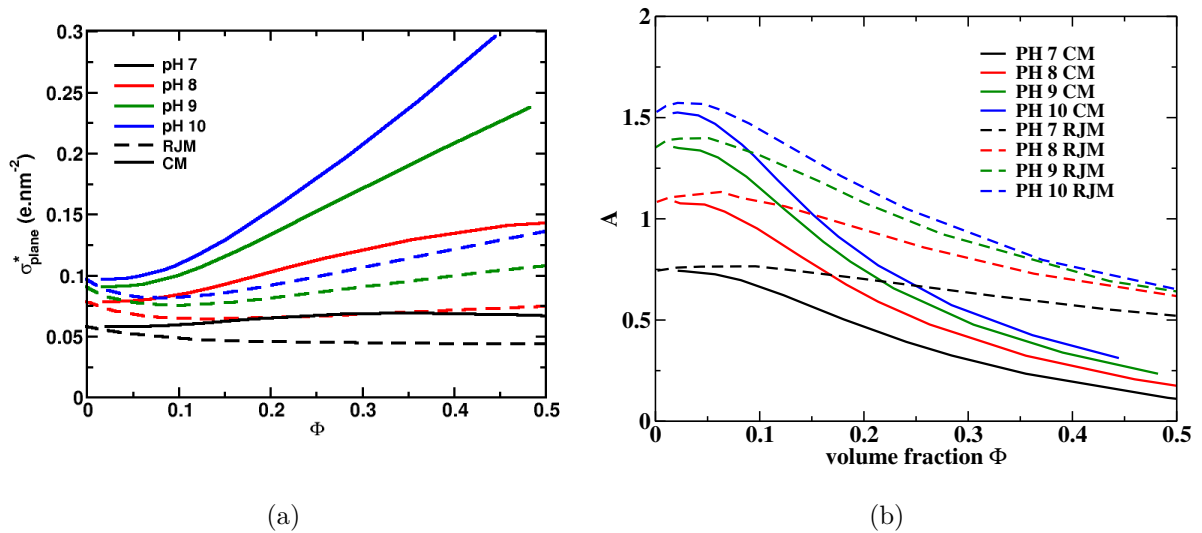


Figure 3.6: Effective surface charge density of the planar surface σ_{plane}^* and factor A versus volume fraction ϕ . Those were worked out for the HS40 distribution, and for the following pHs: 7 (black), 8 (red), 9 (green), and 10 (blue), using the PCM (full lines), and the PRJM (dashed lines) .

In the same way as for the bare surface charge density, the effective surface charge density can be accurately approximated by means of an affine function of $(\kappa^* R_p)^{-1}$, that is,

$$\sigma^* = \sigma_{plane}^* \left(1 + A(\kappa^* R_p)^{-1} \right), \quad (3.37)$$

where σ_{plane}^* is the effective surface charge density of the confined planar surface in the

same conditions (pH and ϕ , i.e. same edge potential for the PCM and same background charge for the PRJM) and A is a dimensionless coefficient which measures the impact of the size of the particle. σ_{plane}^* and A depend on the model, pH, particle size distribution and volume fraction. Equivalently, Eq. 3.37 can be written in terms of effective charge, that is $Z^*/R_p = 4\pi\sigma_{plane}^*/\kappa^*(\kappa^*R_p + A)$. In the case of no added salt, after noting that $\sigma^* = \frac{\gamma\kappa^*}{\pi\lambda_B}$, where γ is a coefficient which varies with σ and ϕ [141], it was found that Z^* scales linearly with the ratio R_p/λ_B . Such linear scaling was verified experimentally for deionized colloidal suspensions in the infinite dilution limit, in the semi-dilute regime and in the concentrated regime by measurements of electrophoretic mobility of isolated colloids[155, 156], conductivity of colloidal liquids and elasticity of colloidal crystals[133], respectively.

In the case of added salt ($\kappa R_p \gg 1$) and infinite dilution limit, where an analytical expression of the electrostatic potential solution of the non linear Poisson Boltzmann theory has been obtained [157, 158], an analytical approximation of the coefficient A for non titrating colloids can be obtained and reads,

$$A = \frac{1}{2} \left(5 - \frac{\gamma^4 + 3}{\gamma^2 + 1} \right), \quad (3.38)$$

where $\gamma = \sqrt{1 + x^2} - x$ and $x = \frac{\kappa}{2\pi\lambda_B\sigma}$. The approximation is asymptotically exact in the limit of large R , see the Appendix for a detailed development. Finally, since γ goes to 1 when $\sigma \rightarrow \infty$ one finds $A_{sat} = 3/2$ at the saturation of the colloidal charge.

Fig. 3.6 shows the PCM and PRJM results of the coefficient A and the effective surface charge density of the plane, σ_{plane}^* , versus ϕ on HS40 at different pH and a set ionic strength of 5 mM. Not surprisingly, σ_{plane}^* follows the same trend as for $\sigma_{5.5\text{ nm}}^*$, c.f. Fig. 3.5(b). In particular, for pH values greater than the pK_a (pH > 7.7) PRJM's σ_{plane}^* systematically shows a non monotonous behavior with respect to ϕ with a minimum around $\phi \approx 0.1$. Within the PCM, on the other hand, σ_{plane}^* continuously rises with ϕ . The difference in behavior in σ_{plane}^* between the two models is reminiscent of that of σ_{plane}^* at saturation which follows the same qualitative trend, see e.g. Ref. [159]. Indeed, in these conditions of pH, σ_{plane} is generally larger than $\sigma_{plane,sat}^*$. For pH values lower than the pK_a and at relatively high ϕ the PCM's σ_{plane}^* also shows a drop due to the regulation of the bare surface charge density which becomes much smaller than σ_{plane}^* at saturation.

This qualitative difference is echoed in the coefficient A which shows a maximum value in the PRJM and not in the PCM, see Fig. 3.6-b. Indeed, A varies between a maximum

value A_{sat} , at the saturation of the charge and a minimum value A_0 when $\sigma^* = \sigma$, c.f. Eq. 3.35. It naturally follows that $\sigma^*(R_p)$ desaturates as ϕ further increases and approaches the ideal planar limit where the effective charge is proportional to R_p^2 . In this respect, the PCM's A values decrease faster with ϕ than is the case in the PRJM. In addition, for non titrating surfaces $A_0 = 0$ ($\sigma(R_p) = \sigma_{plane}$) and, as we have seen above, $A_{sat} = 1.5$ at $\phi = 0$ both for titrating and non titrating surfaces.

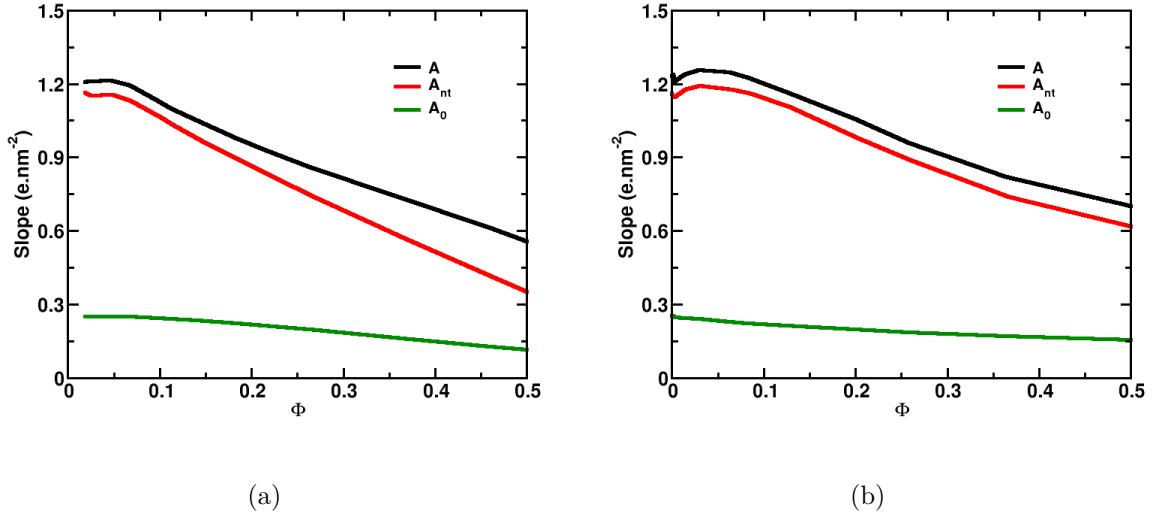


Figure 3.7: Slopes of the linear variation of σ^* with $(\kappa R_p)^{-1}$ of a titrating, A , and a non-titrating colloidal particle, A_{nt} . That of the bare surface charge density, A_0 , is also given as a reference. The slopes are given for both the PCM (a) and PRJM (b). Calculations are performed for silica HS40 dispersions in equilibrium with a bulk solution containing 5mM of 1-1 salt and at pH 8. In the non titrating case, the particles are given a surface charge density equal to that of the planar silica surface in the same conditions.

This points to the fact that for non titrating colloids, with a $\sigma(R_p, \phi)$ equal to that of a titrating planar surface in the same conditions ($\sigma_{plane}(\phi, \text{pH})$), the corresponding coefficient, A_{nt} , is lower than A for charge regulating particles. In other words, A is a function of A_0 and A_{nt} , see Figure 3.7. In the limit of small variations of σ , one can further give an analytic approximation for the dependence of A on A_0 and A_{nt} which reads,

$$A \approx A_{nt} + \frac{\kappa^*}{\kappa} A_0 \frac{\sigma_b}{\sigma^*} \frac{d\sigma^*}{d\sigma_b}. \quad (3.39)$$

Close to the saturation of the effective charge as well as in the limit of small σ_p the last expression reduces to $A \approx A_{nt} + \kappa^*/\kappa A_0$.

Not shown here is how the ionic strength affects both σ_{plane}^* and A . This is already well documented in the literature in the case of monodisperse suspensions, see e.g. Refs. [160, 161, 162]. Not surprisingly, the same qualitative behavior is found in polydisperse suspensions. That is, A drops and σ^* rises when ionic strength increases. It is also easy to infer from Eqs. 8-22 and Fig. 3.4 that an increase in the polydispersity gives rise to a shift in σ_{plane}^* and A values to larger ϕ values.

In conclusion of this section, we have seen that the well-known linear scaling of the effective charge with $(\kappa R_p)^{-1}$ is also verified in the case of polydisperse and charge regulating colloids for all ϕ . In practice, this means that a complete force field for these suspensions can be obtained at relatively low computational cost. Indeed, this amounts to calculating A , σ_{plane}^* and κ^* with a few R_p values (in principle two are enough) at set values of ψ_c (in the PCM) or Z_{back} (in the PRJM), and post-calculating ϕ given the particle size distribution (continuous or not).

3.3.3 Osmotic pressure

In this section the effect of the polydispersity on osmotic pressure is discussed. Finally, the validity of the PRJM and PCM will be discussed in light of experimental equation of states for various commercial silica dispersions as measured by L. Goehring, B. Cabane, J. Li and P-C Kiatkirakajorn[150, 8, 151, 9].

Figure 3.8 gives the microion contribution to the total osmotic pressure, P_{micro} as obtained from the PCM with different polydisperse suspensions having a normal size distribution of the same mean particle size $\langle R_p \rangle = 20$ nm but of varying polydispersities. P_{micro} is found to decrease as δ increases. The drop in P_{micro} is significant above 10% of polydispersity. The PRJM exhibits the same qualitative behavior (not shown).

The shape of the particle radius distribution is further found to have only a minor effect on P_{micro} . This is all the more true as the particle size distributions are chosen so as to have identical $\langle R_p^3 \rangle$ and $\langle R_p \rangle$. As shown in Figure 3.9-a for three different distribution shapes, when these conditions are met the P_{micro} thus obtained can hardly be distinguished. This behavior is a direct consequence of the geometrical definition of the particle volume fraction, see Eq. 3.6 combined with the very slow variation in the water layer thickness, $R_{cell} - R_p$, with the particle radius. In the limit of large κR_p , $R_{cell} - R_p$ becomes constant.

Fig. 3.10 compares the experimental equations of state of the HS40 and TM50

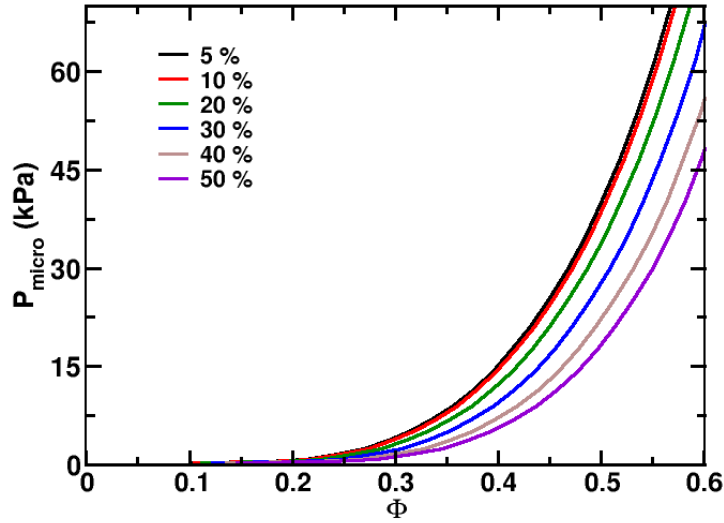


Figure 3.8: Simulated microion contribution to the osmotic pressure of titrating silica particle dispersions as a function of the particle volume fraction for varying polydispersities. The calculations are performed within the PCM approximation. The silica particles are suspended in a 5 mM 1-1 salt solution at pH 9. The particles present a normal size distribution with $\langle R_p \rangle = 20$ nm. The polydispersity is changed as indicated in the legend.

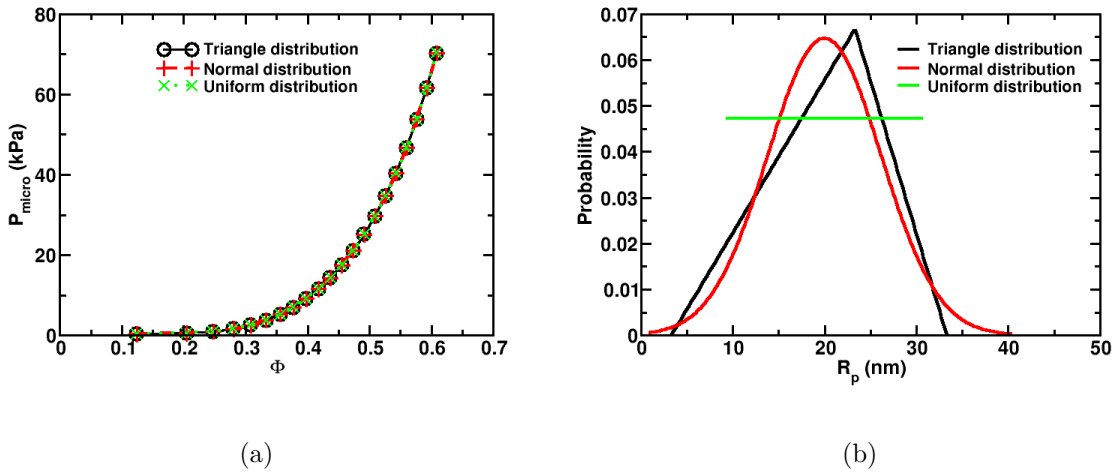


Figure 3.9: (a) PCM calculations of the micro-ions osmotic pressure, P_{micro} , for silica dispersions with varying shapes of particle size distribution but with identical $\langle R_p \rangle$ (20 nm) and $\langle R_p^3 \rangle$ (21.77^3 nm³). The silica particles are suspended in a 5 mM 1-1 salt solution at pH 9. Note that for the normal distribution $\delta = 31\%$. The distribution is changed as indicated in the legend. (b) The triangular, normal and uniform size distributions used.

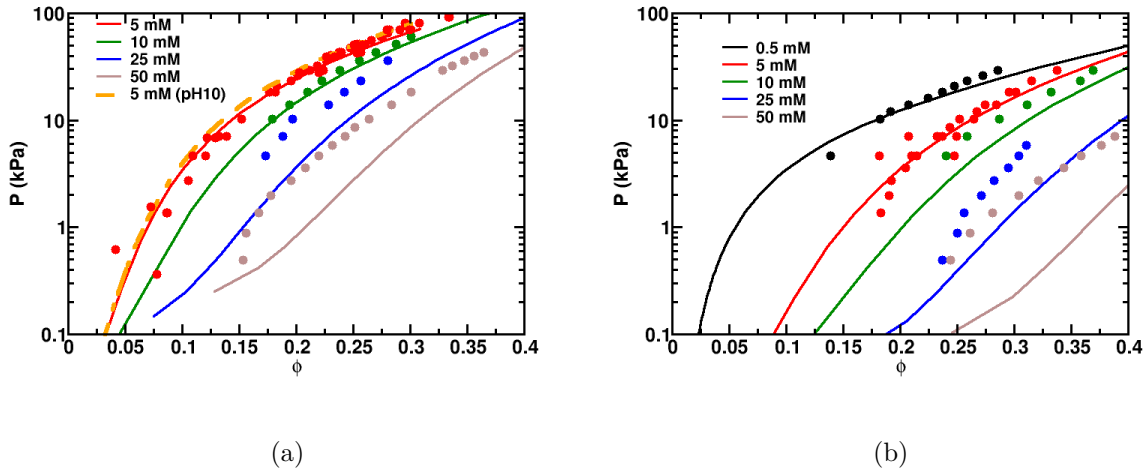


Figure 3.10: Experimental equation of state for the (a) HS40 and (b) TM50 silica dispersions in comparison with the micro-ion pressure calculated by the polydisperse cell model at various bulk concentrations of monovalent salt and pH 9. The experimental data are from L. Goehring, B. Cabane, J. Li and P-C Kiatkirakajorn[150, 8, 151, 9].

silica dispersions[151] with the micro-ion pressure calculated with the polydisperse cell model at various bulk concentrations of monovalent salt and pH 9. The osmotic pressure is seen to increase when the ionic strength of the bulk and the mean particle radius ($\langle R_p(\text{HS40}) \rangle < \langle R_p(\text{TM50}) \rangle$) decreases, in good agreement with the polydisperse cell model. What is more, the PCM is found to give a good description of the osmotic pressure of the silica dispersions only for the lowest bulk salt concentrations studied, up to 10 mM for the HS40 and to 5 mM for the TM50. This should not come as a surprise since the PCM is known to neglect the colloid-colloid correlations (entropic and contact contributions) to the osmotic pressure, as explained at length in refs[143, 163, 92, 164, 144]. In short, the PCM approximation is good as long as the colloid-colloid contribution to the osmotic pressure is negligible compared to the microion contribution that is when the mean separation between the colloids is a few times smaller than the interaction range. A consequence, found here when one compares the HS40 and TM50 results, is that the lower the mean particle size (that is the smaller the mean colloid separation), the larger the validity range of the PCM.

Fig. 3.11 compares the experimental equations of state of the HS40 and TM50 silica dispersions[151] with the micro-ion pressure calculated with the PRJM at various bulk concentrations of monovalent salt and at pH 9. The PRJM is found to give a poor

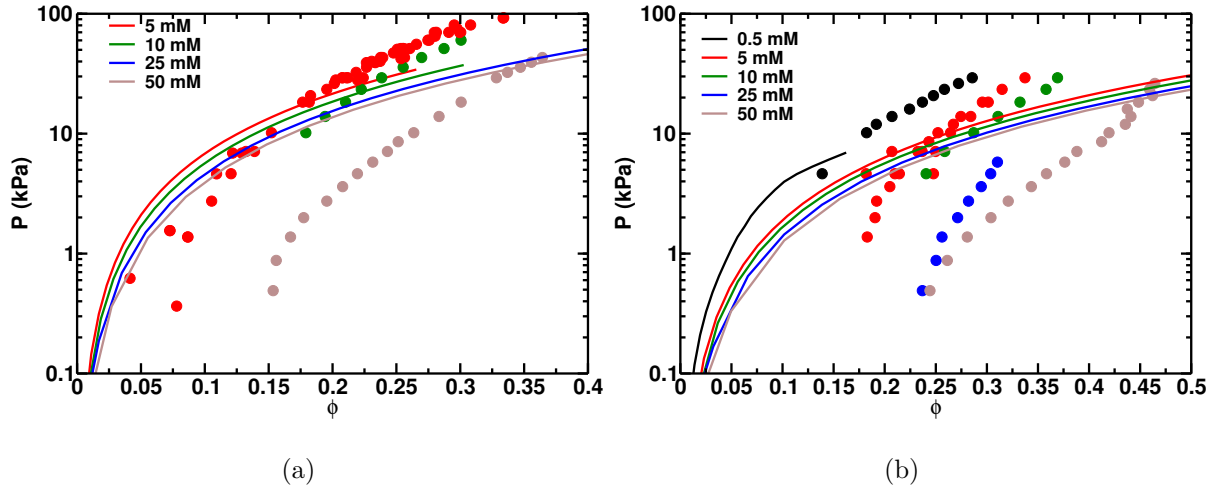


Figure 3.11: Experimental equation of state for the (a) HS40 and (b) TM50 silica dispersions in comparison with the micro-ion pressure calculated by the PRJM at various bulk concentrations of monovalent salt and pH 9.

description of the experimental osmotic pressure. Generally, it is found that the osmotic pressure is overestimated at low volume fractions and underestimated in the concentrated regime.

3.4 Conclusion

In this chapter, we proposed a cell and a renormalized jellium model to study the thermodynamic properties and estimate the renormalized parameters to be used in a one-component model, i.e. Z^* and κ^* , for polydisperse suspensions of titratable spherical colloids with a continuous size distribution. We further proposed a simple algorithm and a Nim implementation to solve them. The models are largely inspired by the work of Torres[101] on binary mixtures of colloids with constant charge. PCM and PRJM include a charge regulation, instead of a constant charge boundary condition, modeled as a simple 1-pK-Stern model. The application of the models to continuous size distributions was made simple and easy by the linear scaling of both the bare and effective charges with the adimensional curvature of the particles, $(\kappa R_p)^{-1}$. For very small $(\kappa R_p)^{-1}$, σ and σ^* scale quadratically. We presented a detailed example of such an analysis in the case of aqueous suspensions of silica nanoparticles of various size distributions. Besides being simple, the 1-pK model was found to give a very good description of the charging behavior for bare silica surfaces experimentally observed in diluted conditions, in accordance with previous

studies, see e.g. Ref. [165]. This allowed us to constrain the surface chemistry parameters of the PCM and PRJM, leaving us with two commonly characterized parameters, that is the pH and the particle size distribution. Both models give the same qualitative results. Yet, the cell model thus generalized is found to predict much more accurately the equations of state of aqueous silica dispersions at finite salt concentrations. In general, the bare surface charge density is found to drop as the density and the radius of the silica particles increases, due to the charge regulation. In a polydisperse suspension, the particles of radius $R_p < \langle R_p \rangle$ are further found to bear a surface charge density significantly greater than that of the same particles at the same density but in a monodisperse suspension (the opposite occurs when $R_p > \langle R_p \rangle$). This is all the more true as polydispersity rises and R_p is small compared to $\langle R_p \rangle$ ($R_p \gg \langle R_p \rangle$). In other words, the bare charge polydispersity is found to increase with the size polydispersity. Not surprisingly, the same trend is found for the effective charge polydispersity. It should be stressed, however, that a polydispersity of effective charges is also present in the case of polydisperse particles having the same bare surface charge density, although less pronounced. Despite these differences a significant impact on the microion osmotic pressure is only seen in suspensions of silica particles with very large polydispersities ($> 15\%$). One may expect, however, to observe more clear effects in the micro-structure of these suspensions, even for relatively small polydispersities.

Acknowledgements

I would like to thank Lucas Goehring and Joaquim Li for providing us with their experimental osmotic pressure data, as well as Bernard Cabane and Robert Botet for helpful discussions.

Appendix

Analytical expression for A_0

In this section a detailed development of the analytical expression for the slope, A_0 , of the linear variation of the bare surface charge density of spherical colloids with $(\kappa R)^{-1} \ll 1$ is given.

Carvalho *et al* [154] showed that for colloids with a small dimensionless curvature, $\zeta = (\kappa R)^{-1} \ll 1$, their bare surface charge density, σ , is related to the diffuse layer potential, $\psi_d = \psi(R)$, (see Eq. A14 in [154]) as follow

$$\frac{4\pi\lambda_B\sigma_{bare}}{\kappa_{res}} = 2 \sinh\left(\frac{\psi_d}{2}\right) + 4\zeta \tanh\left(\frac{\psi_d}{4}\right). \quad (3.40)$$

At the planar limit ($\zeta = 0$) the above equation reduces to

$$\frac{4\pi\lambda_B\sigma_{plane}}{\kappa} = 2 \sinh\left(\frac{\psi_{d,plane}}{2}\right), \quad (3.41)$$

where σ_{plane} and $\psi_{d,plane}$ are the bare charge density and the diffuse potential of the plane.

A first-order Taylor development of Eq. 3.40 about ζ , with $\zeta \ll 1$, gives

$$\begin{aligned} \frac{4\pi\lambda_B\sigma_{plane}}{\kappa}(1 + A_0\zeta) &= 2 \sinh\left(\frac{\psi_{d,plane}}{2}\right) \\ &+ \zeta \left[4 \tanh\left(\frac{\psi_{d,plane}}{4}\right) + \cosh\left(\frac{\psi_{d,plane}}{2}\right) \left(\frac{\partial\psi_d}{\partial\zeta}\right)_{\zeta=0} \right], \end{aligned} \quad (3.42)$$

where $A_0 = \left(\frac{\partial\sigma_{plane}}{\partial\zeta}\right)_{\zeta=0}$, which combined with Eq. 3.41 yields

$$\frac{4\pi\lambda_B\sigma_{plane}}{\kappa_{res}}A_0 = 4 \tanh\left(\frac{\psi_{d,plane}}{4}\right) + \cosh\left(\frac{\psi_{d,plane}}{2}\right) \left(\frac{\partial\psi_d}{\partial\zeta}\right)_{\zeta=0} \quad (3.43)$$

After some algebra, one further finds

$$\begin{aligned} \frac{4\pi\lambda_B\sigma_{plane}}{\kappa}A_0 &= 4 \tanh\left(\frac{\psi_{d,plane}}{4}\right) \\ &+ \cosh\left(\frac{\psi_{d,plane}}{2}\right) \left[\frac{C\kappa\lambda_{Stern}\sigma_{d,plane}}{q_s} - \frac{1}{q_s} \left(\frac{1}{1 - \alpha_{plane}} + C\sigma_{plane} \right) A_0 \right] \end{aligned} \quad (3.44)$$

where $C = 4\pi\lambda_B\lambda_{Stern}$ is the capacitance of the Stern layer and α_{plane} is the fraction of deprotonated sites of the plane. Indeed,

$$\begin{aligned} \frac{\partial\psi_d}{\partial\zeta} &= \left(\frac{\partial F(\sigma, \zeta)}{\partial\zeta}\right)_{\sigma} + \left(\frac{\partial F(\sigma, \zeta)}{\partial\sigma}\right)_{\zeta} \left(\frac{\partial\sigma}{\partial\zeta}\right) \\ &= \frac{C\kappa\lambda_{Stern}\sigma}{q_s} - \frac{1}{q_s} \left(\frac{1}{1 - \alpha} + C\sigma \right) A, \end{aligned} \quad (3.45)$$

where

$$F(\sigma, \zeta) = \frac{1}{q_s} \left[\ln(10)(\text{pH} - \text{p}K_a) - \ln\left(\frac{\alpha}{1 - \alpha}\right) - \frac{C}{1 + \lambda_{Stern}/R} \right], \quad (3.46)$$

c.f. Eq. 3.33.

From equation 3.44 the final expression of A_0 can be found, it reads

$$A_0 = \frac{\frac{1}{\cosh^2(\psi_{d,plane}/4)} + \frac{C\sigma_{plane}\kappa\lambda_{Stern}}{2q_s \tanh(\psi_{d,plane}/2)}}{1 + \frac{1/(1 - \alpha_{plane}) + C\sigma_{plane}}{2q_s \tanh(\psi_{d,plane}/2)}}. \quad (3.47)$$

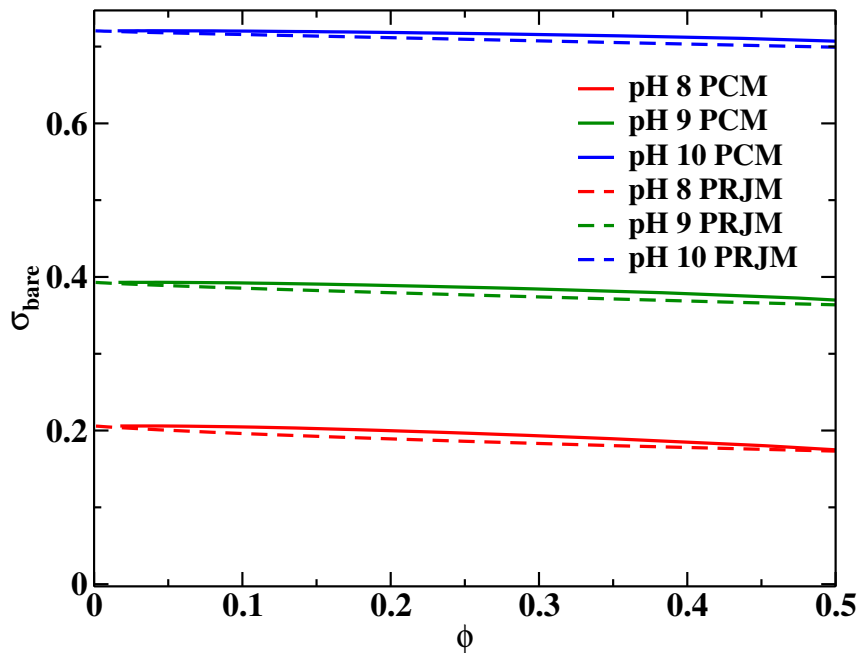


Figure 3.12: Bare surface charge density σ_{bare} versus volume fraction, ϕ , of particles of radius 8 nm in a monodisperse silica suspension at various pH calculated with the PCM (full lines), and the PRJM (dashed lines).

Bare surface charge densities for monodisperse dispersions

Figure 3.12 gives the bare surface charge density of a monodisperse silica suspension (radius 8 nm) against volume fraction at several pH, calculated with the PCM and the PRJM. As for polydisperse suspensions (see Fig. 3.2), σ_{bare} increases with pH and decreases with volume fraction. Both models give close results.

Screening in HS40 silica suspensions

Fig. 3.13 compares, in the case of HS40 silica dispersions, the relative effective inverse screening length κ^*/κ when accounting or not for the charge regulation or polydispersity. In this case of relatively low polydispersity, the screening length and, thus, the pressure is found to be unaffected by the charge regulation and only slightly by the polydispersity.

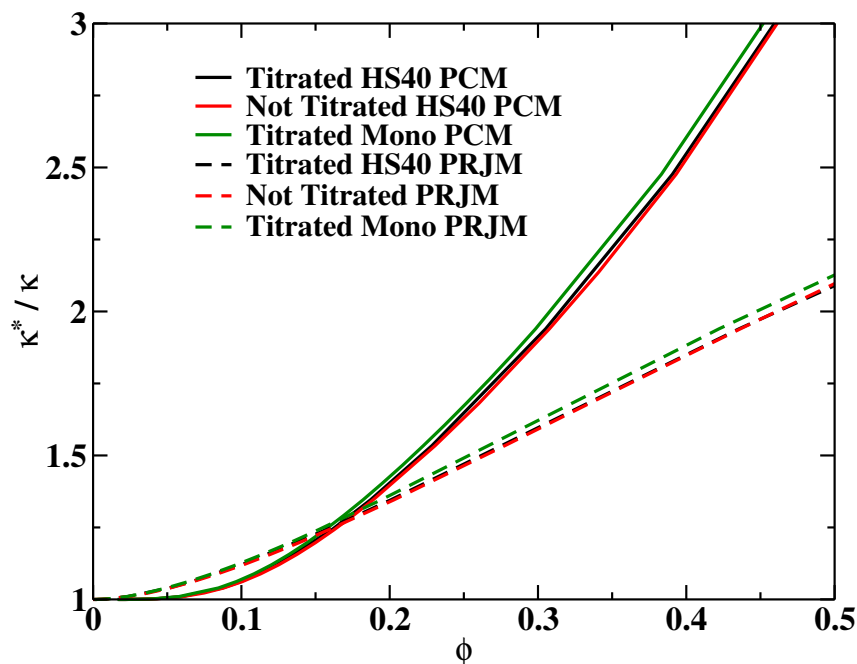


Figure 3.13: Relative effective inverse screening length, κ^*/κ , of the HS40 silica suspension in comparison with that of a monodisperse silica suspension with $R=\langle R_{\text{HS40}} \rangle$ and a non titrating colloidal suspension with the same particle distribution as the HS40. In the latter, the charge density of all particles is set equal to that of a planar silica surface in the same bulk conditions. The dispersions are in equilibrium with a bulk solution containing 5mM of 1-1 salt and at pH 9. HS40 with titration (black), HS40 without titration (red), monodisperse 8nm with titration (green). The results are computed with the PCM (full lines) and the PRJM (dashed lines).

Chapter 4

Structure and Thermodynamics of Aqueous Suspensions of Polydisperse Silica Nanoparticles: A Monte Carlo Study

In this chapter, two multi-component models (colloid only models) are constructed, based on the PCM and PRJM (see Chapter 3) and thereafter referred as MCM-CM and MCM-RJM, respectively. Monte Carlo simulations of these models are performed in the NVT and NPT ensembles which, combined to a swap move, efficiently equilibrate charged polydisperse particle suspensions up to high volume fractions. The simulation results are confronted with experimentally determined phase diagrams and equation of state for two different aqueous suspensions of polydisperse silica nanoparticles (Ludox HS40 and Ludox TM50). The MCM-CM simulations are found to predict very satisfactorily the phase compositions of the suspensions and their locations in the experimental phase diagrams. This includes but is not limited to an MgZn_2 Laves - bcc phase coexistence and a re-entrant melting phenomenon. The MCM-CM simulations predict equally well the equations of state for the two silica dispersions. The MCM-RJM simulations are found, on the contrary, to be unable to reproduce the experimental data. In good agreement with experimental observations, a glass forming liquid is predicted by the MCM-CM simulations at rather modest volume fractions. Preliminary results suggest that it is a good glass former with a rather homogeneous structure.

4.1 Introduction

Development of analytical theories and simulations has allowed considerable progress in the understanding of polydisperse hard sphere (HS) systems over the last two decades. The equation of state[166] and the solid-liquid coexistence[23, 24, 167] in binary HS mixtures have been successively obtained using a swap move which attempts to exchanging pairs of particles in combination with a Monte-Carlo thermodynamic integration scheme[168]. The latter was further used to reveal the rich phase diagram of binary hard sphere mixtures[29] of varying compositions, size ratios and densities of the binary HS. The phase diagram thus obtained explains the formation of binary superlattice structures, namely A_1B_2 and AB_{13} , observed in natural silicate opals[27], although certainly not made of pure HS, and in synthetic suspensions of near ideal HS binary systems[31], respectively. Using the same approach Dijkstra and co-workers[32, 34] more recently added two new stable superlattice structures, $MgCu_2$ and $MgZn_2$ Laves, to the theoretical binary HS phase diagram, a prediction which has only recently been confirmed experimentally by Palberg and co-workers [33] in binary systems of HS approximants. Perhaps more importantly, these associated theoretical and experimental works on HS systems (purely entropic) clearly demonstrate the counter-intuitive idea, initiated by Onsager[169] in his seminal work on the isotropic-nematic transition in a fluid of thin hard rods, that the ordering/crystallization is entropy driven[29, 170, 21, 104]. In other words, the macroscopically observed order is driven by an increase in microscopic disorder: upon crystallization the HS particles gain in free volume and, thus, in degrees of freedom.

When departing from binary systems and approaching the continuous polydisperse systems that best describe real colloidal suspensions, however, the parameter space increases accordingly and, consequently, the successful thermodynamic integration approach soon becomes impracticable. An attractive alternative is the isobaric semi-grand canonical (ISGC) ensemble developed by Kofke *et al.*[171, 172] which provides for the sampling of many realizations of the polydisperse disorder together with a direct access to the coexistence pressure. Applying the ISGC ensemble in MC simulations, Kofke and Boldhuis[47] showed that at equilibrium a fluid of arbitrary polydispersity can fractionate and allow the precipitation of a crystal of small polydispersity, invalidating the notion of terminal polydispersity asserted from experimental observations[45, 51, 117], beyond which a fluid cannot form a crystal, and questioning the putative existence of an equilibrium glass phase

at high polydispersities[173]. This was further confirmed by the theoretical work of Fasolo and Sollich[174, 36] with the aid of a moment free energy method inspired by the work of Bartlett[46, 173, 175]. They further showed that as density increases the polydisperse system fractionates into a cascade of crystalline solids (of fcc structure), a prediction later confirmed by MC simulations in the ISGC ensemble[176, 177].

In recent years, there has been an important progress in the understanding of the nucleation processes of HS systems. Brute force Brownian dynamics[75] (BD), molecular dynamics[117, 178], umbrella sampling[105, 179], forward flux sampling[178] have all been used to calculate the nucleation rate of hard spheres and nucleation Gibbs free energy. The results produced by the different methods are in very good agreement with each other[178] and agree well with experimental data[180, 181, 182] at high supersaturation. Simulations, however, underestimate experimental findings at low supersaturation by several orders of magnitude, but this may be due in part to the softness of the interactions in the experimental system[183, 75]. The predicted slowing down of the particle dynamics[117] was further shown to explain the experimentally observed minimum in and strong elapse of the induction time with increasing polydispersity and supersaturation[184, 185]. In experiments, however, the nucleation rate density was observed to be much enhanced when increasing polydispersity[184] despite a much longer induction time. This observation may be partly explained by the synergetic effect induced by the gain in mobility of the particles in the neighboring areas of forming nuclei[186, 187, 188].

Density[189] and structural fluctuations[75], with a lack of long range order, were identified in MC and BD simulations, respectively, as acting as the first step (precursors) of nucleation, and were later shown to occur simultaneously in the early stage of nucleation[190]. The identified structural heterogeneity was further found to be closely coupled to dynamical heterogeneity[191], even beyond the mode-coupling glass transition, suggesting an intimate link between nucleation and vitrification[192, 193]. The dynamic and structural correlation was confirmed experimentally[194, 195] and was further elaborated as a potential proof for the thermodynamic nature of the glass transition[196, 197, 198]. The observed correlation could, however, equally well be remanent from a kinetically hindered nucleation stuck in the prenucleation process[194, 195, 50]. Interestingly, the recent simulation results of Coslovich *et al.* [199] on large polydisperse HS systems show an appreciable increase in local geometric order only at large packing fractions where

the system is eventually found to crystallize (AlB_2 symmetry).

Further improvement in the understanding of the glass transition of polydisperse HS systems and soft sphere systems was also achieved by rediscovering the simple but very efficient MC swap move[166, 23] that dramatically accelerates the equilibrium sampling of configuration space[54, 200, 201]. Application of such an MC algorithm has allowed the thermalization of supercooled liquids of polydisperse HS beyond the random close packing limit showing that the jamming transition cannot be the end point of the fluid branch[202] and opening up a path to the study of the Gardner transition[203, 119] marked by the rapid increase in spatial correlation lengths[198] and relaxation time scales. The sharp and continuous drop in the configurational entropy observed by Kauzmann in several glass forming liquids [204] was confirmed beyond the experimental glass transition[205].

On the other hand, particles with soft interactions, whether due to charged surfaces or grafted polymers, present marked differences, despite generic similarities, with their HS counterparts. In general, binary mixtures of soft particles show a much richer phase diagram than those of HS, as inferred from both experiments[103, 206, 207, 208] and simulations[209, 210, 211, 212]. The interaction softness has been found to facilitate the thermalization of colloidal suspensions, due to the gain in free volume/mobility of the colloids[213, 214]. As an example, the addition of small amounts of non-adsorbing polymer, turning pure HS into attractive HS by depletion, can lead to a devitrification of polydisperse HS suspensions[215, 216, 217]. Similarly, in computer simulations, suspensions of soft particles with high polydispersities and Kob-Andersen Lennard Jones mixture used as model glass-formers irremediably crystallize beyond the mode-coupling glass transition[53, 218, 219, 220]. This renders difficult the disentanglement between the different dynamic and thermodynamic scenarios of the glass transition[220], but further confirms the non-validity of the notion of terminal polydispersity. Experimentally, particles with very soft interactions, e.g. star polymers and microgels, are observed to crystallize up to very high polydispersities[221, 222, 223]. At high densities, they become good glass formers and their dynamics near the glass transition, characterized by the large scale cooperative motion of particles and the disappearance of hopping dynamics, is found to agree well with mean-field phenomenology as described by the mode coupling theory[224, 225, 219, 226], at least much better than any other model glass formers. Despite these recent advances, our general understanding of neutral soft particle dispersions

remains to a large extent qualitative due to a lack of systematic comparison between simulations and experimental model systems and to the weaknesses of the effective pair potential (w^*) used in the simulations, which for example, does not take into account its dependence on the particle density[223] as due to many-body interactions.

The realization of this density dependence of w^* has been a key achievement in the understanding of nearly monodisperse suspensions of charged particles (CS). There, w^* has been shown to be accurately captured by a hard core Yukawa (HCY) pair potential as long as an effective charge and screening length calculated with an appropriate rescaling procedure are used[65, 160, 100]. The static structure factor of the liquid-like ordered state of CS suspensions is well reproduced by theories [227, 228, 229] and simulations. The phase diagrams are known from computer simulations for HCY[230] and point Yukawa[44, 38, 231, 232] particles in both the constant charge and constant potential conditions[132]. In general, they are found to agree closely with experimental phase diagrams[37, 233, 234]. CS are observed to crystallize very rapidly compared to HS[235, 236, 237, 238]. This behavior agrees well with the umbrella sampling simulations of Auer[239] and is explained by the reduction in the crystal/melt interfacial free energy with the increase in the range of the electrostatic repulsion (potential softness). The electrostatic interactions are predicted to favor a two-step nucleation process through a metastable, mainly bcc nucleus even in the fcc stable region of the phase diagram[239, 240], in good agreement with experimental observations[241]. Furthermore, the long predicted Wigner glass[44, 242, 243] was recently observed with nearly monodisperse CS in salt free conditions at very low volume fractions ($< 0.01\%$)[244].

Due to their higher complexity, much less is known, however, about multimodal and polydisperse suspensions of CS. Only a limited number of experimental and theoretical studies exist for model multimodal suspensions and even fewer for polydisperse CS suspensions.

A complex multistep nucleation process to superlattice CS crystals in bidisperse CS suspension has been observed[245] and remains for the moment out of reach of theoretical work. In contrast to umbrella sampling predictions made on polydisperse HS systems[105], a decreased of the reduced interfacial free energy between the bcc crystal and the coexisting equilibrium fluid was observed by Palberg *et al.* in CS suspensions with increasing polydispersity[50]. This also remains unexplored by simulations. In general,

binary mixtures of CS reveal a far better miscibility than HS.[118] Their phase diagram has been studied mainly under low salt conditions and shows large regions of substitutional bcc alloys. Eutectic, azeotropic[246, 39, 247] and spindle type phase diagrams are also observed[248]. The characteristic size ratios of the different types of phase diagram are, however, considerably lower than those predicted and observed for HS. Experimental studies on highly polydisperse CS suspensions are very limited. Cabane *et al.* observed the formation of a Laves phase in coexistence with a bcc and liquid phase[8] in highly polydisperse suspensions of highly charged silica nanoparticles. The colloid crystals are further observed to melt into a disordered solid upon compression[7]. Kiatkirakajorn studied the phase diagram of a slightly less polydisperse suspension of silica nanoparticles in the ionic strength – volume fraction plane [9]. The typical bcc and fcc crystalline phases of the monodisperse case are observed but in a reversed order. That is, as the colloid density increases, first a fluid to fcc phase transition is observed, followed by an fcc to bcc phase transition[9]. In addition, the fcc and bcc phases are often observed to coexist with an hcp phase. Upon further compression, the colloidal crystals are also found to melt into a disordered solid.

Different theories have been proposed to reproduce the liquid-like ordered state of polydisperse CS suspensions with various levels of success[102, 249, 250]. Monte Carlo (MC) simulations revealed a crystal to glass transition in systems of polydisperse charged colloids interacting through an HCY pair potential[251, 252, 253, 254, 106]. Similarly, both terminal polydispersity and re-entrant melting were found in HCY systems with quenched size polydispersity using free energy calculations[255]. The phase diagrams of binary mixtures of equally and oppositely charged colloids were calculated by simulations and approximate theory[256, 34, 41, 257]. Finally, a lattice MC simulation in the Gibbs ensemble was employed to rationalize the liquid/bcc/Laves phase coexistence[8, 258] in highly polydisperse suspensions of CS observed by Cabane *et al.*[8]. Despite this progress, our understanding of the effects of polydispersity on the crystallization, phase diagram and glass transition of polydisperse CS suspensions is limited. The main reason being again, the lack of a well accepted method/tool which relates the charge polydispersity to the size polydispersity and which thus provides an accurate description of the interaction polydispersity[259, 250, 248]. Recently, several theoretical methods have been developed to solve this issue[101, 125, 126]. None of them, however, have been tested on polydisperse

systems.

In the present chapter, we study the reliability of two previously developed methods (see Chapter 3) to compute the distribution of the HCY pair potentials and associated MC simulations of the so defined multi-component model (MCM) simulations to predict the phases observed in two different polydisperse suspensions of charged silica nanoparticles[8, 9]. The first method used to compute the distribution of the HCY pair potentials is based on the polydisperse cell model initially proposed by Torres *et al.*[101], hereafter referred as MCM-CM. The second is based on a generalization of the jellium model, hereafter named MCM-RJM. They are both extended to account for the titration and regulation of the particle surface charge. The MCM simulations are performed with an in-house code in the canonical (NVT) and isothermal isobaric (NPT) ensembles using swap moves and a well optimized cell decomposition. The simulations optimized in this way allow us to thermalize polydisperse CS systems to very high densities ($\approx 50\%$) and to reach a proper equilibrium with up to 257 600 particles. In general, very good agreement with the experiments is found including the transition to the glass forming liquid.

4.2 Methods

4.2.1 Model and Simulations

The polydisperse HS40 and TM50 silica nanoparticles are described by a MCM of the colloids only. These latter are modeled by hard spheres bearing a uniform charge density. Each colloid component is signified by a specific radius, R , and renormalized charge number, Z^* . The colloids interact through a combination of a hard core and a Yukawa potential. The pair potential between two colloids i and j separated by distance r then reads

$$\beta u_{ij}^*(r) = \begin{cases} +\infty & \text{if } r \leq R_i + R_j \\ \lambda_B \frac{Z_i^* Z_j^*}{(1+\kappa^* R_i)(1+\kappa^* R_j)} \frac{\exp(-\kappa^* r)}{r} & \text{if } r > R_i + R_j, \end{cases} \quad (4.1)$$

where $\beta = \frac{1}{k_B T}$, with k_B the Boltzmann constant, T the temperature set to 300 K and λ_B is the Bjerrum length set to 0.7105 nm. κ^* is the renormalized inverse screening length. In practice, the bare charge of a titrating silica particle depends on its size as well as the pH and ionic strength of the equilibrium solution but also on the magnitude of the interactions felt. The silica dispersions thus display both a size and a charge polydispersity,

the latter being dependent on the equilibrium conditions. In addition, the interactions between the colloids can be described by the HCY potential, Eq. 4.1, provided the charges and the inverse screening length are properly renormalized [65, 100]. In this case, the density dependent renormalized charges and κ^* are calculated within the framework of the polydisperse Poisson-Boltzmann cell model (PCM) and the polydisperse renormalized jellium model (PRJM). The two models further account for the charge regulation (pH, density and ionic strength) of the silica particles via a one-pK-Stern model adjusted on independent experimental data. The details of the models are described in the previous chapter.

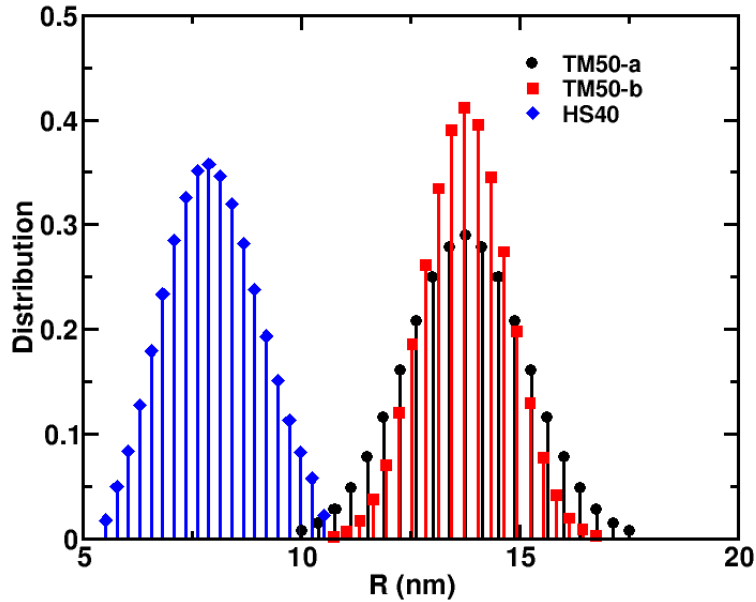


Figure 4.1: Size distributions used in the simulations for the HS40 and TM50 silica nanoparticle dispersions. See text for more details.

The size distributions of the industrially produced HS40 and TM50 silica nanoparticle dispersions were obtained from a fit of the form factor as obtained from SAXS measurements in very diluted conditions, see Ref. [8, 9], and were set accordingly in the models. A truncated Gamma distribution with a mean particle radius (\bar{R}) of 8 nm and a polydispersity of 14% was used for the HS40 dispersion. In the case of the TM50 dispersion, a Gaussian function with $\bar{R} = 13.75$ nm and a polydispersity of 10% was used, hereafter referred as TM50-a. A model with a smaller polydispersity of 7% was also considered for the TM50 dispersion, hereafter named TM50-b. Note that the polydispersity is conven-

tionally defined as the standard deviation in units of \bar{R} , (σ_R/\bar{R}) . The size distributions were discretized into 20 families whose radii vary linearly between $5.5 \text{ nm} \leq R \leq 10.5 \text{ nm}$, $10 \text{ nm} \leq R \leq 17.5 \text{ nm}$, $10.725 \text{ nm} \leq R \leq 16.725 \text{ nm}$ for the HS40, TM50-a and TM50-b models, respectively. The model size distributions are given in Figure 4.1.

The polydisperse colloidal models described above were solved employing MC simulations in the canonical and isobaric ensembles with use of the Metropolis algorithm[260]. In addition to the usual translation move, swap moves between pairs of randomly selected particles were also employed. The probability of swap moves was set to 0.3. All the simulations were carried out in a cubic box with periodic boundary conditions and the minimum image convention. The number of particles, N was always larger than 4000. Typically, the simulations were performed with $N = 4025$ particles and repeated with $N = 20025$ to test for the system size convergence. For some of them N was also increased to 32200 and 257600.

A spherical cutoff of radius r_c was applied to the pair potential. r_c was set according to the interactions between the largest particles such that $\beta u(r_c) \leq 0.1$. A tail correction was applied to the total calculated energy. Simulations were further accelerated with the use of a cell decomposition[52].

Equilibration of the internal energy of the polydisperse dispersions in the solid states often necessitated several million MC cycles (a cycle consists of N attempted MC moves). Production runs lasted for 10^5 MC cycles.

4.2.2 Effective structure factor

Experimentally, the structure of a colloidal dispersion is generally assessed by small angle scattering of X-rays (SAXS) or of neutrons (SANS) or by static light scattering (SLS). The structure of the TM50 and HS40 silica dispersions of interest here was studied using SAXS by Cabane, Goehring *et al.*[8, 9]. The measured SAXS intensity can be written as the product of the form and structure factor, $I(q) = P(q)S(q)$. $P(q)$ is essentially a function of the shape and size distribution of the particles while $S(q)$ is a function of the spatial distribution of the particles, i.e. the structure of the particle dispersion. $P(q)$ is measured in very diluted conditions where $S(q) \approx 1$ which then facilitates the determination of $S(q)$ at any ϕ . It should be noted that the decomposition of $I(q)$ into $P(q)$ and $S(q)$ is strictly valid when no particle fraction occurs. Should this not be the case, only an *effective* $S(q)$

can be extracted from $I(q)$. Nonetheless, such measured $S_{eff}(q)$ can still be compared with simulations. From a theoretical point of view[261], one can write $S_{eff}(q)$ as

$$S_{eff}(q) = \frac{\sum_{i,j=1}^{n_C} F_i(q)F_j(q)v_i v_j \sqrt{\rho_i \rho_j} S_{ij}(q)}{\sum_{i=1}^{n_C} [F_i(q)v_i]^2 \rho_i}. \quad (4.2)$$

with n_C the number of colloidal families, v_i the volume of colloids of type i , $F_i(q) = 3 \left[\frac{\sin qR_i - qR_i \cos qR_i}{(qR_i)^3} \right]$, ρ_i the numeric density of colloids of type i , and

$$S_{ij} = \delta_{ij} + \sqrt{\rho_i \rho_j} \int_0^\infty dr 4\pi r^2 \frac{\sin qr}{qr} [g_{ij}(r) - 1], \quad (4.3)$$

where $g_{ij}(r)$ is the radial distribution function between colloids of types i and j , and δ_{ij} the Kronecker delta. $g_{ij}(r)$ is defined as

$$g_{ij}(r) = \frac{V}{4\pi r^2 N_{ij}} \frac{dn_{ij}(r)}{dr}, \quad (4.4)$$

where $n_{ij}(r)$ is the average number of pairs (i, j) separated by a distance inferior to r , N_{ij} is the total number of pairs (i, j) and V is the total volume of the box.

4.2.3 Local bond-order parameters

In simulations, the structure of solids that may be formed and their distinction is most easily assessed by the mean of local bond-order parameters which are a measure of the structure of the neighbors of a particle. Their construction[69, 70] begins from the definition of a $(2l+1)$ dimensional complex vector with the component,

$$q_{lm}(i) = \frac{1}{N_b(i)} \sum_{j=1}^{N_b(i)} Y_{lm}(\mathbf{r}_{ij}) \quad (4.5)$$

where the the sum goes over all the $N_b(i)$ neighbors of particle i . Generally, one uses only the nearest neighbors in the calculation of $q_{lm}(i)$, the maximum separation between i and its neighbors is defined by the first peak in the $g(r)$. m is an integer that runs from $-l$ and $+l$, $Y_{lm}(\mathbf{r}_{ij})$ are spherical harmonics and \mathbf{r}_{ij} is the position vector from particle i to particle j . The rotationally invariant local bond-order parameters are then defined by,

$$q_l(i) = \sqrt{\frac{4\pi}{2l+1} \sum_{m=-l}^l |q_{lm}(i)|^2} \quad (4.6)$$

The typical q_4 - q_6 map calculated by Monte Carlo simulations for the HCY particle system in five different crystalline structures and in the fluid phase is given in Figure

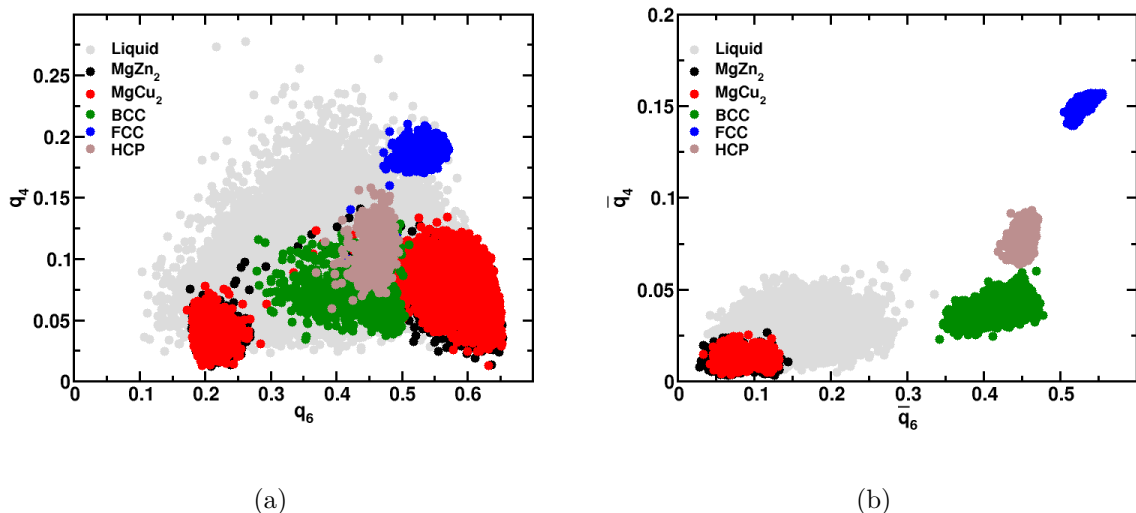


Figure 4.2: Bond order parameters maps from Monte Carlo simulations of HCY particles in different crystalline phases (bcc, hcp, fcc, MgCu₂ Laves and MgZn₂ Laves) and in the fluid phase. More details on the simulations are provided in the text.

4.2(a). The figure illustrates that the q_4 - q_6 region of the fluid completely overlaps with those of the crystalline phases. However, the two Laves phases considered here are characterized by two q_4 - q_6 regions well separated by distinct q_6 values, a property that we will use to identify them. The low and high q_6 regions are the signature of the particles in the octahedral and tetragonal sites of the Laves, respectively.

The mean local bond order parameters, \bar{q}_4 and \bar{q}_6 introduced by Lechner *et al.*[262] will be used, instead, to distinguish the bcc, hcp and fcc phases as well as the bcc, hcp and fcc crystalline phases from the fluid phase. The \bar{q}_4 - \bar{q}_6 regions of these phases are indeed well separated, see Figure 4.2(b). They are defined as

$$\bar{q}_l(i) = \sqrt{\frac{4\pi}{2l+1} \sum_{m=-l}^l |\bar{q}_{lm}(i)|^2} \quad (4.7)$$

with

$$\bar{q}_{lm}(i) = \frac{1}{\bar{N}_b(i)} \sum_{j=1}^{\bar{N}_b(i)} q_{lm}(j) \quad (4.8)$$

where the sum from $j = 0$ to $\bar{N}_b(i)$ runs over all neighbors of particle i plus the particle i itself.

The AB₂ phase, however, is still not well separated from the fluid phase. To do so, the following algorithm was used:

- 1- Preselect all the particles A with $q_6 < q_6^{max}(A)$ and $\bar{q}_6 > \bar{q}_6^{min}(A)$

2- Preselect all the particles B with $q_6 > q_6^{min}(B)$ and $\bar{q}_6 < \bar{q}_6^{max}(B)$

3- Keep only the preselected particles A with a number of neighboring particles B , n_{vois} , such that $10 < n_{vois} < 13$. Neighbors are defined as all particles B that are within the radius r_{cut} around a particle A .

4- Reject all particles B not neighbors of a particle A .

The following set of parameters was found to provide reliable results, $q_6^{max}(A) = 0.27$, $q_6^{min}(B) = 0.35$ and $\bar{q}_6^{max}(B) = \bar{q}_6^{min}(A) = 0.092$. r_{cut} was set equal to the minimum in the mean $g(r)$ just after the first peak.

4.3 Results

4.3.1 HS40 silica suspensions

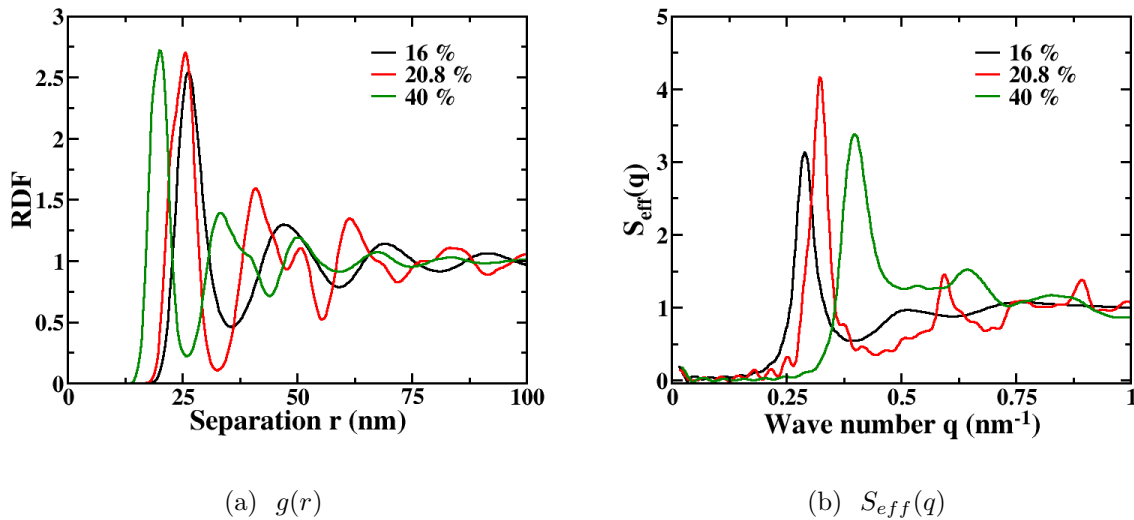


Figure 4.3: Radial distribution function ($g(r)$, a) and effective structure factor ($S_{eff}(q)$, b) at volume fractions 16% (black), 20.8% (red), 40% (green) as predicted from MC simulations of the MCM-CM at pH 9. The MC simulations are performed with 4025 particles. The bulk electrolyte solution contains a 1-1 salt at a ionic strength of 5 mM.

In what follows, we present and discuss two representative quantities which characterize the structure of the silica HS40 suspensions and which are easily accessible experimentally. In Fig. 4.3(a) we show the density evolution of the pair distribution function $g(r)$, at constant pH (pH=9), as predicted from the MC simulations of the MCM-CM. As expected, with the increase in the particle volume fraction, the particles get closer and

the first peak of the $g(r)$ shifts toward lower separation values. This monotonic shift in $g(r)$ is accompanied by a non-monotonic evolution of the peak height. The same trend as in $g(r)$ is observed in the effective structure factor, Fig. 4.3(b). With the increase in the volume fraction, the position of the first peak, $(S_{eff}^{max}(\phi), q^{max}(\phi))$, shifts to larger q values, i.e. smaller r . Simultaneously, $S_{eff}^{max}(\phi)$ exhibits a non-monotonic variation. The $g(r)$ and $S_{eff}(q)$ of the dispersion are characteristic of a liquid-like ordered state at $\phi = 16\%$, whereas at $\phi = 20.8\%$, they are the signature of a crystal-like ordered state with the appearance of distinct and narrow peaks in the $S(q)$ and secondary oscillations in the $g(r)$. The crystal structure will be detailed later, but as an immediate remark and as is illustrated below, we would like to stress here that the overall “quality” (peak resolution and magnitude) of the $g(r)$ and $S(q)$ curves in the crystal-like ordered state is very system size dependent.

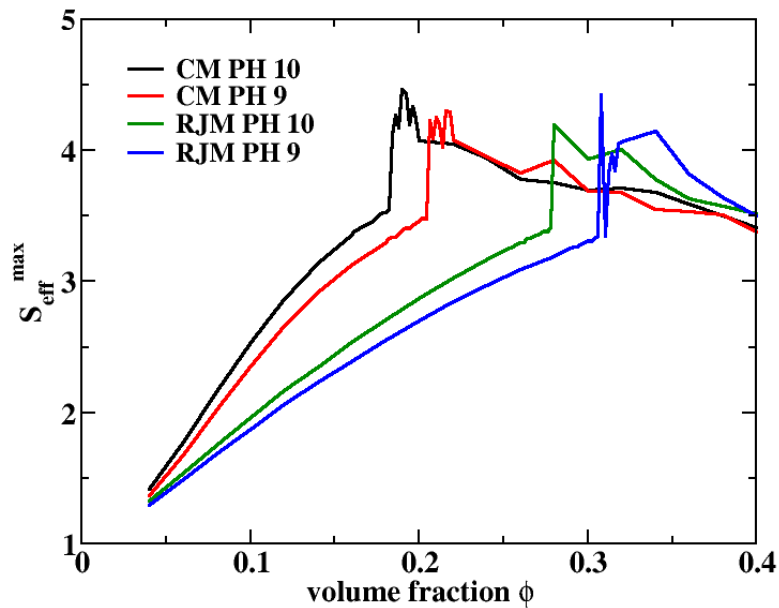


Figure 4.4: Maximum of the effective structure factor (S_{eff}^{max}) versus volume fraction ϕ as predicted from MC simulations of the MCM-CM at pH 10 (black) and pH 9 (red) and from the MCM-RJM at pH 10 (green) and pH 9 (blue). Simulations were performed with 4025 particles. The bulk electrolyte solution contained a 1-1 salt at an ionic strength of 5 mM.

The magnitude of S_{eff}^{max} , known to reflect the level of structuring in the material is plotted in Figure 4.4 as a function of the volume fraction at pH values of 9 and 10. S_{eff}^{max} values as predicted from simulations of the MCM in both the PCM and RJM

approximations are reported for comparison. Whatever the model and pH the same general behavior is noted. S_{eff}^{max} is seen to first increase progressively with ϕ , this increase is followed by a discontinuity characterized by a very steep increase, at a position which depends on the pH and model. Finally, upon further increase in ϕ , S_{eff}^{max} is found to drop continuously. The discontinuity in S_{eff}^{max} strongly suggests a first order fluid to solid transition while the following drop indicates a slow and continuous transition to a glass forming liquid as can also be inferred from the broadening of the peaks in the $S_{eff}(q)$ and the almost liquid-like character of the $g(r)$ curve at $\phi = 40\%$ seen in Fig. 4.3. These results are in full agreement with the experimental observations on HS40 silica dispersions at equilibrium[8] and under rapid drying[7] conditions. As expected, when increasing the repulsive interactions between the silica particles, i.e. when increasing the pH from 9 to 10, the fluid to solid transition is found to occur at lower ϕ . This also explains the quantitative difference between the MCM-CM and the MCM-RJM. As we have previously shown, see Chapter 3, the MCM-RJM results in weaker interparticle interactions and lower osmotic pressures than its CM counterpart. The questions raised are thus (i) which of the two models gives the best description of the experimental data? and (ii) are either of the two MCM models used in the simple but pragmatic MC simulation method employed here able to predict qualitatively and quantitatively the colloid crystals observed experimentally?

To answer these questions we now compare the experimental and simulated S_{eff}^{max} . Fig. 4.5 compares several experimental $S_{eff}(q)$ in the fluid and glass forming liquid regions with those predicted by the simulations within the two MCM approximations. As can be seen the MCM-CM provides a much better description of the $S_{eff}(q)$ than the MCM-RJM. Although not perfect, very good agreement between the experimental and simulated $S_{eff}(q)$ is obtained when the MCM-CM is used, especially given the model approximations and the experimental uncertainties concerning particle size distribution, particle volume fraction and the normalization procedure to extract the experimental $S_{eff}(q)$.

This becomes even clearer when one compares the measured $S_{eff}(q)$ close to the fluid to solid transition, $\phi = 21\%$, with that predicted from the MCM-CM simulations of a large system composed of more than 250 000 particles, see Figure 4.6(a). The predicted curve obtained using the MCM-RJM is also shown for comparison. These results confirm that the MCM-RJM fails to describe accurately the interparticle interactions of polydisperse suspensions of charged colloids at a finite electrolyte concentration. It should be recalled

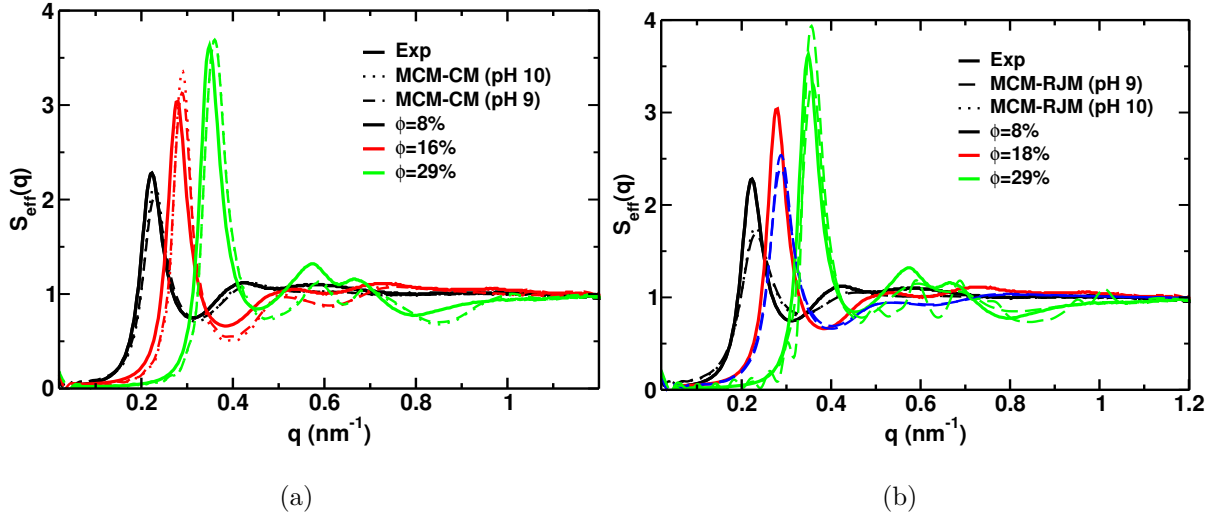


Figure 4.5: Experimental (solid lines) and simulated (dashed lines) effective structure factor $S_{eff}(q)$ at three particle volume fractions (from left to right): 8%, 16%, 29%. The simulation predictions are obtained using the MCM derived from both the (a) PCM and (b) PRJM approximations. Simulations are performed with 4025 particles in the same equilibrium conditions as in the experiments, that is pH 9 and a bulk ionic strength of 5 mM. The simulation curves at pH 10 are also plotted for comparison (dotted lines).

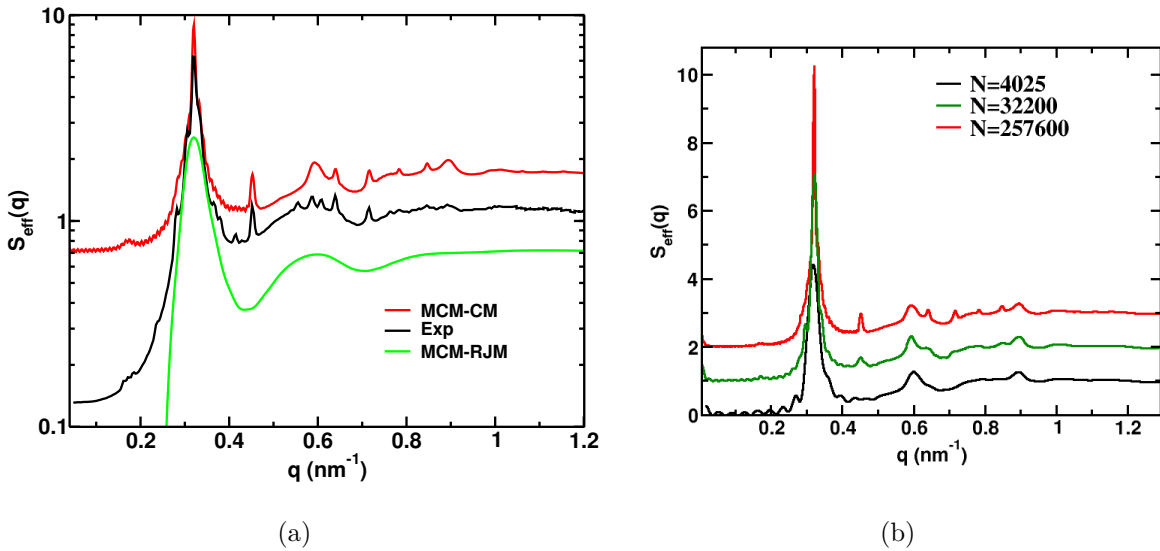


Figure 4.6: Effective structure factor $S_{eff}(q)$ of the HS40 silica dispersion at $\phi = 21\%$ in equilibrium with a bulk solution at pH 9 and a ionic strength of 5 mM. The curves are shifted along the y-axis for clarity (a) Experimentally determined S_{eff} , Exp, in comparison with the predictions of the MCM simulations as obtained within the MCM-CM, and MCM-RJM, approximations. (b) System size dependence of S_{eff} as obtained from the MCM simulations within the PCM approximation.

here that the simulations are essentially parameter free and use only experimentally accessible variables as inputs, namely the measured pH, ionic strength and size distribution. The simulations of the MCM-CM, on the other hand, provide an impressive description of the effective structure factor of the HS40 silica dispersion. In particular, the simulations successfully predict the coexistence of a bcc phase with a Laves AB_2 phase. Indeed, the characteristic (110) (200) (211) (220) (311) peak positions of the bcc crystal phase are very well reproduced. In addition to the bcc peak, many sharp peaks can also be seen, their positions again in very good agreement with the experimental $S_{eff}(q)$. Their positions and relative intensities have been identified as those of crystals of a Laves $MgZn_2$ phase with a compact hexagonal ($P6_3/mmc$) symmetry, see Ref. [8]. Unfortunately, despite the large number of colloids employed in the simulation ($N > 250000$), the system size is still too small to reveal all the characteristic peaks of the Laves $MgZn_2$ phase seen in the SAXS $S_{eff}(q)$, in particular but not only, the triplet at low q values.

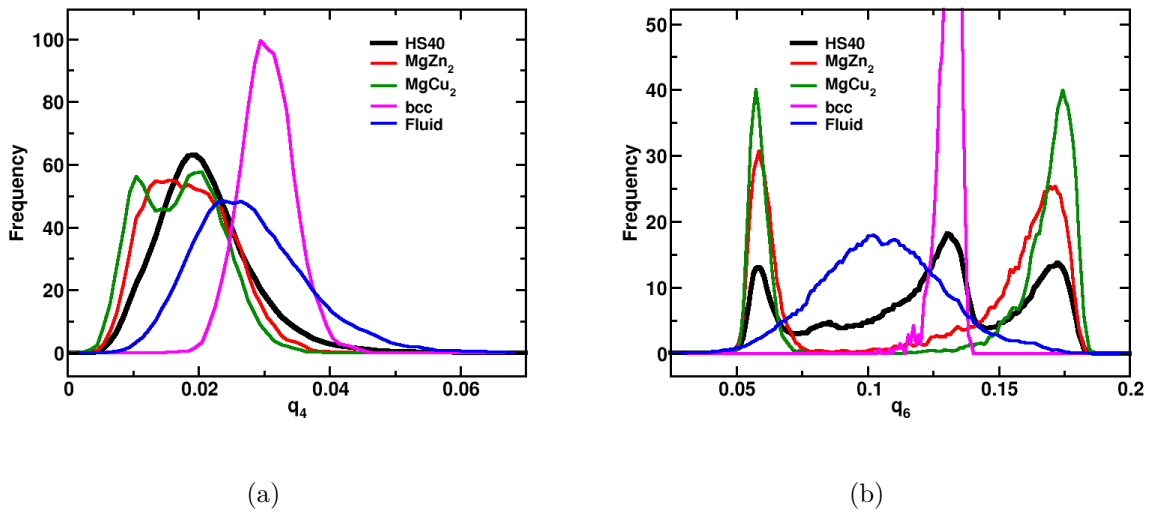


Figure 4.7: Bond order parameters of the HS40 silica dispersion in comparison with that of “ideal” crystalline bcc, $MgZn_2$ Laves and $MgCu_2$ Laves phases as well as of the fluid phase. The simulation conditions are the same as in Fig. 4.9 except for the fluid phase for which ϕ was set to 18%. (a) q_4 (b) q_6 . The “ideal” AB_2 phases were constructed from the known crystallographic structures using a binary distribution of charged particles with radii 7.3 and 9.3 nm for the small (B) and large (A) particles in the tetragonal and octahedral sites, respectively. The “ideal” bcc phase was constructed in the same manner but with monodisperse particles of radius 8 nm. The bond order parameters of these ideal phases were obtained after their thermalization.

Although $S_{eff}(q)$ or $I(q)$ are *natural* quantities to compare with experiments, a much more appropriate choice to recognize and identify the crystalline phases in a simulation is the use of a combination of bond-order parameters based on spherical harmonics, see e.g. Ref. [263]. The latter are calculated at the level of individual particles and are sensitive to the relative positions of their first neighbors. They typically distinguish particles with a liquid-like or a crystal-like order. A careful analysis further specifies the type of crystalline phase. For these reasons, local bond order parameters have been extensively employed in the literature to distinguish between the solid phases of the bcc, fcc and hcp crystal-like order. The case of the Laves phases turns out to be more complicated, as their typical bond order parameters are confounded with those of the fluid phase, see e.g. Figures 4.2 and 4.7. The typical distributions of the q_6 and q_4 bond order parameters of the Laves phases, along with those of the fluid phase and bcc phase are shown in Fig. 4.7. The Laves q_6 and q_4 completely overlap with those of the liquid. Nevertheless, the AB_2 q_6 distribution is bimodal. The first peak, on the left, results from the large particle in the octahedral sites (A), while the second is due to the small particles in the tetragonal sites (B). The particles belonging to the Laves phase can be suitably filtered out from the fluid phase by taking advantage of this property along with the distinct and characteristic coordination number of the particles within the octahedral and tetragonal sites, see Sect. 4.2 for more details. In all cases, the trimodal q_6 distribution of the HS40 silica dispersion at $\phi = 21\%$ confirms the coexistence of a bcc and AB_2 phase.

Another difficulty, is the very close proximity of the hexagonal and cubic variant of the Laves phases, that is the compact hexagonal ($P6_3/mmc$) $MgZn_2$ and compact cubic (Fd_3m) $MgCu_2$ structures, in terms of both structure and energy, which makes them hard to distinguish. A consequence is the very subtle difference between the two Laves phases in the q_4 and q_6 distributions, as seen in Fig. 4.7. This is also clearly illustrated in Fig. 4.8(a) where the mean radial distribution functions between the large particles in the octahedral sites of the pure and thermalized $MgZn_2$ and $MgCu_2$ Laves phases are compared. That of the simulated HS40 silica suspension is also shown. Differences in the $g(r)$ between the two Laves phases appear only from the third neighbors and qualitative change only from the fourth neighbors. The distributions of the bond order parameters for the two Laves phases calculated with the third and fourth neighbors still show substantial overlap, as illustrated in Figure 4.8(b) for q_4 . In any case, all these quantities confirm the

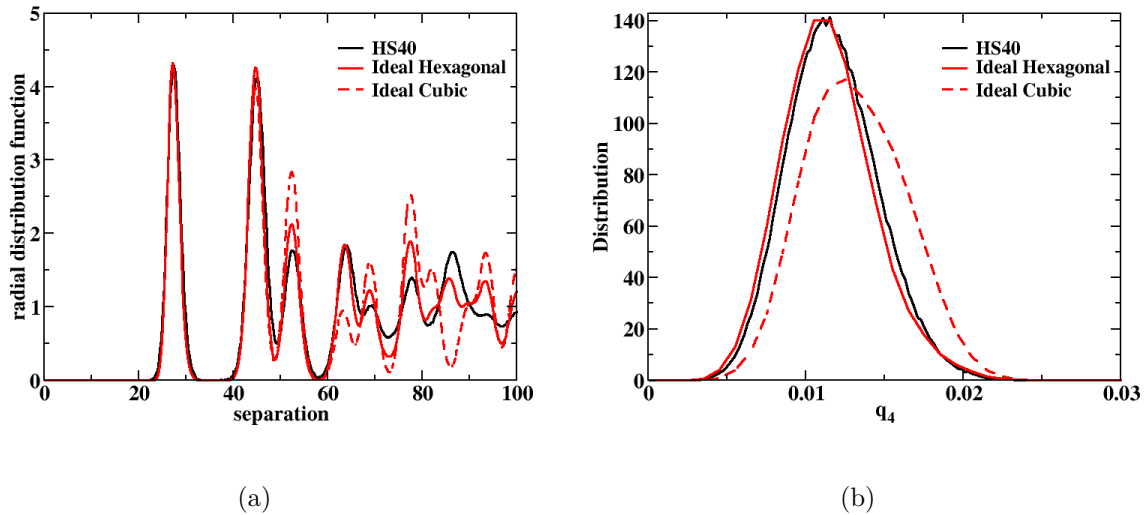


Figure 4.8: (a) Simulated radial distribution function between the particles in the octahedral sites (large particles) of the “ideal” Laves MgCu_2 (full red line) and MgZn_2 (dashed red line) phases in comparison with that of the HS40 silica dispersion (full black line). All the simulations are performed with the MCM-CM with 4025 colloidal particles at $\phi = 20.8\%$ in equilibrium with a bulk solution at pH 9 and a ionic strength of 5 mM. The “ideal” AB_2 phases were constructed from the known crystallographic structures using a binary distribution of charged particles with radii 7.3 and 9.3 nm for the small (B) and large (A) particles in the tetragonal and octahedral sites, respectively. (b) q_4 distribution calculated with the third and fourth neighbors for the “ideal” Laves MgZn_2 and MgCu_2 phases in comparison with that of the Laves phase formed in the simulated HS40 silica dispersion. The simulation conditions are the same as above.

formation of a Laves phase of compact hexagonal structure (MgZn_2) in the model HS40 silica dispersion, in good agreement with the experiments.

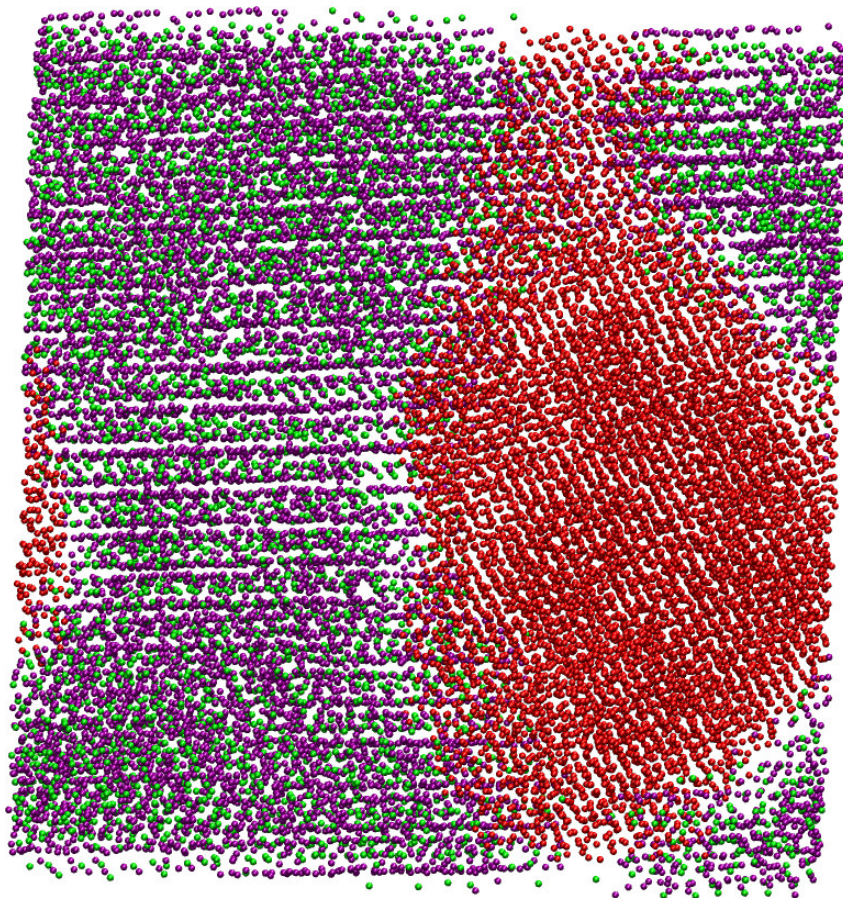


Figure 4.9: Snapshot of the simulated HS40 silica dispersion at $\phi = 21\%$ in equilibrium with a bulk solution at pH 9 and an ionic strength of 5 mM. The simulations were performed with the MCM-CM. The number of colloidal particles is set at $N = 257600$. The colors of the particles are set according to their crystalline order. That is, the particles in the bcc crystal-like order are colored in red and the particles in the octahedral and tetragonal sites of the MgZn_2 phase are represented in green and purple, respectively. For clarity, the liquid-like ordered particles are not represented. Note that these latter are principally found at the interfaces between the crystallites.

The simulation snapshot at $\phi = 21\%$ represented in Fig. 4.9 makes use of the particle filtering tools described above. A large and almost spherical bcc crystal is found to coexist with a polycrystalline MgZn_2 phase. The simulation box is devoided of large pockets of liquid-like ordered particles, the latter being found only in the interfacial regions between the crystals. This constitutes one of the major differences with the experiments, as indi-

cated in Fig. 4.5 by the oscillating background in the experimental $S_{eff}(q)$. However, the Laves phase was observed in experiments to grow very slowly and could only be detected after several days of equilibration. The experimental samples might not be in their final equilibrium state.

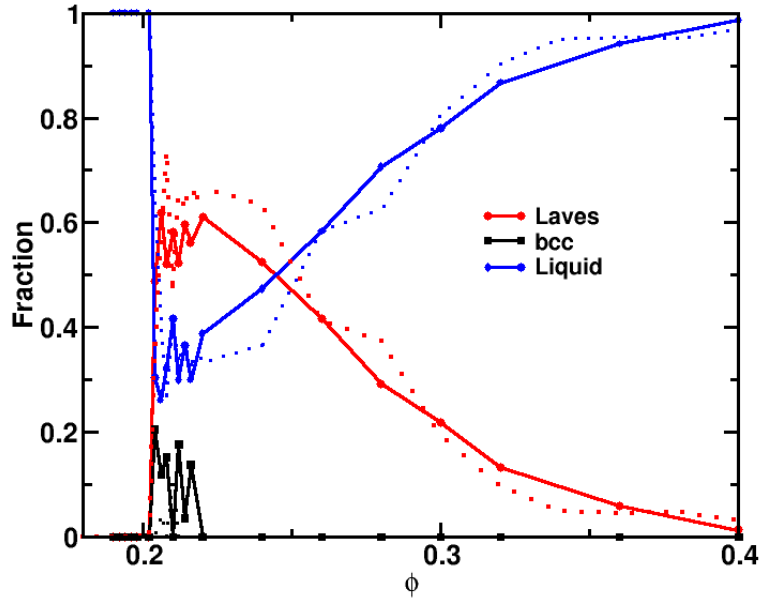


Figure 4.10: Simulated relative fractions of particles in liquid-like (blue) or bcc (black) or MgZn_2 Laves (red) crystal-like order in the HS40 silica dispersion as a function of the particle volume fraction. The simulations were performed in the MCM-CM approximation at two different system sizes, $N = 20125$ (solid lines) and $N = 4025$ (dotted lines).

Figure 4.10 presents the evolution with the particle volume fraction of the phase composition of the HS40 silica dispersion as predicted by the MCM-CM simulations for two different system sizes ($N = 4025$ and $N = 20\,125$). Interestingly, the fluid to solid phase transition is found to depend only weakly on the system size, indicating that the interface free energy between the Laves phase and the fluid is rather small. This may also explain why the Laves phase is always found to form first in the course of the simulation. On the other hand, the formation of the bcc phase is found to depend on both the system size and the configuration of the polycrystalline state of the MgZn_2 phase as indicated by the rather large fluctuations in the bcc content of the simulated systems. The simulation range of particle volume fractions of $0.20 < \phi < 0.22$ for the bcc-Laves coexistence corresponds well to the experimental range of $0.21 < \phi < 0.24$ [8]. Contrary

to the simulation predictions, however, the formation of a bcc phase alone in coexistence with a liquid phase was also observed in a small region of ϕ , $0.18 < \phi < 0.21$, preceding that of the bcc-Laves phase coexistence[8]. This discrepancy could be due to a free energy barrier between the solid bcc phase and fluid phase too large for the nucleation to occur in the simulations or, as will be seen later, to the use of a slightly too large polydispersity.

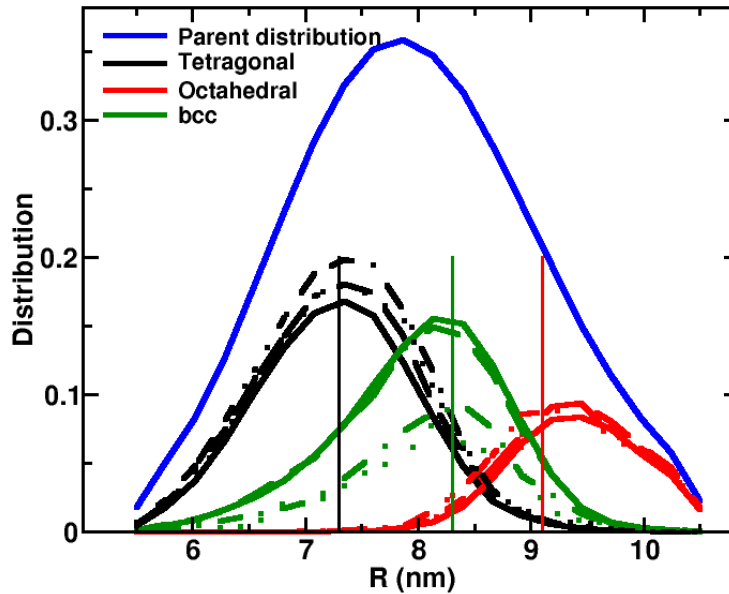


Figure 4.11: Particle size distributions in the bcc and MgZn_2 Laves phases as predicted by the MCM-CM simulations in the same conditions as in Fig. 4.9. The MCM simulations were performed at four different system sizes, $N = 4025$ (dotted lines), $N = 20125$ (dotted dashed lines), $N = 32200$ (dashed lines) and $N = 257600$ (solid lines). The parent size distribution (blue) and the mean particle size distributions as determined from the SAXS analysis (vertical lines) of the HS40 silica dispersion at $\phi = 24\%$ are also plotted for comparison. For clarity the size distribution of particles with a liquid-like order is omitted. The mean particle size (7.94 nm) of this latter is found to be marginally smaller than that of the parent size distribution (8 nm).

The size distributions of particles belonging to the bcc and MgZn_2 phases as predicted by the MCM-CM simulations at $\phi = 21\%$ are represented in Fig. 4.11, and are compared with the mean particle sizes determined from SAXS analysis of the crystallized HS40 silica dispersions at $\phi = 24\%$, see Ref. [8]. In the simulations, the particle size distribution of the Laves phase is found to depend only weakly on the system size, i.e. N , contrary to

what is observed in the bcc phase. As discussed earlier for Fig. 4.10, the proportion of the bcc phase, as it is formed after the Laves phase, is found to be sensitive to the specific configuration (size and position) of the MgZn_2 crystallites when $N \lesssim 30000$. However, the mean particle size of each phase, including the bcc phase, is insensitive to N for $N > 4000$. In the simulation, the average radii of 7.29, 8.03, and 9.40 nm for particles in the Laves tetragonal, bcc, and Laves octahedral sites, respectively, agree well with the corresponding experimental values of 7.3, 8.3, and 9.1 nm.

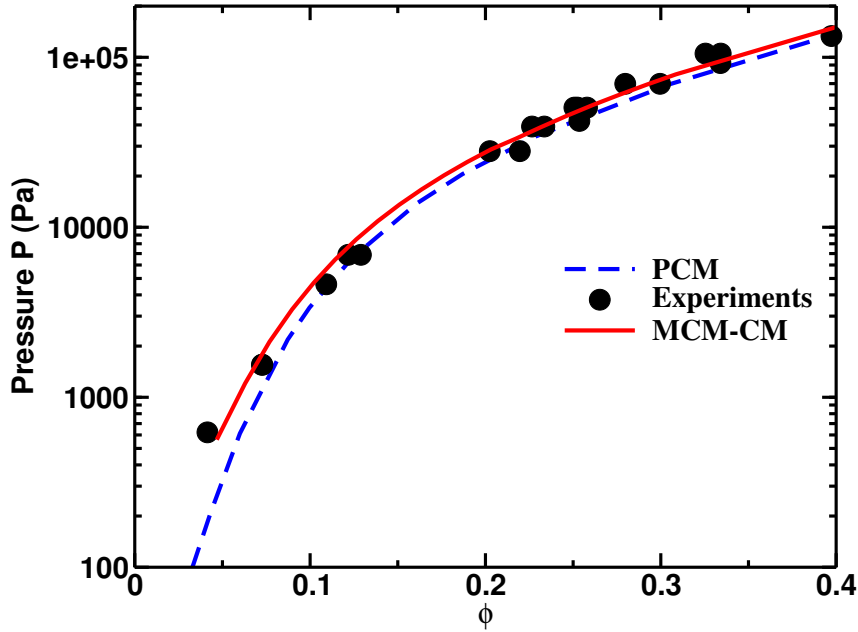


Figure 4.12: Equations of state of the HS40 silica dispersion equilibrated with a bulk solution at pH 9 and an ionic strength of 5 mM as obtained from osmotic stress measurements (experiments) and MCM-CM simulations. The osmotic pressure of the small ions as calculated from the PCM is also given for comparison, see Chapter 3.

Finally, the predicted and experimentally determined equations of state of the HS40 silica dispersion are presented in Fig. 4.12. The simulated EOS is calculated by employing the analytical correction term (volume term) derived by Boon *et al.*[164], which, when added to the usual virial pressure of the MCM, P_{MCM} , was shown to provide a very good approximation of the EOS calculated at the level of the full primitive model. The EOS defined as such reads,

$$\Pi_{EOS} = P_{MCM} + kT \frac{(\kappa^*)^2}{8\pi l_B} \left(1 - \left(\frac{\kappa}{\kappa^*} \right)^2 \right)^2 \quad (4.9)$$

The first term is calculated in the course of the simulation following the virial theorem;

the second term is analytically obtained from the effective inverse screening length of the suspension, κ^* , as determined from the PCM from the known inverse screening length of the bulk solution, κ , see Chapter 3. The EOS calculated by the PCM, which neglects the colloid-colloid correlations and thus underestimates the experimental results, is also given for comparison. Again, very good agreement is obtained, showing that the MCM-CM is able to accurately predict not only the structure but also the thermodynamic properties of HS40 silica dispersions.

4.3.2 TM50 silica suspensions

Figure 4.13 gives the predicted phase composition for the TM50-a silica particle dispersions equilibrated in a bulk solution at pH 9 and containing either 0.5 or 5 mM of 1-1 salt as obtained from the MCM-CM simulations. It is instructive here to compare these results with those of the HS40 dispersions for the same ionic strength (5 mM); compare Figures 4.13(b) and 4.10. We recall that the TM50-a dispersions have a larger \bar{R} (13.75 nm), i.e. interactions at the same ψ are on average greater and of longer range, and a much smaller polydispersity (10%) as compared to the HS40 dispersions (8 nm, 14%). As expected, the smaller polydispersity of the TM50-a results in a shift of the freezing transition to a lower volume fraction. Quite unexpectedly however, the ϕ interval in which the crystalline phases form is found to be much more limited, $0.18 \lesssim \phi \lesssim 0.24$ as compared to $0.2 \lesssim \phi \lesssim 0.4$ for the HS40. In other words, a lower polydispersity does not necessarily result in a better solidification! A more detailed inspection of the phase composition given in Figure 4.13(b) provides some explanations for this trend. In particular, the lower polydispersity of the TM50-a still allows for the formation of a Laves MgZn_2 phase but in a much lower proportion. At the same time, it favors the formation of a bcc phase on the low end of the solid region. However, it is still too large to stabilize the bcc phase when the volume fraction increases. Indeed, the bcc phase is rapidly found to be destabilized at the expense of a liquid phase. In other terms, the level of polydispersity of the TM50-a is favorable neither to the bcc phase (except in a small region of low ϕ values and ionic strength), nor to the Laves phase and even less so to the fcc phase, see below. Upon further increase in the volume fraction, the solid phases melt into a glass forming liquid. Note that this continuous transition is as rapid as that of HS40 dispersions. A simulation snapshot given in Figure 4.13(c) illustrates the very small proportion of the solid phases

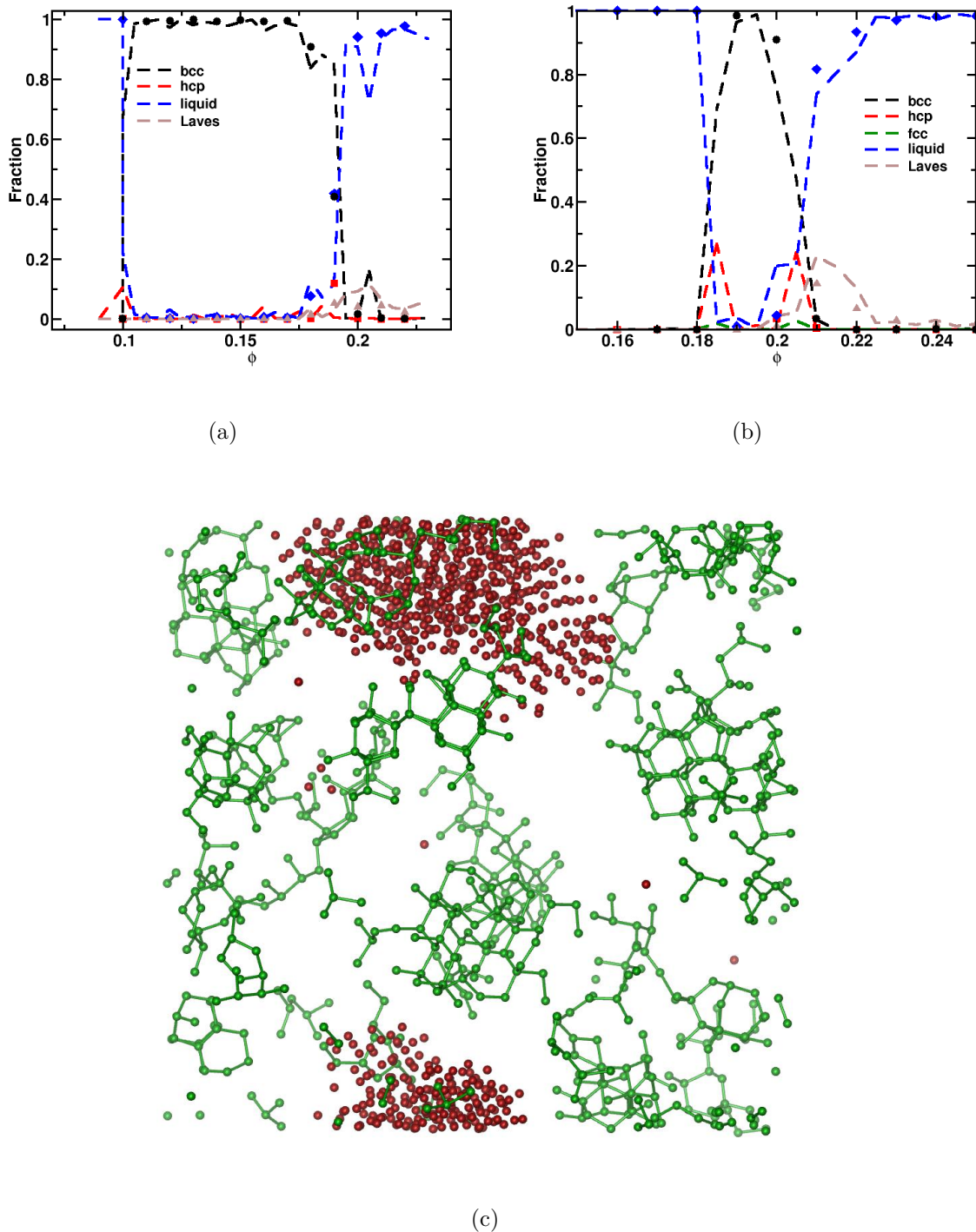


Figure 4.13: Phase composition of the TM50-a dispersions at pH 9 as predicted from MC simulations of the MCM-CM. The ionic strength is set to (a) 0.5 mM and (b) 5 mM. The simulations are performed with both $N = 4010$ (dotted lines) and $N = 20010$ (full symbols). (c) Simulation snapshot of an equilibrated TM50-a dispersion at $\phi = 21\%$ in a bulk solution containing 5 mM of 1-1 salt at pH 9. Particles in the bcc crystal-like order and in the tetragonal sites of the MgZn_2 phase are colored in red and green, respectively. Particles in liquid-like order and in the Laves tetragonal sites are not shown for clarity.

in the coexistence region of the Laves, bcc and fluid phases. The Laves MgZn_2 phase is only found in the form of small clusters, a finding which contrasts with the case of the HS40 dispersions.

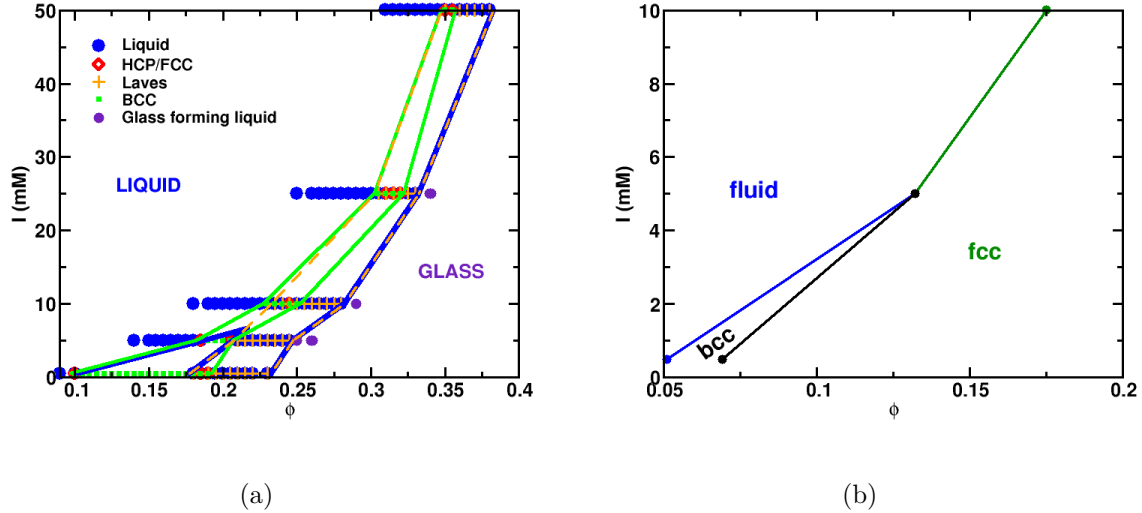


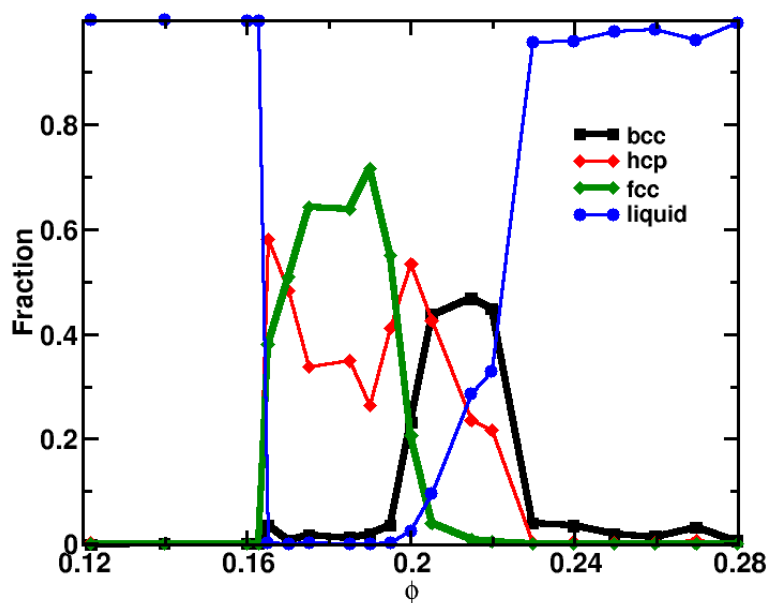
Figure 4.14: (a) Phase diagram presented in the ϕ - ionic strength plane of the TM50-a dispersion determined from MC simulations of the MCM-CM. The symbols refer to the analysis of the phase composition as obtained from the MCM-CM simulations in the NVT simulations. Lines give the approximate boundaries of the different phases estimated from these simulation analysis. (b) Phase diagram of a monodisperse silica particle suspension with $R = \bar{R}_{\text{TM50}}$ in the same equilibrium conditions as above. Symbols: calculated phase coexistence from the point Yukawa phase diagram of Hamaguchi, Farouki, and Dubin[232]. Lines: guides to the eyes.

One other striking difference with the HS40 dispersions is the complete crystallization of the dispersion in a bcc phase on the low end of the freezing transition which preempts the formation of the Laves phase. This region is further found to enlarge and to shift to lower values of ϕ with the increase in the magnitude of the colloidal interaction, that is when the ionic strength of the equilibrium solution decreases, as shown in Figure 4.13(a). When instead the ionic strength increases to over 5 mM, the region of the bcc phase shrinks and is incorporated into that of the fluid phase. This is best seen in the approximate phase diagram plotted in Figure 4.14. Note that a determination of the exact location of the phase boundaries and coexistence regions would have necessitated intensive calculations of phase free energies which are beyond the scope of the present work. However, the simulation tools to do so are yet to be defined and designed for systems such

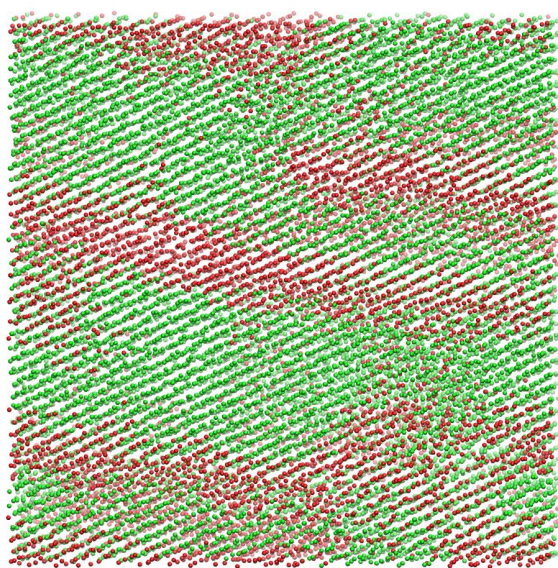
as ours whose interactions are density dependent, see Ref. [264] and discussion section below. A comparison with the phase diagram of the monodisperse suspensions, Figure 4.14(b), with the same \bar{R} in the same equilibrium conditions shows, as expected, that polydispersity enhances the stability of the fluid phase, see e.g. the shift in the freezing transition. Even more interestingly, polydispersity destabilizes almost completely the fcc phase, that is the equilibrium phase in the monodisperse case. Qualitatively, the same results have been obtained and discussed at some length by Botet *et al.*[258] using lattice MC simulations in the Gibbs ensemble allowing these authors to study the equilibrium distribution of HCY particles between two predefined and different crystal lattices. Their simulations clearly show that when the size polydispersity is increased, the initially stable fcc phase is progressively destabilized at the expense of the bcc phase. This is primarily an entropic effect as the number of possible configurations in an fcc crystal lattice, i.e. without particle overlaps, drops faster than in a bcc lattice and eventually becomes lower. When the particles in the simulations are allowed to move freely and are not artificially constrained to fixed lattice positions, the entropic effect becomes more pronounced. The free volume being higher in the bcc phase than in the fcc phase, one consequence of the lattice simulations is thus to overestimate the stability of the fcc phase with respect to the bcc phase, see e.g. Ref. [8].

When the polydispersity is further decreased to 7% the formation of the Laves phase is completely inhibited. This is shown in Figure 4.15(a), which gives the phase composition of the TM50-b dispersions in the same equilibrium conditions as the HS40 dispersions and TM50-a dispersions in Figure 4.13(b). Here, a fcc phase followed by a bcc phase, both in coexistence with an HCP phase, are found at the freezing transition. As expected again, the freezing transition is found at lower ϕ values as compared to the two preceding dispersions and at larger values than in the monodisperse case. As with the monodisperse case, an fcc phase, although in coexistence with an hcp phase, is found among the equilibrium crystalline phases at the start of the freezing transition. Further inside the freezing transition, at $\phi = 19.5\%$, an fcc-bcc phase transition appears. Upon further increase in the volume fraction, the crystalline phases eventually melt all together into a glass forming liquid.

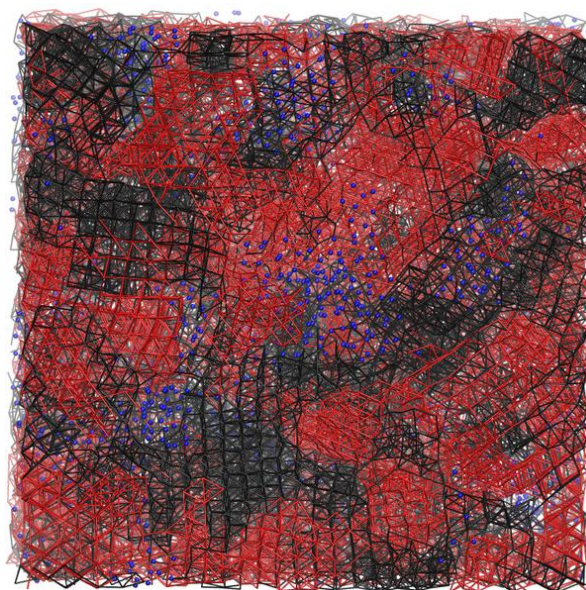
Two representative snapshots of the TM50-b dispersions, equilibrated with a solution containing 5 mM of salt and at pH 9, illustrating the phase coexistence in the dominant



(a)



(b)



(c)

Figure 4.15: (a) Phase composition of the TM50-b dispersions at pH 9 as predicted from MC simulations of the MCM-CM. The ionic strength is set to 5 mM. The simulations are performed with $N = 20010$. (b-c) Simulation snapshots at (b) $\phi = 0.185$ and (c) $\phi = 0.205$ of the TM50-b dispersion equilibrated with a bulk solution containing 5 mM of a 1-1 salt at pH 9. The same color code as in (a) is used, that is black for the bcc phase, red for the hcp phase, green for fcc phase and blue for the fluid phase.

equilibrium domain of the fcc phase ($\phi = 18.5\%$) and just after the fcc-bcc phase transition ($\phi = 20.5\%$) are shown in Figures 4.15(b) and 4.15(c). A stratified structure is observed when the hcp and fcc crystalline phases coexist. On the other hand, an intermixed structure between the hcp and bcc phase is found at higher volume fraction. This finding suggests a spinodal decomposition of the dispersion, or at least that the interfacial free energy between the two phases is very low.

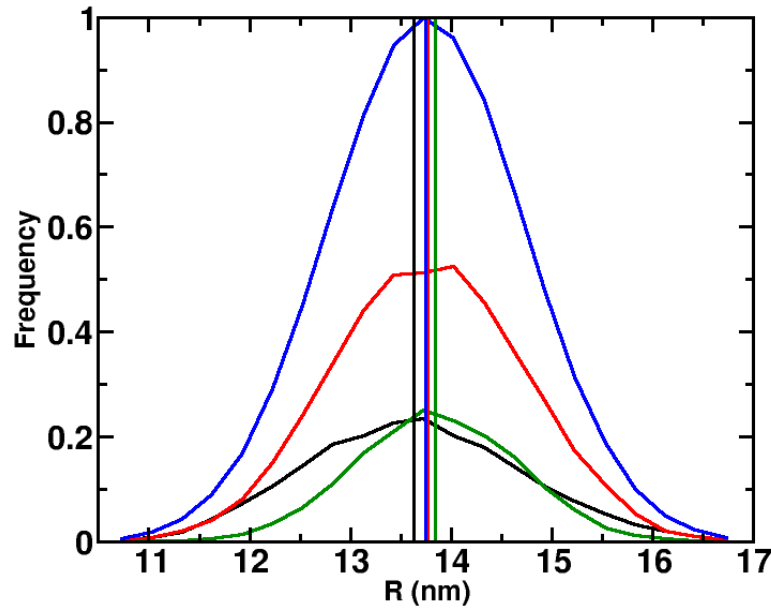


Figure 4.16: Simulated particle size distributions in the fcc (green), hcp (red) and bcc (black) crystalline phases in comparison with the parent size distribution (blue) for the TM50-b silica dispersion at $\phi = 20.5\%$ and in equilibrium with a bulk solution containing 5 mM of 1-1 salt at pH 9. The vertical lines give the mean particle size of each phases. The MC simulations were performed with 20010 particles using the MCM-CM.

Figure 4.16 represents the particle population of the different phases at the hcp-fcc-bcc phase coexistence. The bcc phase is more tolerant to variations in particle size than the fcc phase, as can be seen from the somewhat larger polydispersity of its particle distribution. At the same time, the bcc phase tends to incorporate on average smaller particles than the fcc phase. On the contrary, the mean radius of the particles in the hcp phase is the same as in the parent particle distribution. Particle segregation remains limited however.

Figure 4.17(a) shows the approximate phase diagram from MCM-CM simulations of the TM50-b dispersions at pH 9 in the volume fraction - ionic strength representation.

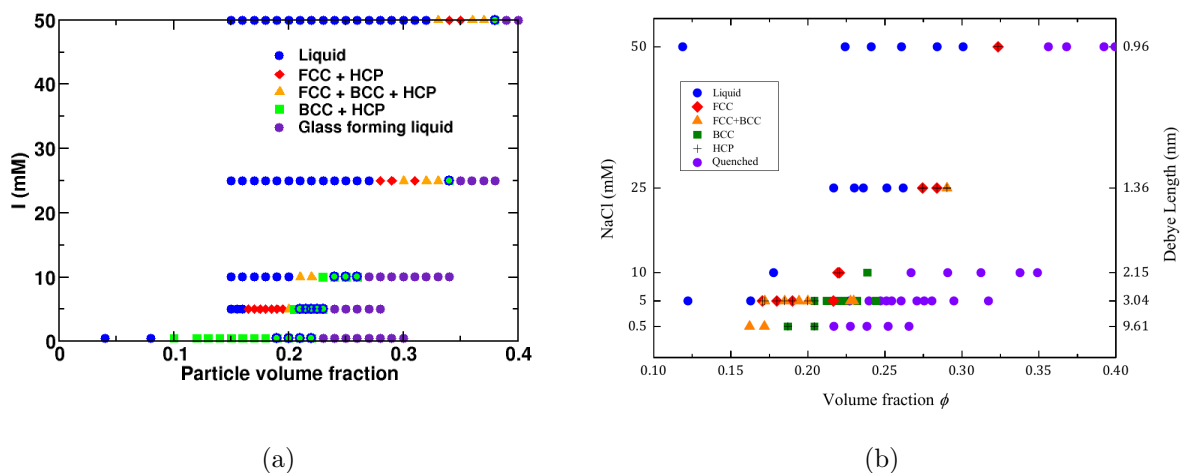


Figure 4.17: Simulated (a) and experimental (b) phase diagrams of the TM50 silica dispersions equilibrated at pH 9 in volume fraction - ionic strength (or inverse Debye length) representation. The simulation results are for the TM50-b. They are produced with MC simulations in the NVT ensemble of the MCM-CM with $N = 20010$. The experimental phase diagram is from Kiatkirakajorn *et al.*[9]. It was obtained after two month of equilibration from synchrotron based small x-ray scattering (SAXS) measurements. The presence of an hcp or rhcp phase was also systematically observed in coexistence with the other solid phases but not reported in the experimental phase diagram.

When the ionic strength of the bulk solution is increased to more than 5 mM, the inversion of the appearance of the fcc-bcc phases is preserved. The region of stability of the bcc phase is, however, progressively reduced and shifted to higher ϕ values. On the contrary, when the ionic strength is decreased to less than 5 mM, the solid region is dominated by the bcc phase. A comparison of the phase diagrams of the TM50-b and TM50-a dispersions shows that the solid – (glass forming liquid) transition occurs at *lower* ϕ as the size polydispersity *decreases*. This is all the more true when the ionic strength is low. The re-entrant melting is further found to be much sharper when the polydispersity of the dispersion is smaller; compare Figures 4.15(a) and 4.10. Taken together, these results confirm the greater tolerance of the Laves phase in regard to size distribution than the bcc phase.

Figure 4.17(b) presents the experimental phase diagram of the TM50 silica dispersions measured by Kiatkirakajorn *et al.*[9] in the same equilibrium conditions of pH and ionic strengths. With the exception of the lowest salt concentration studied (0.5 mM), the experimental phase diagram is found to compare very satisfactorily with the simulated one. In particular, the freezing and re-entrant melting transitions are in very good agreement. In addition, the predicted destabilization of the fcc phase in favor of the bcc phase upon increase in the volume fraction is confirmed. The discrepancy at low ionic strength may be due to the experimental difficulty to keep a low ionic strength while maintaining a high pH. It may also be due to the shielding of the effective pair potential [265, 234] which has been shown to be significant at small ionic strengths.

Figure 4.18, finally, compares the simulation predictions with the measured equations of state of the TM50 silica dispersions for varying ionic strengths and at a set pH of 9. As can be seen, the predicted osmotic pressures from the MCM simulations (and calculated using Eq. 4.9) are in very good agreement with their experimental counterparts. In particular, the close agreement is maintained in the regime of high ionic strength where the calculated osmotic pressures from the PCM alone is known and shown here, Figure 4.18, to underestimate experimental values, as it neglects the contribution of the colloid correlations.

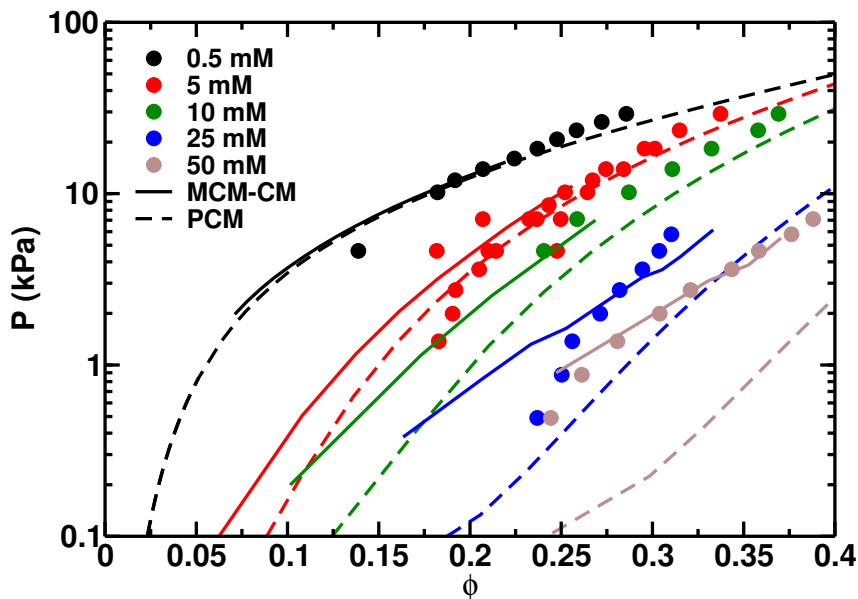


Figure 4.18: Comparison of the experimental (symbols) and simulated (lines) equations of state of the TM50 silica dispersion equilibrated in a bulk solution at pH 9 containing various amounts of 1-1 salt. MCM-MC: Osmotic pressures calculated from Eq. 4.9 using MC simulations of the MCM-CM. PCM: Osmotic pressure calculated from the polydisperse cell model, see Chapter 3. Symbols: experimental data.

4.3.3 Discussion and conclusion

The above results call for further discussion on a number of points. We first discuss solid phase tolerance to particle size polydispersity, then turn to the re-entrant melting transition and comment on the limitations of the model and simulation used and finally offer some general conclusions.

One of the main interests of the present study is to question the generally accepted idea that the smaller the size polydispersity, the better a colloidal dispersion may crystallize. While the increased stability of the fluid phase and the corresponding shift of the freezing transition to higher ϕ with increased size polydispersity is not put into question, our results strongly suggest that this shift can be more than simply compensated by the concomitant shift toward the higher ϕ of the re-entrant melting transition. In other words, solid crystalline phases can form in a larger ϕ gap when polydispersity increases. Obviously, this is not true in the limit of monodispersity where no re-entrant melting transition is observed. At the same time in experiments, particle dispersions always present some polydispersity. Interestingly, a larger region of crystalline phases is found in

colloidal suspensions with rather large size polydispersity, typically here higher than 10%, in which solid phases with superlattice structures made of small and large particles, here Laves phases, are stable. The AB_2 phase is further shown to persist at high pressures, up to 100 kPa in the case of the HS40 silica particle suspensions, where the solid phases with unimodal compositions found in the TM50 silica dispersions had long disappeared. On the contrary, when the polydispersity is decreased, the AB_2 phase formation is limited and eventually completely inhibited. The bcc phase, instead, is found to stabilize. Due to its lower packing volume density and lower tolerance to size polydispersity however, it is marked by a rather sudden melting upon increase in the volume fraction. The much higher tolerance to size polydispersity of the AB_2 phase can be explained by the large gain in mixing entropy associated with its bimodal particle composition as compared, for example, to a fractionated system in two coexisting, but different, bcc phases composed of the same sub-populations of particles (A and B) as the AB_2 phase.

The concomitance in the position of the re-entrant melting transition between the simulations and the experiments seen in the TM50 silica nanoparticle dispersions is somewhat surprising and calls for further investigation. This concomitance may suggest that the glass forming liquid formed is thermodynamically stable or that its metastability state is very stable. Whatever the response, its formation is favored by the interaction potential asymmetry stemming from the pronounced charge polydispersity of the titrating silica nanoparticles. In addition, the glass forming liquids found here present strong similarities with those found in suspensions of highly soft particles, e.g. microgels. Besides the fact that they also form at rather moderate volume fractions from the melting of solid phases, they are marked by the absence of a specific local geometry (e.g. an icosahedral structure) and by a rather homogeneous structure. All these preliminary results suggest that the glass forming liquid found in charged polydisperse silica particle suspensions is a good glass former and may constitute an excellent experimental and theoretical model to study the glassy state and to test the associated theories.

Despite the surprisingly good predictive capacity of the MCM-CM and associated MC simulations, they can and should be improved still further. As we have seen, the model seems to give a rather poor description of the silica suspensions at the lowest ionic strength. An alternative might be the PRJM, also in the mean-field Poisson-Boltzmann approximation. Another alternative might be the corresponding models (CM and RJM) in the full

primitive model. Although much more computer demanding, the associated simulations can be automatized and the computing time should continue to decline significantly with technological developments in processor and hardware. The charge polydispersity driven by the charge regulation is in our opinion one of the keys of the success of the present model. However, the charge regulation is accounted for at a very “mean-field” level. Indeed, the charge on a particle should in principle not respond to the “mean” interactions it undergoes (here the mean density and mean composition of the suspension) but to the specific interactions to which it is exposed in each of its configurations with its neighbors.

We pragmatically used NVT and NPT MC simulations which combined with the very efficient swap move, allow for the thermalization of polydisperse colloidal suspensions up to very high ϕ . Although pragmatic and efficient, the MC simulations employed are limited in two senses: (i) the exact phase boundaries and coexistence regions of the phase diagram are not accessible; (ii) the fractionation, relaxation and density fluctuation of the system may be limited due to finite size and interfacial effects[177]. In the specific case of interest here, after noting that the fluid composition and the size polydispersity of the different phases formed are rather insensitive to the volume fraction, an approximate phase diagram could be obtained by thermodynamic integration combined with the corrected equation of state, Eq. 4.9, derived by Boon *et al.*[164]. However, this method would be inoperative in determining the truly thermodynamic phase behavior in the region of the observed glass forming liquid. In principle, the semi-grand isobaric ensemble developed by Wilding *et al.*[177] could solve these issues. This method is nonetheless complicated by the density and composition dependence of the effective pair potentials. This is not only a question of technical difficulties. Indeed, in the thermodynamic limit (infinite phases), relevant when one is interested in computing/determining a phase diagram, each phase has its own particle size distribution (composition) and density. The effective pair potentials would thus need to be computed for each specific density and composition visited during the course of the simulations, not to mention the required (by the ensemble) distribution of chemical potentials that must be adjusted to the original particle size distribution! Obviously, one can always disregard this problem, as has been done in the present work, and it seems to be a good approximation. However, when large fractionation is at work, typically at high ϕ , this approximation might break down and again lead to an approximate or simply a false phase diagram. In any case, we hope that these results and

discussions will motivate further experimental and theoretical investigations to contribute to deciphering these open scientific issues.

To conclude, Monte Carlo simulations of two multi-component models were deployed and confronted to the structures and equations of state measured for aqueous suspensions of two different sets of polydisperse silica nanoparticles (Ludox HS40 and Ludox TM50) in a large range of equilibrium conditions. The MCMs were developed in the framework of the mean-field Poisson-Boltzmann equation approximation based on a generalization of either the cell model or the renormalized jellium model to account for the polydispersity and charge regulation of the colloids, see Chapter 3. The MC simulations of the MCMs models were performed in the NVT and NPT ensembles which, combined to a swap move, efficiently equilibrate charged polydisperse particle suspensions up to high volume fractions. The MCM-CM simulations were found to predict very satisfactorily the phase compositions and their locations in the experimental phase diagrams. This includes, but is not limited to, the fractionation of the HS40 silica particle suspensions in a MgZn_2 Laves phase in coexistence with a bcc phase and the re-entrant melting transition in the TM50 silica particle suspensions. The MCM-CM simulations predict the equations of state for the two silica dispersions equally well. The MCM-RJM simulations are found, on the other hand, to be unable to reproduce the experimental data. In good agreement with the experimental data, a glass forming liquid is predicted by the MCM-CM simulations at rather modest ϕ . Preliminary results suggest that it is a good glass former with a rather homogeneous structure, properties that will be studied in more detail in a forthcoming study.

Acknowledgements

I would like to thank Joaquim Li, Pree-Cha Kiatkirakajorn, Lucas Goehring and Bernard Cabane for the experimental results presented in this chapter, and for the nice collaboration.

Conclusions

My PhD studies delved into the impact of density, electrostatic coupling and polydispersity on the colloidal interactions and the structural properties of charged colloidal dispersions. To address these questions, I developed and used simulation techniques based on Monte Carlo simulations and mean field calculations. The successful strategy has been to use a hierarchical multiscale approach which consists in calculating the effective pair potential of interaction between the colloids at a low enough scale, to include the main physics and chemistry of the system, and to inject them in a colloid-only simulation. Although not a new strategy, the calculation of the $w^*(r)$ turned out to be far from trivial in the context of aqueous dispersions of polydisperse and titratable colloids or of concentrated and highly coupled systems. I developed and tested three methods at different level of approximations.

In Chapter 2, I developed a first method based on the calculation of pair potential of mean force between two colloids in a cubic box with periodic boundary conditions. The method takes advantage of the fact that the main contribution of the many-body interactions, occurring in concentrated dispersions of charged colloids, is due to the mean increase in counterion concentration and corresponding depletion in co-ions. The variation in colloid density is then simply mimicked by an appropriate change in the concentration of counterions neutralized by an homogeneous background charge. The method was tested at the level of the primitive model. A good description of the structure of the colloidal dispersion was obtained in the low and high coupling regimes, even at high colloid densities. The method can easily be used in popular molecular simulation program packages, extended to non-spherical and generalized to polydisperse systems. In the latter case, however, the method can be very time consuming.

In that respect, the mean field version of the cell and renormalized jellium models, CM and RJM, sounded more practicable at least for not too highly coupled systems,

as developed in Chapter 3. Indeed, when this later condition is met, the effective pair potential is known to be of the Yukawa form but with renormalized parameters which, in the monodisperse case, can be easily extracted from the CM and RJM. Inspired by the seminal work of Torres et al.[101] and taking advantage of the quadratic variation of charge with the particle radius, I developed a code based on both the CM and RJM methods that enables the calculation of $w^*(r)$ for charged colloidal systems with continuous size distribution. The two methods were further generalized to include the charge regulation of titratable colloids using a 1-pK Stern model. When adjusted with independent measurements, like e.g. surface charge titration by potentiometric measurement, a virtue of such developed methods is to be parameter free. A comparison of the measured and calculated equation of state on various commercially available silica dispersions gave some first indications that the CM based method is more accurate than that based on the RJM for systems with finite salt concentrations.

In Chapter 4, simulation results of the colloid-only multi-component model (MCM), based on the polydisperse CM and RJM methods, are compared with the structures and equations of state measured by our collaborators (Joaquim Li, Pree-Cha Kiatkirakajorn, Lucas Goehring and Bernard Cabane) for aqueous suspensions of two different sets of polydisperse silica nanoparticles (Ludox HS40 and Ludox TM50) in a large range of equilibrium conditions. The simulations were performed with a MC technique in the NVT and NPT ensembles which, combined with a swap move, efficiently equilibrates charged polydisperse particle suspensions up to high volume fractions. The MCM-RJM is found to be unable to reproduce the experimental data. On contrary, the MCM-CM is shown to predict very well the equation of state of the two dispersions. In addition, the MCM-CM simulations are found to predict very satisfactorily the phase compositions of the silica suspensions and their locations in the experimental phase diagrams. This includes but is not limited to an MgZn_2 Laves - bcc phase coexistence and a re-entrant melting phenomenon, in good agreement with the experimental data published elsewhere[8]. It should be mentioned that repeated SAXS experiments on different samples of the same dispersion (Ludox HS40) revealed also the presence of an AB_{13} phase[9], so far unpredicted by our simulations. However, some questions remain on the uncertainty and accuracy of the numerical method used to extract the size distribution of the recorded SAXS spectra.

The results obtained provide some answers to the questions raised in the introduc-

tion, see Chapter 1. 1) My simulation results give some clear evidence that short range attractive forces and resulting aggregation of colloids are not the source of the continuous amorphization of the charged polydisperse colloidal dispersions at high densities, i.e. decrease in the short range order as the colloid density increases. In contrast, they suggest the formation of a glass forming liquid favored by the large asymmetry in the repulsive interactions stemming from the polydispersity. This is supported by the surprising concomitance of the re-entrant melting transition between the simulations and the experiments on the silica nanoparticle dispersions. These results call for further investigations.

2) We have shown that the bcc solid phase is stabilized by polydispersity instead of the more compact fcc solid phase, in good agreement with experiments. For relatively small polydispersities, this gives rise to an inversion in the order of appearance of the solid phases compared to the monodisperse case. That is, a fcc solid phase is found to form first followed by a bcc solid phase as the colloid density is increased. For larger polydispersities up to 14%, colloidal crystals with fcc structure disappear all together in favor with those of bcc and MgZn_2 structure. In future studies it would be interesting to investigate larger polydispersities as well as the effect of the distribution shape.

3) The overall good agreement obtained between the simulated and experimental results on two different silica dispersions gives some confidence in the pragmatic simulation strategy used and its predictive capacity as well as in the soundness of the models and numerical methods developed. As discussed in the last chapter, the simulation approach presents a certain number of limitations which I hope will motivate further developments. More generally, I hope that this work will motivate further experimental and theoretical investigations to contribute to deciphering these fascinating systems.

Bibliography

- [1] D.H. Everett. Definitions, Terminology and Symbols in Colloid and Surface Chemistry. *Pure Applied Chemistry*, 31(4):579–638, 1972.
- [2] Robert J. Hunter. *Introduction to modern colloid science*. Oxford University Press, 1993.
- [3] Sabine Laschat, Angelika Baro, Nelli Steinke, Frank Giesselmann, Constanze Hägele, Giusy Scalia, Roxana Judele, Elisabeth Kapatsina, Sven Sauer, Alina Schreivogel, and Martin Tosoni. Discotic Liquid Crystals: From Tailor-Made Synthesis to Plastic Electronics. *Angewandte Chemie International Edition*, 46(26):4832–4887, jun 2007.
- [4] F. Meseguer. Colloidal crystals as photonic crystals. *Colloids and Surfaces A: Physicochemical and Engineering Aspects*, 270-271:1–7, dec 2005.
- [5] B. V. Derjaguin and L. Landau. Theory of the stability of strongly charged lyophobic sols and of the adhesion of strongly charged particles in solutions of electrolytes. *Acta Physico Chim USSR*, 14:633–662, 1941.
- [6] E. J. W. Verwey and J. Th G. Overbeek. *Theory of the Stability of Lyophobic Colloids*. Elsevier Publishing Company Inc., Amsterdam, 1948.
- [7] Joaquim Li, Bernard Cabane, Michael Sztucki, Jérémie Gummel, and Lucas Goehring. Drying Dip-Coated Colloidal Films. *Langmuir*, 28(1):200–208, jan 2012.
- [8] Bernard Cabane, Joaquim Li, Franck Artzner, Robert Botet, Christophe Labbez, Guillaume Bareigts, Michael Sztucki, and Lucas Goehring. Hiding in Plain View: Colloidal Self-Assembly from Polydisperse Populations. *Physical Review Letters*, 116(20):208001, may 2016.

- [9] Pree-Cha Kiatkirakajorn. *Morphological instabilities in drying colloids*. PhD thesis, Georg-August University School of Science, sep 2018.
- [10] J. D. Bernal and I. Fankuchen. X-ray and crystallographic studies of plant virus preparations. *Journal of General Physiology*, 25(1):111–146, sep 1941.
- [11] Robley C. Williams and Kenneth M. Smith. A Crystallizable Insect Virus. *Nature*, 179(4551):119–120, jan 1957.
- [12] Irving Langmuir. The Role of Attractive and Repulsive Forces in the Formation of Tactoids, Thixotropic Gels, Protein Crystals and Coacervates. *Journal of Chemical Physics*, 6(12):873–896, Dec 1938.
- [13] J. B. Jones, J. V. Sanders, and E. R. Segnit. Structure of Opal. *Nature*, 204(4962):990–991, dec 1964.
- [14] P.J. Darragh, A.J. Gaskin, and J. V. Sanders. Opals. *Scientific American*, 234(4):84–95, 1976.
- [15] R. K. Iler. *The Chemistry of Silica*. John Wiley, New York, 1979.
- [16] B. J. Alder and T. E. Wainwright. Phase Transition for a Hard Sphere System. *Journal of Chemical Physics*, 27(5):1208–1209, nov 1957.
- [17] W. W. Wood and J. D. Jacobson. Preliminary Results from a Recalculation of the Monte Carlo Equation of State of Hard Spheres. *Journal of Chemical Physics*, 27(5):1207–1208, nov 1957.
- [18] P. N. Pusey and W. van Megen. Phase behaviour of concentrated suspensions of nearly hard colloidal spheres. *Nature*, 320(6060):340–342, mar 1986.
- [19] Pawel Pieranski. Colloidal crystals. *Contemporary Physics*, 24(1):25–73, 1983.
- [20] John G. Kirkwood, Eugene K. Maun, and Berni J. Alder. Radial Distribution Functions and the Equation of State of a Fluid Composed of Rigid Spherical Molecules. *Journal of Chemical Physics*, 18(8):1040–1047, aug 1950.
- [21] Daan Frenkel. Entropy-driven phase transitions. *Physica A: Statistical Mechanics and its Applications*, 263(1):26–38, feb 1999.

- [22] P. N. Pusey, W. van Meegen, P. Bartlett, B. J. Ackerson, J. G. Rarity, and S. M. Underwood. Structure of crystals of hard colloidal spheres. *Physical Review Letters*, 63:2753–2756, Dec 1989.
- [23] W. G. T. Kranendonk and D. Frenkel. Computer simulation of solid-liquid coexistence in binary hard-sphere mixtures. *Journal of Physics: Condensed Matter*, 1(41):7735, 1989.
- [24] W. G. T. Kranendonk and D. Frenkel. Computer simulation of solid-liquid coexistence in binary hard sphere mixtures. *Molecular Physics*, 72(3):679–697, feb 1991.
- [25] Marjolein Dijkstra, René van Roij, and Robert Evans. Phase diagram of highly asymmetric binary hard-sphere mixtures. *Physical Review E*, 59(5):5744–5771, may 1999.
- [26] L. Filion, M. Hermes, R. Ni, E. C. M. Vermolen, A. Kuijk, C. G. Christova, J. C. P. Stiefelhagen, T. Vissers, A. van Blaaderen, and M. Dijkstra. Self-assembly of a colloidal interstitial solid with tunable sublattice doping. *Physical Review Letters*, 107:168302, Oct 2011.
- [27] M. J. Murray and J. V. Sanders. Close-packed structures of spheres of two different sizes II. The packing densities of likely arrangements. *Philosophy Magazine A*, 42(6):721–740, dec 1980.
- [28] Laura Filion and Marjolein Dijkstra. Prediction of binary hard-sphere crystal structures. *Physical Review E*, 79(4):046714, apr 2009.
- [29] M. D. Eldridge, P. A. Madden, and D. Frenkel. Entropy-driven formation of a superlattice in a hard-sphere binary mixture. *Nature*, 365(6441):35–37, sep 1993.
- [30] M.D. Eldridge, P.A. Madden, P.N. Pusey, and P. Bartlett. Binary hard-sphere mixtures: a comparison between computer simulation and experiment. *Molecular Physics*, 84(2):395–420, 1995.
- [31] P. Bartlett, R. H. Ottewill, and P. N. Pusey. Superlattice formation in binary mixtures of hard-sphere colloids. *Physical Review Letters*, 68(25):3801–3804, jun 1992.

- [32] Antti-Pekka Hynninen, Job H. J. Thijssen, Esther C. M. Vermolen, Marjolein Dijkstra, and Alfons van Blaaderen. Self-assembly route for photonic crystals with a bandgap in the visible region. *Nature Materials*, 6(3):202–205, mar 2007.
- [33] Nicole Schaertl, Thomas Palberg, and Eckhard Bartsch. Formation of laves phases in repulsive and attractive hard sphere suspensions. *ArXiv*, eprint 1702.05817, feb 2017.
- [34] A.-P. Hynninen, L. Filion, and M. Dijkstra. Stability of LS and LS2 crystal structures in binary mixtures of hard and charged spheres. *Journal of Chemical Physics*, 131(6):064902, aug 2009.
- [35] M. D. Eldridge, P. A. Madden, and D. Frenkel. Entropy-driven formation of a superlattice in a hard-sphere binary mixture. *Nature*, 365(6441):35–37, sep 1993.
- [36] Moreno Fasolo and Peter Sollich. Fractionation effects in phase equilibria of polydisperse hard-sphere colloids. *Physical Review E*, 70(4):041410, oct 2004.
- [37] E. B. Sirota, H. D. Ou-Yang, S. K. Sinha, P. M. Chaikin, J. D. Axe, and Y. Fujii. Complete phase diagram of a charged colloidal system: A synchrotron x-ray scattering study. *Physical Review Letters*, 62(13):1524–1527, mar 1989.
- [38] Evert Jan Meijer and Daan Frenkel. Melting line of Yukawa system by computer simulation. *Journal of Chemical Physics*, 94(3):2269–2271, feb 1991.
- [39] Nina J. Lorenz, Hans Joachim Schöpe, Holger Reiber, Thomas Palberg, Patrick Wette, Ina Klassen, Dirk Holland-Moritz, Dieter Herlach, and Tsuneo Okubo. Phase behaviour of deionized binary mixtures of charged colloidal spheres. *Journal of Physics: Condensed Matter*, 21(46):464116, 2009.
- [40] Mirjam E. Leunissen, Christina G. Christova, Antti-Pekka Hynninen, C. Patrick Royall, Andrew I. Campbell, Arnout Imhof, Marjolein Dijkstra, René van Roij, and Alfons van Blaaderen. Ionic colloidal crystals of oppositely charged particles. *Nature*, 437:235, sep 2005.
- [41] Markus Bier, René van Roij, and Marjolein Dijkstra. Phase diagrams of binary mixtures of oppositely charged colloids. *Journal of Chemical Physics*, 133(12):124501, sep 2010.

- [42] Masayuki Hasaka, Hiromichi Nakashima, and Kensuke Oki. Structure of the laves phase observed in polystyrene latexes. *Transactions of the Japan Institute of Metals*, 25(2):65–72, 1984.
- [43] William G. Hoover and Francis H. Ree. Melting Transition and Communal Entropy for Hard Spheres. *Journal of Chemical Physics*, 49(8):3609–3617, Oct 1968.
- [44] Mark. O. Robbins, Kurt Kremer, and Gary S. Grest. Phase diagram and dynamics of Yukawa systems. *Journal of Chemical Physics*, 88(5):3286–3312, mar 1988.
- [45] P. N. Pusey. The effect of polydispersity on the crystallization of hard spherical colloids. *Journal de Physique France*, 48(5):709–712, may 1987.
- [46] Paul Bartlett. Fractionated crystallization in a polydisperse mixture of hard spheres. *Journal of Chemical Physics*, 109(24), 1998.
- [47] David A. Kofke and Peter G. Bolhuis. Freezing of polydisperse hard spheres. *Physical Review E*, 59(1):618–622, jan 1999.
- [48] Peter Sollich. Predicting phase equilibria in polydisperse systems. *Journal of Physics: Condensed Matter*, 14(3):R79, 2002.
- [49] Ludovic Berthier and Giulio Biroli. Theoretical perspective on the glass transition and amorphous materials. *Review of Modern Physics*, 83(2):587–645, jun 2011.
- [50] Thomas Palberg, Patrick Wette, and Dieter M. Herlach. Equilibrium fluid-crystal interfacial free energy of bcc-crystallizing aqueous suspensions of polydisperse charged spheres. *Physical Review E*, 93(2):022601, feb 2016.
- [51] P. N. Pusey and W. van Megen. Observation of a glass transition in suspensions of spherical colloidal particles. *Physical Review Letters*, 59(18):2083–2086, nov 1987.
- [52] D. Frenkel and B. Smit. *Understanding Molecular Simulation*. Academic Press, San Diego, 2002.
- [53] L. A. Fernández, V. Martín-Mayor, and P. Verrocchio. Phase Diagram of a Polydisperse Soft-Spheres Model for Liquids and Colloids. *Physical Review Letters*, 98(8):085702, feb 2007.

- [54] Tomás S. Grigera and Giorgio Parisi. Fast Monte Carlo algorithm for supercooled soft spheres. *Physical Review E*, 63(4):045102, mar 2001.
- [55] Giovanni Bussi, Davide Donadio, and Michele Parrinello. Canonical sampling through velocity rescaling. *Journal of Chemical Physics*, 126(1):014101, jan 2007.
- [56] Berk Hess, Carsten Kutzner, David van der Spoel, and Erik Lindahl. GROMACS 4: Algorithms for Highly Efficient, Load-Balanced, and Scalable Molecular Simulation. *Journal of Chemical Theory and Computation*, 4(3):435–447, mar 2008.
- [57] Christopher J. Fennell and J. Daniel Gezelter. Is the Ewald summation still necessary? Pairwise alternatives to the accepted standard for long-range electrostatics. *Journal of Chemical Physics*, 124:4104, jun 2006.
- [58] D. Wolf, P. Keblinski, S. R. Phillpot, and J. Eggebrecht. Exact method for the simulation of Coulombic systems by spherically truncated, pairwise r-1 summation. *Journal of Chemical Physics*, 110(17):8254–8282, apr 1999.
- [59] D. J. Auerbach, W. Paul, A. F. Bakker, C. Lutz, W. E. Rudge, and Farid F. Abraham. A special purpose parallel computer for molecular dynamics: motivation, design, implementation, and application. *Journal of Physical Chemistry*, 91(19):4881–4890, sep 1987.
- [60] Martin Turesson, Bo Jönsson, and Christophe Labbez. Coarse-Graining Intermolecular Interactions in Dispersions of Highly Charged Colloids. *Langmuir*, 28(11):4926–4930, 2012.
- [61] Axel Thuresson, Magnus Ullner, and Martin Turesson. Interaction and Aggregation of Charged Platelets in Electrolyte Solutions: A Coarse-Graining Approach. *Journal of Physical Chemistry B*, 118(26):7405–7413, jul 2014.
- [62] E Allahyarov and H Löwen. Nonadditivity in the effective interactions of binary charged colloidal suspensions. *Journal of Physics: Condensed Matter*, 21(42):424117, oct 2009.
- [63] Dirk Reith, Mathias Pütz, and Florian Müller-Plathe. Deriving effective mesoscale potentials from atomistic simulations. *Journal Computational Chemistry*, 24(13):1624–1636, 2003.

- [64] Florian Müller-Plathe. Coarse-graining in polymer simulation: From the atomistic to the mesoscopic scale and back. *ChemPhysChem*, 3(9):754–769, 2002.
- [65] S. Alexander, P. M. Chaikin, P. Grant, G. J. Morales, P. Pincus, and D. Hone. Charge renormalization, osmotic pressure, and bulk modulus of colloidal crystals: Theory. *Journal of Chemical Physics*, 80(11):5776–5781, 1984.
- [66] E. Trizac and Y. Levin. Renormalized jellium model for charge-stabilized colloidal suspensions. *Physical Review E*, 69:031403, 2004.
- [67] Jacob Israelachvili. *Intermolecular and Surface Forces*. Academic Press, 2nd edition, 1991.
- [68] William Press, Saul Teukolsky, William Vetterling, and Brian Flannery. *Numerical Recipes in Fortran: The Art of Scientific Computing*, volume 1. Cambridge University Press, 2 edition, 1992.
- [69] Paul J. Steinhardt, David R. Nelson, and Marco Ronchetti. Bond-orientational order in liquids and glasses. *Physical Review B*, 28(2):784–805, Jul 1983.
- [70] S. Auer and D. Frenkel. Numerical prediction of absolute crystallization rates in hard-sphere colloids. *Journal of Chemical Physics*, 120(6):3015–3029, 2004.
- [71] Johan Mattsson, Hans M. Wyss, Alberto Fernandez-Nieves, Kunimasa Miyazaki, Zhibing Hu, David R. Reichman, and David A. Weitz. Soft colloids make strong glasses. *Nature*, 462:83–86, nov 2009.
- [72] M. Turesson, T. Åkesson, and J. Forsman. Interaction between charged surfaces immersed in a polyelectrolyte solution. *Langmuir*, 23:9555–9558, 2007.
- [73] Peter J. Lu and David A. Weitz. Colloidal particles: Crystals, glasses, and gels. *Annual Review of Condensed Matter Physics*, 4:217–333, 2013.
- [74] Prashant Sinha, Istvan Szilagyi, F. Javier Montes Ruiz-Cabello, Plinio Maroni, and Michal Borkovec. Attractive forces between charged colloidal particles induced by multivalent ions revealed by confronting aggregation and direct force measurements. *Journal of Physical Chemistry Letters*, 4(4):648–652, 2013. PMID: 26281881.

- [75] Takeshi Kawasaki and Hajime Tanaka. Formation of a crystal nucleus from liquid. *Proceedings of the National Academy of Sciences*, 107(32):14036–14041, aug 2010.
- [76] Thomas Palberg. Crystallization kinetics of colloidal model suspensions: Recent achievements and new perspectives. *Journal of Physics: Condensed Matter*, 26(33):333101, 2014.
- [77] Peter G. Bolhuis and David A. Kofke. Monte Carlo study of freezing of polydisperse hard spheres. *Physical Review E*, 54(1):634–643, jul 1996.
- [78] Daan Frenkel and Rob Eppenga. Monte carlo study of the isotropic-nematic transition in a fluid of thin hard disks. *Physical Review Letters*, 49(15):1089–1092, Oct 1982.
- [79] Daan Frenkel and Ard A. Louis. Phase separation in binary hard-core mixtures: An exact result. *Physical Review Letters*, 68(22):3363–3365, jun 1992.
- [80] H. N. W. Lekkerkerker and G. J. Vroege. Liquid crystal phase transitions in suspensions of mineral colloids: new life from old roots. *Philosophical Transactions of the Royal Society A*, 371(1988):0263, 2013.
- [81] L. Guldbrand, B. Jönsson, H. Wennerström, and P. Linse. Electric double layer forces. A Monte Carlo study. *Journal of Chemical Physics*, 80:2221–2228, 1984.
- [82] Roland Kjellander and Stjepan Marceljja. Correlation and image charge effects in electric double layers. *Chemical Physics Letters*, 112(1):49–53, nov 1984.
- [83] Jianzhong Wu, Dusan Bratko, and John M. Prausnitz. Interaction between like-charged colloidal spheres in electrolyte solutions. *Proceedings of the National Academy of Sciences*, 95(26):15169–15172, dec 1998.
- [84] Hartmut Löwen, Paul A. Madden, and Jean-Pierre Hansen. Ab initio description of counterion screening in colloidal suspensions. *Physical Review Letters*, 68(7):1081–1084, feb 1992.
- [85] Grace Martinelli Kepler and Seth Fraden. Attractive potential between confined colloids at low ionic strength. *Physical Review Letters*, 73(2):356–359, Jul 1994.

- [86] Amy E. Larsen and David G. Grier. Like-charge attractions in metastable colloidal crystallites. *Nature*, 385(6613):230–233, Jan 1997.
- [87] Michael A. Bevan and Shannon L. Eichmann. Optical microscopy measurements of kt-scale colloidal interactions. *Current Opinion in Colloid & Interface Science*, 16(2):149–157, 2011.
- [88] Jorg Baumgartl, Jose Luis Arauz-Lara, and Clemens Bechinger. Like-charge attraction in confinement: myth or truth? *Soft Matter*, 2(8):631–635, 2006.
- [89] A. A. Louis. Beware of density dependent pair potentials. *Journal of Physics: Condensed Matter*, 14(40):9187, 2002.
- [90] Bryan Beresford-Smith and Derek Y. C. Chan. Electrical double-layer interactions in concentrated colloidal systems. *Faraday Discussions of the Chemical Society*, 76(0):65–75, 1983.
- [91] R. Castañeda-Priego, V. Lobaskin, J. C. Mixteco-Sánchez, L. F. Rojas-Ochoa, and P. Linse. On the calculation of the structure of charge-stabilized colloidal dispersions using density-dependent potentials. *Journal of Physics: Condensed Matter*, 24(6):065102, 2012.
- [92] Yannick Hallez, Joseph Diatta, and Martine Meireles. Quantitative Assessment of the Accuracy of the Poisson–Boltzmann Cell Model for Salty Suspensions. *Langmuir*, 30(23):6721–6729, jun 2014.
- [93] Trung Dac Nguyen, Benjamin A. Schultz, Nicholas A. Kotov, and Sharon C. Glotzer. Generic, phenomenological, on-the-fly renormalized repulsion model for self-limited organization of terminal supraparticle assemblies. *Proceedings of the National Academy of Sciences*, 112(25):E3161–E3168, 2015.
- [94] Patrick A. Bonnaud, Christophe Labbez, Ryuji Miura, Ai Suzuki, Naoto Miyamoto, Nozomu Hatakeyama, Akira Miyamoto, and Krystyn J. Van Vliet. Interaction grand potential between calcium-silicate-hydrate nanoparticles at the molecular level. *Nanoscale*, 8(7):4160–4172, 2016.

- [95] David Van Der Spoel, Erik Lindahl, Berk Hess, Gerrit Groenhof, Alan E. Mark, and Herman J. C. Berendsen. Gromacs: Fast, flexible, and free. *Journal of Computational Chemistry*, 26(16):1701–1718, 2005.
- [96] V. Ballenegger, A. Arnold, and J. J. Cerdà. Simulations of non-neutral slab systems with long-range electrostatic interactions in two-dimensional periodic boundary conditions. *Journal of Chemical Physics*, 131:094107–094107, sep 2009.
- [97] V. Ballenegger. Communication: On the origin of the surface term in the ewald formula. *Journal of Chemical Physics*, 140(16):161102, apr 2014.
- [98] Peter Sloth and Torben S. Sørensen. Monte carlo calculations of chemical potentials in ionic fluids by application of widom’s formula: Correction for finite-system effects. *Chemical Physics Letters*, 173(1):51–56, 1990.
- [99] G. S. Manning. Limiting Laws and Counterion Condensation in Polyelectrolyte Solutions I. Colligative Properties. *Journal of Chemical Physics*, 51:924–933, 1969.
- [100] E. Trizac, L. Bocquet, M. Aubouy, and H. H. von Grünberg. Alexander’s Prescription for Colloidal Charge Renormalization. *Langmuir*, 19(9):4027–4033, apr 2003.
- [101] Aldemar Torres, Gabriel Téllez, and René van Roij. The polydisperse cell model: Nonlinear screening and charge renormalization in colloidal mixtures. *Journal of Chemical Physics*, 128(15):154906, apr 2008.
- [102] Bruno D’Aguanno and Rudolph Klein. Structural effects of polydispersity in charged colloidal dispersions. *Journal of the Chemical Society: Faraday Transactions*, 87(3):379–390, jan 1991.
- [103] Elena V. Shevchenko, Dmitri V. Talapin, Nicholas A. Kotov, Stephen O’Brien, and Christopher B. Murray. Structural diversity in binary nanoparticle superlattices. *Nature*, 439(7072):55–59, jan 2006.
- [104] Wiel H. Evers, Bart De Nijs, Laura Filion, Sonja Castillo, Marjolein Dijkstra, and Daniel Vanmaekelbergh. Entropy-Driven Formation of Binary Semiconductor-Nanocrystal Superlattices. *Nano Letters*, 10(10):4235–4241, oct 2010.

- [105] Stefan Auer and Daan Frenkel. Suppression of crystal nucleation in polydisperse colloids due to increase of the surface free energy. *Nature*, 413(6857):711–713, oct 2001.
- [106] Marjolein N. van der Linden, Alfons van Blaaderen, and Marjolein Dijkstra. Effect of size polydispersity on the crystal-fluid and crystal-glass transition in hard-core repulsive Yukawa systems. *Journal of Chemical Physics*, 138(11):114903, mar 2013.
- [107] Marjolein Dijkstra, Daan Frenkel, and Jean-Pierre Hansen. Phase separation in binary hard-core mixtures. *Journal of Chemical Physics*, 101(4):3179–3189, aug 1994.
- [108] D. V. Byelov, M. C. D. Mourad, I. Snigireva, A. Snigirev, A. V. Petukhov, and H. N. W. Lekkerkerker. Experimental Observation of Fractionated Crystallization in Polydisperse Platelike Colloids. *Langmuir*, 26(10):6898–6901, may 2010.
- [109] A. Esztermann and H. Löwen. Colloidal Brazil-nut effect in sediments of binary charged suspensions. *Europhysics Letters*, 68(1):120, oct 2004.
- [110] Diego Noguera-Marín, Carmen L. Moraila-Martínez, Miguel A. Cabrerizo-Vílchez, and Miguel A. Rodríguez-Valverde. Particle Segregation at Contact Lines of Evaporating Colloidal Drops: Influence of the Substrate Wettability and Particle Charge–Mass Ratio. *Langmuir*, 31(24):6632–6638, jun 2015.
- [111] Andrea Fortini, Ignacio Martín-Fabiani, Jennifer Lesage De La Haye, Pierre-Yves Dugas, Muriel Lansalot, Franck D’Agosto, Elodie Bourgeat-Lami, Joseph L. Keddie, and Richard P. Sear. Dynamic Stratification in Drying Films of Colloidal Mixtures. *Physical Review Letters*, 116(11):118301, mar 2016.
- [112] Jiajia Zhou, Ying Jiang, and Masao Doi. Cross Interaction Drives Stratification in Drying Film of Binary Colloidal Mixtures. *Physical Review Letters*, 118(10):108002, mar 2017.
- [113] D. G. A. L. Aarts. Capillary Length in a Fluid-Fluid Demixed Colloid-Polymer Mixture. *Journal of Physical Chemistry B*, 109(15):7407–7411, apr 2005.

- [114] Marjolein Dijkstra, René van Roij, and Robert Evans. Phase Behavior and Structure of Binary Hard-Sphere Mixtures. *Physical Review Letters*, 81(11):2268–2271, sep 1998.
- [115] O. Zvyagorskaya, A. J. Archer, and C. Bechinger. Criticality and phase separation in a two-dimensional binary colloidal fluid induced by the solvent critical behavior. *Europhysics Letters*, 96(2):28005, 2011.
- [116] J. L. Barrat and J. P. Hansen. On the stability of polydisperse colloidal crystals. *Journal de Physique France*, 47(9):1547–1553, sep 1986.
- [117] P. N. Pusey, E. Zaccarelli, C. Valeriani, E. Sanz, Wilson C. K. Poon, and Michael E. Cates. Hard spheres: Crystallization and glass formation. *Philosophical Transactions of the Royal Society A*, 367(1909):4993–5011, dec 2009.
- [118] Thomas Palberg, Eckhard Bartsch, Richard Beyer, Maximilian Hofmann, Nina Lorenz, Janina Marquis, Ran Niu, and Tsuneo Okubo. To make a glass—avoid the crystal. *Journal of Statistical Mechanics*, 2016(7):074007, 2016.
- [119] Ludovic Berthier, Patrick Charbonneau, Daniele Coslovich, Andrea Ninarello, Misaki Ozawa, and Sho Yaida. Configurational entropy measurements in extremely supercooled liquids that break the glass ceiling. *Proceedings of the National Academy of Sciences*, 114(43):11356–11361, oct 2017.
- [120] Makoto Fushiki. Molecular-dynamics simulations for charged colloidal dispersions. *Journal of Chemical Physics*, 97(9):6700–6713, nov 1992.
- [121] J. Dobnikar, Y. Chen, R. Rzehak, and H. H. von Grünberg. Many-body interactions and the melting of colloidal crystals. *Journal of Chemical Physics*, 119(9):4971–4985, aug 2003.
- [122] Bryan Beresford-Smith, Derek Y. C Chan, and D. John Mitchell. The electrostatic interaction in colloidal systems with low added electrolyte. *Journal of Colloid and Interface Science*, 105(1):216–234, may 1985.
- [123] M. Brunner, C. Bechinger, W. Strepp, V. Lobaskin, and H. H. von Grünberg. Density-dependent pair interactions in 2D. *Europhysics Letters*, 58(6):926, jun 2002.

- [124] R. A. Marcus. Calculation of Thermodynamic Properties of Polyelectrolytes. *Journal of Chemical Physics*, 23(6):1057–1068, jun 1955.
- [125] José Marcos Falcón-González and Ramón Castañeda-Priego. Renormalized jellium mean-field approximation for binary mixtures of charged colloids. *Physical Review E*, 83(4):041401, apr 2011.
- [126] María Isabel García de Soria, Carlos E. Álvarez, and Emmanuel Trizac. Renormalized jellium model for colloidal mixtures. *Physical Review E*, 94(4):042609, oct 2016.
- [127] R. J. Hunter. *Foundations of Colloid Science*. Clarendon Press, Oxford, 1995.
- [128] T. Hiemstra and W. H. Van Riemsdijk. A Surface Structural Approach to Ion Adsorption: The Charge Distribution (CD) Model. *Journal of Colloid and Interface Science*, 179(2):488–508, may 1996.
- [129] M. Borkovec. Origin of 1-pK and 2-pK models for ionizable water-solid interfaces. *Langmuir*, 13:2608–2613, aug 1997.
- [130] J. Lyklema. *Fundamentals of Interface and Colloid Science - Vol IV*. Elsevier, Amsterdam, 2005.
- [131] L. F. Rojas-Ochoa, R. Castañeda-Priego, V. Lobaskin, A. Stradner, F. Scheffold, and P. Schurtenberger. Density Dependent Interactions and Structure of Charged Colloidal Dispersions in the Weak Screening Regime. *Phys. Rev. Lett.*, 100(17):178304, may 2008.
- [132] Frank Smalenburg, Niels Boon, Maarten Kater, Marjolein Dijkstra, and René van Roij. Phase diagrams of colloidal spheres with a constant zeta-potential. *Journal of Chemical Physics*, 134(7):074505, feb 2011.
- [133] Patrick Wette, Hans Joachim Schöpe, and Thomas Palberg. Comparison of colloidal effective charges from different experiments. *Journal of Chemical Physics*, 116(24):10981–10988, jun 2002.
- [134] V. Lobaskin, B. Dünweg, M. Medebach, T. Palberg, and C. Holm. Electrophoresis of colloidal dispersions in low-salt regime. *Physical Review Letters*, 98:176105, apr 2007.

- [135] Jason W. Merrill, Sunil K. Sainis, and Eric R. Dufresne. Many-Body Electrostatic Forces between Colloidal Particles at Vanishing Ionic Strength. *Physical Review Letters*, 103(13):138301, sep 2009.
- [136] T. Gisler, S. F. Schulz, M. Borkovec, H. Sticher, P. Schurtenberger, B. D’Aguanno, and R. Klein. Understanding colloidal charge renormalization from surface chemistry: Experiment and theory. *Journal of Chemical Physics*, 101(11):9924–9936, dec 1994.
- [137] H. H von Grünberg. Chemical Charge Regulation and Charge Renormalization in Concentrated Colloidal Suspensions. *Journal of Colloid and Interface Science*, 219(2):339–344, nov 1999.
- [138] M. Heinen, T. Palberg, and H. Löwen. Coupling between bulk- and surface chemistry in suspensions of charged colloids. *Journal of Chemical Physics*, 140(12):124904, mar 2014.
- [139] Eric S. Reiner and C. J. Radke. Electrostatic interactions in colloidal suspensions: Tests of pairwise additivity. *AIChE Journal*, 37(6):805–824, jun 1991.
- [140] Hartmut Löwen. Charged rodlike colloidal suspensions: An ab initio approach. *Journal of Chemical Physics*, 100(9):6738–6749, may 1994.
- [141] Lydéric Bocquet, Emmanuel Trizac, and Miguel Aubouy. Effective charge saturation in colloidal suspensions. *Journal of Chemical Physics*, 117(17):8138–8152, nov 2002.
- [142] L. Belloni. Colloidal Interactions. *Journal of Physics: Condensed Matter*, 12:R549–R587, 2000.
- [143] J. Dobnikar, R. Castañeda-Priego, H. H. von Grünberg, and E. Trizac. Testing the relevance of effective interaction potentials between highly-charged colloids in suspension. *New Journal of Physics*, 8(11):277, 2006.
- [144] Yannick Hallez and Martine Meireles. Fast, Robust Evaluation of the Equation of State of Suspensions of Charge-Stabilized Colloidal Spheres. *Langmuir*, 33(38):10051–10060, sep 2017.

- [145] B. Beresford-Smith. *Some Aspects of Strongly Interacting Colloidal Interactions*. PhD thesis, Australian National University, Canberra, 1985.
- [146] Nikola Kallay, Tajana Preočanin, and Suzana Žalac. Standard States and Activity Coefficients of Interfacial Species. *Langmuir*, 20(7):2986–2988, mar 2004.
- [147] Matthew A. Brown, Guilherme Volpe Bossa, and Sylvio May. Emergence of a Stern Layer from the Incorporation of Hydration Interactions into the Gouy–Chapman Model of the Electrical Double Layer. *Langmuir*, 31(42):11477–11483, oct 2015.
- [148] Jearl Walker. *Halliday & Resnick Fundamentals of Physics*. Wiley, Hoboken, NJ, 2014.
- [149] P. M. Dove and C. M. Craven. Surface charge density on silica in alkali and alkaline earth chloride electrolyte solutions. *Geochim Cosmochim Acta*, 69:4963–4970, 2005.
- [150] Joaquim Li, Martin Turesson, Caroline Anderberg Haglund, Bernard Cabane, and Marie Skepö. Equation of state of PEG/PEO in good solvent. Comparison between a one-parameter EOS and experiments. *Polymer*, 80:205–213, dec 2015.
- [151] Lucas Goehring, Joaquim Li, and Pree-Cha Kiatkirakajorn. Drying paint: From micro-scale dynamics to mechanical instabilities. *Philosophical Transactions of the Royal Society A*, 375(2093):20160161, may 2017.
- [152] Z. Abbas, C. Labbez, S. Nordholm, and E. Ahlberg. Size-dependent surface charging of nanoparticles. *Journal of Physical Chemistry C*, 112:5715–5723, 2008.
- [153] Mikael Lund and Bo Jönsson. On the Charge Regulation of Proteins. *Biochemistry*, 44(15):5722–5727, apr 2005.
- [154] Sidney J. de Carvalho, Ralf Metzler, and Andrey G. Cherstvy. Critical adsorption of polyelectrolytes onto planar and convex highly charged surfaces: The nonlinear Poisson–Boltzmann approach. *New Journal of Physics*, 18(8):083037, 2016.
- [155] Norbert Garbow, Martin Evers, Thomas Palberg, and Tsuneo Okubo. On the electrophoretic mobility of isolated colloidal spheres. *Journal of Physics: Condensed Matter*, 16(23):3835, 2004.

- [156] Filip Strubbe, Filip Beunis, and Kristiaan Neyts. Determination of the effective charge of individual colloidal particles. *Journal of Colloid and Interface Science*, 301(1):302–309, sep 2006.
- [157] Irina A. Shkel, Oleg V. Tsodikov, and M. Thomas Record. Complete Asymptotic Solution of Cylindrical and Spherical Poisson-Boltzmann Equations at Experimental Salt Concentrations. *Journal of Physical Chemistry B*, 104(21):5161–5170, jun 2000.
- [158] Miguel Aubouy, Emmanuel Trizac, and Lydéric Bocquet. Effective charge versus bare charge: An analytical estimate for colloids in the infinite dilution limit. *Journal of Physics A*, 36(22):5835, 2003.
- [159] Salete Pianegonda, Emmanuel Trizac, and Yan Levin. The renormalized jellium model for spherical and cylindrical colloids. *Journal of Chemical Physics*, 126(1):014702, jan 2007.
- [160] Luc Belloni. Ionic condensation and charge renormalization in colloidal suspensions. *Colloids and Surfaces A: Physicochemical and Engineering Aspects*, 140(1–3):227–243, sep 1998.
- [161] Robert D. Groot. On the equation of state of charged colloidal systems. *Journal of Chemical Physics*, 94(7):5083–5089, apr 1991.
- [162] Mark J. Stevens, Michael L. Falk, and Mark O. Robbins. Interactions between charged spherical macroions. *Journal of Chemical Physics*, 104(13):5209–5219, apr 1996.
- [163] A. R. Denton. Poisson–Boltzmann theory of charged colloids: Limits of the cell model for salty suspensions. *J. Phys.: Condens. Matter*, 22(36):364108, 2010.
- [164] Niels Boon, Guillermo Ivan Guerrero-García, René van Roij, and Monica Olvera de la Cruz. Effective charges and virial pressure of concentrated macroion solutions. *Proceedings of the National Academy of Sciences*, 112(30):9242–9246, jul 2015.
- [165] Motoyoshi Kobayashi, Frédéric Juillerat, Paolo Galletto, Paul Bowen, and Michal Borkovec. Aggregation and charging of colloidal silica particles: Effect of particle size. *Langmuir*, 21(13):5761–5769, jun 2005.

- [166] D. Gazzillo and G. Pastore. Equation of state for symmetric non-additive hard-sphere fluids: An approximate analytic expression and new Monte Carlo results. *Chemical Physics Letters*, 159(4):388–392, jul 1989.
- [167] W. G. T. Kranendonk and D. Frenkel. Thermodynamic properties of binary hard sphere mixtures. *Molecular Physics*, 72(3):715–733, feb 1991.
- [168] Daan Frenkel and Anthony J. C. Ladd. New Monte Carlo method to compute the free energy of arbitrary solids. Application to the fcc and hcp phases of hard spheres. *Journal of Chemical Physics*, 81(7):3188–3193, oct 1984.
- [169] Onsager Lars. The effects of shape on the interaction of colloidal particles. *Annals of the New York Academy of Sciences*, 51(4):627–659, may 1949.
- [170] Bruce J. Ackerson. When order is disordered. *Nature*, 365(6441):11–12, sep 1993.
- [171] David A. Kofke and Eduardo D. Glandt. Monte Carlo simulation of multicomponent equilibria in a semigrand canonical ensemble. *Molecular Physics*, 64(6):1105–1131, aug 1988.
- [172] David A. Kofke and Eduardo D. Glandt. Infinitely polydisperse fluids. *Journal of Chemical Physics*, 90(1):439–447, jan 1989.
- [173] Paul Bartlett and Patrick B. Warren. Reentrant Melting in Polydispersed Hard Spheres. *Physical Review Letters*, 82(9):1979–1982, mar 1999.
- [174] Moreno Fasolo and Peter Sollich. Equilibrium Phase Behavior of Polydisperse Hard Spheres. *Physical Review Letters*, 91(6):068301, aug 2003.
- [175] P. Bartlett. The effect of polydispersity on colloidal phase transitions. In *Trends in Colloid and Interface Science XIV*, Progress in Colloid and Polymer Science, pages 137–140. Springer, Berlin, Heidelberg, 2000.
- [176] Peter Sollich and Nigel B. Wilding. Crystalline Phases of Polydisperse Spheres. *Physical Review Letters*, 104(11):118302, mar 2010.
- [177] Nigel B. Wilding and Peter Sollich. Phase behavior of polydisperse spheres: Simulation strategies and an application to the freezing transition. *Journal of Chemical Physics*, 133(22):224102, dec 2010.

- [178] L. Filion, M. Hermes, R. Ni, and M. Dijkstra. Crystal nucleation of hard spheres using molecular dynamics, umbrella sampling, and forward flux sampling: A comparison of simulation techniques. *Journal of Chemical Physics*, 133(24):244115, dec 2010.
- [179] Stefan Auer and Daan Frenkel. Prediction of absolute crystal-nucleation rate in hard-sphere colloids. *Nature*, 409(6823):1020–1023, feb 2001.
- [180] C. Sinn, A. Heymann, A. Stipp, and T. Palberg. Solidification kinetics of hard-sphere colloidal suspensions. In *Trends in Colloid and Interface Science XV*, Progress in Colloid and Polymer Science, pages 266–275. Springer, Berlin, Heidelberg, 2001.
- [181] J. L. Harland and W. van Megen. Crystallization kinetics of suspensions of hard colloidal spheres. *Physical Review E*, 55(3):3054–3067, mar 1997.
- [182] Klaus Schätzel and Bruce J. Ackerson. Density fluctuations during crystallization of colloids. *Physical Review E*, 48(5):3766–3777, nov 1993.
- [183] S. Auer, W. C. K. Poon, and D. Frenkel. Phase behavior and crystallization kinetics of poly-12-hydroxystearic-coated polymethylmethacrylate colloids. *Physical Review E*, 67(2):020401, feb 2003.
- [184] Hans Joachim Schöpe, Gary Bryant, and William van Megen. Small changes in particle-size distribution dramatically delay and enhance nucleation in hard sphere colloidal suspensions. *Physical Review E*, 74(6):060401, dec 2006.
- [185] Hans Joachim Schöpe, Gary Bryant, and William van Megen. Effect of polydispersity on the crystallization kinetics of suspensions of colloidal hard spheres when approaching the glass transition. *Journal of Chemical Physics*, 127(8):084505, aug 2007.
- [186] Eduardo Sanz, Chantal Valeriani, Emanuela Zaccarelli, W. C. K. Poon, P. N. Pusey, and M. E. Cates. Crystallization Mechanism of Hard Sphere Glasses. *Physical Review Letters*, 106(21):215701, may 2011.
- [187] Eduardo Sanz, Chantal Valeriani, Emanuela Zaccarelli, Wilson C. K. Poon, Michael E. Cates, and Peter N. Pusey. Avalanches mediate crystallization in a

- hard-sphere glass. *Proceedings of the National Academy of Sciences*, 111(1):75–80, jan 2014.
- [188] Taiki Yanagishima, John Russo, and Hajime Tanaka. Common mechanism of thermodynamic and mechanical origin for ageing and crystallization of glasses. *Nature Communications*, 8:15954, jun 2017.
- [189] T. Schilling, H. J. Schöpe, M. Oettel, G. Opletal, and I. Snook. Precursor-Mediated Crystallization Process in Suspensions of Hard Spheres. *Physical Review Letters*, 105(2):025701, jul 2010.
- [190] Joshua T. Berryman, Muhammad Anwar, Sven Dorosz, and Tanja Schilling. The early crystal nucleation process in hard spheres shows synchronised ordering and densification. *Journal of Chemical Physics*, 145(21):211901, nov 2016.
- [191] Eric R. Weeks, J. C. Crocker, Andrew C. Levitt, Andrew Schofield, and D. A. Weitz. Three-Dimensional Direct Imaging of Structural Relaxation Near the Colloidal Glass Transition. *Science*, 287(5453):627–631, jan 2000.
- [192] Hajime Tanaka, Takeshi Kawasaki, Hiroshi Shintani, and Keiji Watanabe. Critical-like behaviour of glass-forming liquids. *Nature Materials*, 9(4):324–331, apr 2010.
- [193] Takeshi Kawasaki and Hajime Tanaka. Structural origin of dynamic heterogeneity in three-dimensional colloidal glass formers and its link to crystal nucleation. *Journal of Physics: Condensed Matter*, 22(23):232102, 2010.
- [194] Markus Franke, Sebastian Golde, and Hans Joachim Schöpe. Solidification of a colloidal hard sphere like model system approaching and crossing the glass transition. *Soft Matter*, 10(29):5380–5389, jul 2014.
- [195] Sebastian Golde, Thomas Palberg, and Hans Joachim Schöpe. Correlation between dynamical and structural heterogeneities in colloidal hard-sphere suspensions. *Nature Physics*, 12(7):712–717, jul 2016.
- [196] John Russo and Hajime Tanaka. The microscopic pathway to crystallization in supercooled liquids. *Scientific Reports*, 2:505, jul 2012.

- [197] Mathieu Leocmach, John Russo, and Hajime Tanaka. Importance of many-body correlations in glass transition: An example from polydisperse hard spheres. *Journal of Chemical Physics*, 138(12):12A536, feb 2013.
- [198] Hua Tong and Hajime Tanaka. Revealing Hidden Structural Order Controlling Both Fast and Slow Glassy Dynamics in Supercooled Liquids. *Physical Review X*, 8(1):011041, mar 2018.
- [199] Daniele Coslovich, Misaki Ozawa, and Ludovic Berthier. Local order and crystallization of dense polydisperse hard spheres. *Journal of Physics: Condensed Matter*, 30(14):144004, 2018.
- [200] L. A. Fernández, V. Martín-Mayor, and P. Verrocchio. Optimized Monte Carlo method for glasses. *Philosophy Magazine*, 87(3-5):581–586, jan 2007.
- [201] Andrea Ninarello, Ludovic Berthier, and Daniele Coslovich. Models and Algorithms for the Next Generation of Glass Transition Studies. *Physical Review X*, 7(2):021039, jun 2017.
- [202] Ludovic Berthier, Daniele Coslovich, Andrea Ninarello, and Misaki Ozawa. Equilibrium sampling of hard spheres up to the jamming density and beyond. *Physical Review Letters*, 116:238002, jun 2016.
- [203] Patrick Charbonneau, Jorge Kurchan, Giorgio Parisi, Pierfrancesco Urbani, and Francesco Zamponi. Fractal free energy landscapes in structural glasses. *Nature Communications*, 5:3725, apr 2014.
- [204] Walter. Kauzmann. The Nature of the Glassy State and the Behavior of Liquids at Low Temperatures. *Chemical Reviews*, 43(2):219–256, oct 1948.
- [205] Ludovic Berthier, Patrick Charbonneau, Yuliang Jin, Giorgio Parisi, Beatriz Seoane, and Francesco Zamponi. Growing timescales and lengthscales characterizing vibrations of amorphous solids. *Proceedings of the National Academy of Sciences*, 113(30):8397–8401, jul 2016.
- [206] Dmitri V. Talapin, Elena V. Shevchenko, Maryna I. Bodnarchuk, Xingchen Ye, Jun Chen, and Christopher B. Murray. Quasicrystalline order in self-assembled binary nanoparticle superlattices. *Nature*, 461(7266):964–967, oct 2009.

- [207] Xingchen Ye, Jun Chen, and Christopher B. Murray. Polymorphism in Self-Assembled AB₆ Binary Nanocrystal Superlattices. *Journal of the American Chemical Society*, 133(8):2613–2620, mar 2011.
- [208] Michael A. Boles and Dmitri V. Talapin. Many-Body Effects in Nanocrystal Superlattices: Departure from Sphere Packing Explains Stability of Binary Phases. *Journal of the American Chemical Society*, 137(13):4494–4502, apr 2015.
- [209] C. Knorowski, S. Burleigh, and A. Travesset. Dynamics and Statics of DNA-Programmable Nanoparticle Self-Assembly and Crystallization. *Physical Review Letters*, 106(21):215501, may 2011.
- [210] Alex Travesset. Binary nanoparticle superlattices of soft-particle systems. *Proceedings of the National Academy of Sciences*, 112(31):9563–9567, aug 2015.
- [211] Brigitte Pansu and Jean-François Sadoc. Metallurgy of soft spheres with hard core: From BCC to Frank-Kasper phases. *European Physical Journal E*, 40(11):102, nov 2017.
- [212] Alex Travesset. Nanoparticle Superlattices as Quasi-Frank-Kasper Phases. *Physical Review Letters*, 119(11):115701, sep 2017.
- [213] Valerie J. Anderson and Henk N. W. Lekkerkerker. Insights into phase transition kinetics from colloid science. *Nature*, 416(6883):811–815, apr 2002.
- [214] Clara Weis, Irene Natalia, and Norbert Willenbacher. Effect of weak attractive interactions on flow behavior of highly concentrated crystalline suspensions. *Journal of Rheology*, 58(5):1583–1597, aug 2014.
- [215] E. Bartsch, T. Eckert, C. Pies, and H. Sillescu. The effect of free polymer on the glass transition dynamics of microgel colloids. *Journal of Non-Crystalline Solids*, 307-310:802–811, sep 2002.
- [216] W. C. K. Poon, K. N. Pham, S. U. Egelhaaf, and P. N. Pusey. 'Unsticking' a colloidal glass, and sticking it again. *Journal of Physics: Condensed Matter*, 15(1):S269, 2003.
- [217] Anna Kozina, Dominik Sagawe, Pedro Díaz-Leyva, Eckhard Bartsch, and Thomas Palberg. Polymer-enforced crystallization of a eutectic binary hard sphere mixture. *Soft Matter*, 8(3):627–630, dec 2011.

- [218] Lester O. Hedges, Robert L. Jack, Juan P. Garrahan, and David Chandler. Dynamic Order-Disorder in Atomistic Models of Structural Glass Formers. *Science*, 323(5919):1309–1313, mar 2009.
- [219] Daniele Coslovich and Robert L. Jack. Structure of inactive states of a binary Lennard-Jones mixture. *Journal of Statistical Mechanics*, 2016(7):074012, 2016.
- [220] Daniele Coslovich, Misaki Ozawa, and Walter Kob. Dynamic and thermodynamic crossover scenarios in the kob-andersen mixture: Insights from multi-cpu and multi-gpu simulations. *The European Physical Journal E*, 41(5):62, May 2018.
- [221] Christos N. Likos. Soft matter with soft particles. *Soft Matter*, 2(6):478–498, may 2006.
- [222] Ashlee St John Iyer and L. Andrew Lyon. Self-Healing Colloidal Crystals. *Angewandte Chemie International Edition*, 48(25):4562–4566, 2009.
- [223] A. Scotti, U. Gasser, E. S. Herman, Jun Han, A. Menzel, L. A. Lyon, and A. Fernandez-Nieves. Phase behavior of binary and polydisperse suspensions of compressible microgels controlled by selective particle deswelling. *Physical Review E*, 96(3):032609, sep 2017.
- [224] Atsushi Ikeda and Kunimasa Miyazaki. Slow dynamics of the high density Gaussian core model. *Journal of Chemical Physics*, 135(5):054901, aug 2011.
- [225] Sudipta Gupta, Manuel Camargo, Jörg Stellbrink, Jürgen Allgaier, Aurel Radulescu, Peter Lindner, Emanuela Zaccarelli, Christos N. Likos, and Dieter Richter. Dynamic phase diagram of soft nanocolloids. *Nanoscale*, 7(33):13924–13934, aug 2015.
- [226] Manoj Kumar Nandi and Sarika Maitra Bhattacharyya. Analysis of the anomalous mean-field like properties of Gaussian core model in terms of entropy. *Journal of Chemical Physics*, 148(3):034504, jan 2018.
- [227] Dale W. Schaefer. Colloidal suspensions as soft core liquids. *Journal of Chemical Physics*, 66(9):3980–3984, may 1977.

- [228] John B. Hayter and Jeff Penfold. An analytic structure factor for macroion solutions. *Molecular Physics*, 42(1):109–118, jan 1981.
- [229] Jean-Pierre Hansen and John B. Hayter. A rescaled MSA structure factor for dilute charged colloidal dispersions. *Molecular Physics*, 46(3):651–656, jun 1982.
- [230] Antti-Pekka Hynninen and Marjolein Dijkstra. Phase diagrams of hard-core repulsive Yukawa particles. *Physical Review E*, 68(2):021407, aug 2003.
- [231] G. Dupont, S. Moulinasse, J. P. Ryckaert, and M. Baus. The b.c.c.-f.c.c.-fluid triple point as obtained from Monte Carlo simulations of the Yukawa model for monodisperse colloidal suspensions. *Molecular Physics*, 79(2):453–456, jun 1993.
- [232] S. Hamaguchi, R. T. Farouki, and D. H. E. Dubin. Triple point of Yukawa systems. *Physical Review E*, 56(4):4671–4682, oct 1997.
- [233] T. Palberg, W. Mönch, F. Bitzer, R. Piazza, and T. Bellini. Freezing Transition for Colloids with Adjustable Charge: A Test of Charge Renormalization. *Physical Review Letters*, 74(22):4555–4558, may 1995.
- [234] Patrick Wette, Ina Klassen, Dirk Holland-Moritz, Dieter M. Herlach, Hans Joachim Schöpe, Nina Lorenz, Holger Reiber, Thomas Palberg, and Stephan V. Roth. Communications: Complete description of re-entrant phase behavior in a charge variable colloidal model system. *Journal of Chemical Physics*, 132(13):131102, apr 2010.
- [235] Jan K. G Dhont, Carla Smits, and Henk N. W Lekkerkerker. A time resolved static light scattering study on nucleation and crystallization in a colloidal system. *Journal of Colloid and Interface Science*, 152(2):386–401, sep 1992.
- [236] H. J. Schöpe and T. Palberg. Frustration of structural fluctuations upon equilibration of shear melts. *Journal of Non-Crystalline Solids*, 307-310:613–622, sep 2002.
- [237] Patrick Wette, Hans Joachim Schöpe, and Thomas Palberg. Microscopic investigations of homogeneous nucleation in charged sphere suspensions. *Journal of Chemical Physics*, 123(17):174902, oct 2005.

- [238] Patrick Wette and Hans Joachim Schöpe. Nucleation kinetics in deionized charged colloidal model systems: A quantitative study by means of classical nucleation theory. *Physical Review E*, 75(5):051405, may 2007.
- [239] Stefan Auer and Daan Frenkel. Crystallization of weakly charged colloidal spheres: A numerical study. *Journal of Physics: Condensed Matter*, 14(33):7667, 2002.
- [240] Kai Kratzer and Axel Arnold. Two-stage crystallization of charged colloids under low supersaturation conditions. *Soft Matter*, 11(11):2174–2182, mar 2015.
- [241] Peng Tan, Ning Xu, and Lei Xu. Visualizing kinetic pathways of homogeneous nucleation in colloidal crystallization. *Nature Physics*, 10(1):73–79, jan 2014.
- [242] J. Bosse and S. D. Wilke. Low-Density Ionic Glass. *Physical Review Letters*, 80(6):1260–1263, feb 1998.
- [243] Emanuela Zaccarelli, Stefan Andreev, Francesco Sciortino, and David R. Reichman. Numerical Investigation of Glassy Dynamics in Low-Density Systems. *Physical Review Letters*, 100(19):195701, may 2008.
- [244] Ran Niu, Sabrina Heidt, Ramsia Sreij, Riande I. Dekker, Maximilian Hofmann, and Thomas Palberg. Formation of a transient amorphous solid in low density aqueous charged sphere suspensions. *Scientific Reports*, 7(1):17044, dec 2017.
- [245] Jianing Liu, Tong Shen, Zhao Hua Yang, Shu Zhang, and Guang Yu Sun. Multistep Heterogeneous Nucleation in Binary Mixtures of Charged Colloidal Spheres. *Journal of Physical Chemistry Letters*, 8(19):4652–4658, oct 2017.
- [246] Amit Meller and Joel Stavans. Glass transition and phase diagrams of strongly interacting binary colloidal mixtures. *Physical Review Letters*, 68(24):3646–3649, jun 1992.
- [247] Patrick Wette, Hans Joachim Schöpe, and Thomas Palberg. Enhanced crystal stability in a binary mixture of charged colloidal spheres. *Physical Review E*, 80(2):021407, aug 2009.
- [248] Nina J. Lorenz and Thomas Palberg. Melting and freezing lines for a mixture of charged colloidal spheres with spindle-type phase diagram. *Journal of Chemical Physics*, 133(10):104501, sep 2010.

- [249] Hartmut Löwen, Jean-Pierre Hansen, and Jean-Noël Roux. Brownian dynamics and kinetic glass transition in colloidal suspensions. *Physical Review A*, 44(2):1169–1181, jul 1991.
- [250] Paul Salgi and Raj Rajagopalan. Polydispersity in colloids: Implications to static structure and scattering. *Advances in Colloid and Interface Science*, 43(2):169–288, may 1993.
- [251] Eric Dickinson, Roger Parker, and Moti Lal. Polydispersity and the colloidal order-disorder transition. *Chemical Physics Letters*, 79(3):578–582, may 1981.
- [252] E. Dickinson and R. Parker. Polydispersity and the fluid-crystalline phase transition. *Journal de Physique Letters*, 46(6):229–232, mar 1985.
- [253] B. V. R. Tata and A. K. Arora. Crystalline-to-glass transition in charge polydisperse colloids. *Journal of Physics: Condensed Matter*, 4(38):7699, 1992.
- [254] B. V. R. Tata and A. K. Arora. The stable state of charge polydisperse colloids: Disordered or charge ordered? *Journal of Physics: Condensed Matter*, 7(20):3817, 1995.
- [255] Jader Colombo and Marjolein Dijkstra. Effect of quenched size polydispersity on the fluid-solid transition in charged colloidal suspensions. *Journal of Chemical Physics*, 134:154504, 2011.
- [256] A.-P. Hynninen, C. G. Christova, R. van Roij, A. van Blaaderen, and M. Dijkstra. Prediction and Observation of Crystal Structures of Oppositely Charged Colloids. *Physical Review Letters*, 96(13):138308, apr 2006.
- [257] Avi Ben-Simon, Hagai Eshet, and Eran Rabani. On the Phase Behavior of Binary Mixtures of Nanoparticles. *ACS Nano*, 7(2):978–986, feb 2013.
- [258] Robert Botet, Bernard Cabane, Lucas Goehring, Joaquim Li, and Franck Artzner. How do polydisperse repulsive colloids crystallize? *Faraday Discussions*, 186(0):229–240, apr 2016.
- [259] W. Härtl, C. Segschneider, H. Versmold, and P. Linse. On the structure factor of liquid-like ordered binary mixtures of colloidal suspensions. *Molecular Physics*, 73(3):541–552, jun 1991.

- [260] Nicholas Metropolis, Arianna W. Rosenbluth, Marshall N. Rosenbluth, Augusta H. Teller, and Edward Teller. Equation of State Calculations by Fast Computing Machines. *Journal of Chemical Physics*, 21(6):1087–1092, jun 1953.
- [261] P. van Beurten and A. Vrij. Polydispersity effects in the small-angle scattering of concentrated solutions of colloidal sphere. *Journal of Chemical Physics*, 74(5):2744–2748, March 1981.
- [262] Wolfgang Lechner and Christoph Dellago. Accurate determination of crystal structures based on averaged local bond order parameters. *Journal of Chemical Physics*, 129(11):114707, sep 2008.
- [263] Erik E. Santiso and Bernhardt L. Trout. A general set of order parameters for molecular crystals. *Journal of Chemical Physics*, 134(6):064109, feb 2011.
- [264] Sara Jabbari-Farouji, Jean-Jacques Weis, Patrick Davidson, Pierre Levitz, and Emmanuel Trizac. On phase behavior and dynamical signatures of charged colloidal platelets. *Scientific Reports*, 3:3559, dec 2013.
- [265] R. Klein, H. H. von Grünberg, C. Bechinger, M. Brunner, and V. Lobaskin. Macroion shielding and state-dependent pair potentials in colloidal suspensions. *Journal of Physics: Condensed Matter*, 14(33):7631, 2002.

Remerciements

L'auteur remercie le CNRS et la région Bourgogne pour avoir permis le financement de cette thèse.

Je remercie sincèrement René Von Roij et Magali Duvail pour avoir accepté de rapporter cette thèse, ainsi que Nadine Pirio, Virginie Marry, Bernard Cabane, et Lucas Goehring pour leur participation au jury de thèse.

Il me faut remercier sans réserve Christophe et Jean-Marc pour avoir pu m'encadrer toute ces années.

Un grand merci à Agnès, sans qui rien ne fonctionnerait, pour son efficacité et sa disponibilité pour résoudre les nombreux problèmes administratifs et logistiques.

Also, special thanks to Simon for helping with the manuscript.

Je voudrais également remercier les personnes suivantes pour leur collaboration, aide, soutien ou présence; dans le désordre: Luis, André, Fabrice, Martin, Axel, Camille, Nicolas, Gilles, Nicolas, Jaroslava, Hugo, Gang, Sandrine, Isabelle, Bruno, Sylvie, Julien, Pardis, Céline, Valérie, Luc, Carmen et tous ceux que j'ai oubliés.

Enfin, *last but not least*, je tiens à remercier ma mère pour son soutien important, indispensable et indéfectible, ainsi que mes soeurs, nièces et neveux. Je finis par une pensée pour mon père, ancien docteur, qui n'aura pas pu me voir avec ce diplôme.